MONASH University

DEPARTMENT OF MECHANICAL AND AEROSPACE ENGINEERING

DOCTORAL THESIS

Design and Modelling of Robots for Minimally Invasive Surgery

---

Shaotong LIU

Superviors

Dr Chao CHEN

Dr Bernard CHEN

A Prof Laurence HAREWOOD

MONASH University

L M G A

Laboratory of Motion Generation and Analysis

July 2017

Copyright Notice

Abstract

Design and Modelling of Robots for Minimally Invasive Surgery

Robotic minimally invasive surgery are increasingly applied to replace their conventional open-form surgery, due to significant advantages associated with the reduced level of invasion and the advanced functions of the robotic systems. Surgical robots with the remote centre of motion function to constrain the positions of the incision ports have large device footprints and thus suffer extensive collisions when manipulated within confined workspaces. By contrast, the continuum concentric tube robots, which can actively follow complex spatially curved paths within the body cavities, require complex and computationally inefficient kinetostatic models in their design and control. These issues create barriers to the development of more capable surgical robots, as well as the application of such robots in the least invasive single-site or trans-natural-orifices surgeries.

The research presented in this thesis attempts to reduce the footprints of the surgical robots based on the remote centre of motion mechanisms, and improve the computational efficiency of the modelling of the concentric tube robots.

In the first part of the research, a novel planar remote centre of motion mechanism was proposed, with reduced footprint and stay distant from the remote centre (incision port). Necessary conditions were identified to fully constrain the mechanism, and a linkage-based design was generated to minimise the footprint of the robot during surgical manoeuvres. The footprint of the mechanism in the surgical scenario was quantified using four approaches. The proposed mechanism demonstrated up to 35% to 80% improvement over the current parallelogram-based design. For further reduction of the footprint, a cable-based design was proposed. The full proof of functioning, including the remote centre of motion characteristic and the functioning of cable loops, was conducted mathematically, and further validated with finite element analysis and through prototyping.

In the second part of the research, the kinetostatic modelling of the concentric tube robots is studied to improved the computational efficiency. Four robot-dependent modelling approaches were derived based on the combination of the Cosserat rod theory and the Newtonian equilibrium of force and moment. Quantitative comparison between modelling approaches was conducted, where the concentric tube robots were subjected to various external loads. The loading scenarios corresponded to the application of the concentric tube robots as non-cannula and cannula types of robotic surgical tools, and thereby the modelling approaches showing better computational efficiencies in these cases were identified. An improvement of up to 25% in the computing time was observed in one of the modelling approaches when used for non-cannula surgical tools.

The outcomes of this research will benefit the development of the surgical robots with remote centre of motion and the concentric tube robots, both as standalone robots or when combined to generate new surgical robots. These robots, with improve the capability and dexterity, will in turn promote the applications of the robotic minimally invasive surgery with further reduction in the level of invasion.

Declaration

This thesis contains no material which has been accepted for the award of any other degree or diploma at any university or equivalent institution and that, to the best of my knowledge and belief, this thesis contains no material previously published or written by another person, except when due reference is made in the text of the thesis.

Student's Signature:

Print Name: Shaotong LIU

Date: 20th March 2017

Thesis Including Published Works Declaration

I, Shaotong LIU, hereby declare that this thesis contains no material which has been accepted for the award of any other degree or diploma at any university or equivalent institution and that, to the best of my knowledge and belief, this thesis contains no material previously published or written by another person, except where due reference is made in the text of the thesis.

This thesis includes **three** original papers published in peer reviewed journals and **no** unpublished publications. The core theme of the thesis is **design and modelling of robots for minimally invasive surgery**. The ideas, development and writing up of all the papers in the thesis were the principal responsibility of myself, the student, working within the **Department of Mechanical and Aerospace Engineering** under the supervision of **Dr Chao CHEN**.

In the case of **Chapters 3, 4 and 5** my contribution to the work involved the following:
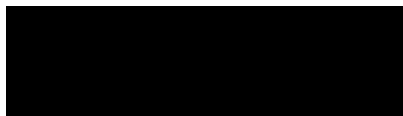
(continue next page)

Thesis Chapter	Publication Title	Status	Nature and % of student contribution	Co-author name(s) Nature and % of contribution	Co-author(s) Monash student
3	A Skeletal Prototype of Surgical Arm Based on Dual-Triangular Mechanism	Published	Conceptual design, math proof of functioning, design and prototyping, math simulations, experiments, and drafting of manuscript, 75%	Laurence HARE-WOOD: review of draft, 2.5%. Bernard CHEN: review of draft, 2.5%. Chao CHEN: conceptual design and input to manuscript, 20%	N N N

(continue next page)

Thesis Chapter	Publication Title	Status	Nature and % of student contribution	Co-author name(s) Nature and % of contribution	Co-author(s) Monash student
4	A Cable Linkage with Remote Centre of Motion	Published	Conceptual design, math proof of functioning, prototyping, math and finte-element simulations, and drafting of manuscript, 70%	Binbin CHEN: proof of functioning, 5%.	Y
				Stéphane CARO: revision of draft, 2.5%.	N
				Sébastien BRIOT: revision of draft, 2.5%.	N
				Laurence HAREWOOD: revision of draft, 2.5%.	N
				Chao CHEN: proof of functioning and input to manuscript, 12.5%	N
5	Framework of Modelling Concentric Tube Robot and Comparison on Computational Efficiency	Published	Mathematical modelling, simulations, and drafting of manuscript 80%	Chao CHEN: mathematicall modelling, input to manuscript, 20%	N

I **have not** renumbered sections of submitted or published papers in order to generate a consistent presentation within the thesis.

Student's Signature:

Date: 20th March 2017

The undersigned hereby certify that the above declaration correctly reflects the nature and extent of the students and co-authors contributions to this work. In instances where I am not the responsible author I have consulted with the responsible author to agree on the respective contributions of the authors.

Main Supervisor's Signature:

Date: 20th March 2017

Acknowledgement

First of all, I would like to thank my supervisors, Dr Chao Chen, Dr Bernard Chen and A Prof Laurence Harewood, for their continuous and generous support on the research project. In particular, I would like to appreciate Dr Chao Chen, for introducing to me the world of academic research, working tirelessly with me over the tough challenges, providing financial support, seeking invaluable feedbacks from the industry, and most importantly, for equipping me with the priceless and comprehensive skills for conducting researches.

I would also like to thank Mr Richard Chen, Mr Brian Carter and the Monash Mechanical Engineering Workshop crew members, for the assistance in the prototyping and the generous sharing of their experience on design and manufacturing. Special thanks go to Mr Andrew Batty and Dr Jordan Thurgood for their efforts on applying for patent protection for the research outcomes, identifying potential applications and establishing connections with the industrial parties. Appreciation goes to Prof Pierre Dupont, for his critical suggestions in defining the directions of the future work.

I further wish to express my greatest appreciation to my beloved family. They had encouraged me to pursue a higher degree as I was in doubt, and have stretched everything they could to support me. I could not love them enough for shaping me into who I am and all the supports they've provided. In particular, I would like to thank my grandfather, Dr Yizhang Liu, who was an engineer and radiologist, and my father, Dr Xianjun Liu, who is a pneumologist. It is them who sparked my interest in engineering, and demonstrated to me how medical engineering could save thousands of lives and benefit the society. And

I would not have chosen engineering for my undergraduate/postgraduate studies as well as the future career without them. I would also wish to thank my uncle, Mr Gaofeng Wu, and my aunt, Mrs Lizhen Wang, for taking care of me over the last ten years since I left my home country and came to Australia.

Lastly, I would like to express my gratitude to my dearest girlfriend, Lynn, for giving me the motivation, assurance and relief I need to battle against the challenges in my life and research career throughout the years, and also her patient wait in the days when we are separated.

List of Publications

Peer-Reviewed Journal Papers

S. T. Liu, L. Harewood, B. Chen, and C. Chen, "A skeletal prototype of surgical arm based on dual-triangular mechanism," *Journal of Mechanisms and Robotics*, vol. 8, no. 4, p. 041015, 2016.

S. Liu, B. Chen, S. Caro, S. Briot, L. Harewood, and C. Chen, "A cable linkage with remote centre of motion," *Mechanism and Machine Theory*, vol. 105, pp. 583-605, 2016.

S. T. Liu and C. Chen, "Framework of modelling concentric tube robot and comparison on computational efficiency," *Meccanica*, 2017.

Conference Papers

S. Liu, C. Chen, B. Chen, and L. Harewood, "Novel linkage with remote centre of motion," in *Proceedings of the 14th IFToMM World Congress*, pp. 338-343, , 2015.

S. Liu, B. Chen, S. Caro, S. Briot, and C. Chen, "Dual-triangular remote centre of motion mechanism with cable transmission," in *4th Joint International Conference on Multibody System Dynamics (IMSD2016)*, 2016.

S. Liu, L. Harewood, B. Chen, and C. Chen, "A review on direct kinematics models and iteration shcemes of continuum concentric tube robots," in *Proc. 2015 Australian Biomedical Engineering Conference (ABEC)*, 2015.

List of Abbreviations

CTR: concentric tube robot

DT: dual-triangular

DOF: degree of freedom

FE: finite element

MIS: minimally invasive surgery

MRI: Magnetic resonance imaging

RC: remote centre

RCM: remote centre of motion

RD: robot dependent

RI: robot independent

ROM: range of motion

PB: parallelogram based

List of Figures

List of Tables

Contents

Chapter 1

Introduction

1.1 Background

Minimally invasive surgeries (MIS), or key hole surgeries, are performed with surgical end effectors inserted into the patient's body through small incision ports rather than conventional big openings [97]. By reducing the level of the invasion, the MIS show significant advantages over the open-form equivalents, including smaller traumas, less blood loss, reduced level of pain, decreased risk of wound infection, better post-operative immune function, faster postoperative recovery, shorter hospital stay, quicker return to the workforce and improved cosmesis [56, 83, 100, 126].

By definition, a surgical robot is a "powered computer controlled manipulator with artificial sensing that can be reprogrammed to move and position tools to carry out a range of surgical tasks" [43]. Surgical robots offer several advanced functions to overcome the drawbacks of conventional manual MIS instruments. Moreover, they provide additional benefits beyond the capability of the manual instruments. For these reasons, surgical robots are increasingly involved in MIS procedures to replace manual equivalents.

There are two major types of conventional MIS instruments: the non-cannula and the cannula types. The non-cannula instruments often feature a common form of having a

long and rigid stick with surgical end effectors mounted at the distal end [126, 131]. The cannulae, on the other hand, are compliant tubes that are fully passive or have limited degrees of freedom (DOFs) at the distal end and can be navigated within body vessels or cavities. Surgical robots that are of corresponding types have been developed.

A non-cannula instrument has only four DOFs (excluding its end-effector) once inserted into the patient's body, which are the roll, pitch, yaw and translation [97]. The reduction in DOF over the seven-DOF human wrist and hand results in a loss of dexterity. Further, the fulcrum effect reverses the direction of motion of the surgical instrument [68, 160], compromising the hand-eye coordination [100]. On surgical robots, the introduction of multi-DOF surgical wrists reproduces the surgeon's hand movements thus recovering the lost dexterity [126, 147]. Control algorithms are implemented to address the fulcrum effect, while images of targets obtained through medical imaging technologies are projected onto the manipulators' frames for better hand-eye coordination, thus recover intuitiveness in operation.

A conventional cannula relies on external lateral forces provided by the surrounding tissue to achieve navigation [165] and can potentially damage the tissue [15]. The navigation ability degrades when advancing in soft tissue, due to reduced lateral force [165]. On the other hand, the compliance for achieving small bending curvature results in buckling and excess torsional flexibility [165]. Further, this reduced stiffness limits the capability to apply adequate surgical forces at the distal end of the cannula [28]. The continuum robots [46, 165, 194] share similar compliant and continuum structures as the conventional cannulae. They can navigate themselves actively to follow complex spatially-curved paths inside body cavities [165], and thereby minimise the damage to the surrounding tissues. Moreover, the higher manipulator stiffness of the continuum robots provides much better output force capability over conventional cannulae [165].

Surgical robots provide other benefits that promote optimal surgical functioning. Filters are added to the controller to filter the surgeons' involuntary hand movements [3, 148]. In combined with motion scaling [31], robots can realise more precise manoeuvres than those of manual instruments [96], allowing surgical procedures that can only be performed

by a very few exceptionally skilled surgeons to be safely and broadly undertaken [177]. Surgical robots also assist in reducing fatigues of surgeons due to long operations [138]. Another advantage that distinguishes the robotic MIS from their manual equivalents is the capability to perform remote operations, including tele-diagnostics [190] and tele-surgery [59]. Safety checks based on the comparison of the positions of manipulators and tissue can be conducted [83] to avoid unintentional contact and to promote safety. Such safety checks can be performed equivalently through contact detection, upon sensing of contact forces at an arbitrary position of the robot [11].

1.2   Problem Statement

1.2.1   Remote Centre of Motion Mechanisms

Since non-cannula instruments (regardless of manual and robotic) are constantly manoeu-vred during surgical procedures, it is crucial to maintain their locations at the incision ports to eliminate the damage to the surrounding tissue. For this reason, many surgical robots include remote centre of motion (RCM) as one of their central functions [180], by controlling the positions and orientations of the instruments with RCM mechanisms. By definition, if a mechanism can rotate at least one of its links around a spatial point without having a physical revolute joint at the point, while this point is distant from the mechanism, this mechanism is considered to be an RCM mechanism [96, 213].

The current clinically-approved state of the art, the da Vinci Xi system [85], features a parallelogram and a revolute joint to achieve two-DOF RCM. The da Vinci series repre-sents the most widely used approach to generate the required DOF with RCM for surgical manoeuvres [96]. However, the use of parallelogram-based (PB) structure leads to a large device footprint [116], which is related to the space needed to operate the mechanism without collision [112]. The consequences include poor access to bedside assistance [71], and more critically, the internal and external (inside/outside the patient's body) colli-sions between the cooperating robotic arms when operating in a confined workspace [181],

which result in the complications during MIS procedures and the compromised optimal surgical functioning [181].

1.2.2   Concentric Tube Robots

The concentric tube robots (CTRs) [165, 194] belong to a unique class of the continuum robots. They are constantly bending, infinite DOF robots with elastic structures [196]. While sharing the continuum structure and compliance with the other type of continuum robots, the tendon-driven robots [200], the CTRs have several critical distinctions. The better coverage of workspace [110], the capability in follow-the-lead applications (active cannulae) [110], and the significantly simpler mechanical structures [115] make the CTRs more suitable than tendon-driven robots in MIS applications.

By providing sufficient stiffness, the CTRs break the barrier between conventional non-cannula and cannula instruments and provide a universal solution to MIS tools. They enable optimal incision path planning to avoid delicate or difficult (obstructing) anatomical structures [48, 165], or to reduce the number of incision ports needed [10]. Such a function is crucial for single-site MIS (e.g. laparoendoscopic single-site surgeries [6, 139]) and trans-natural-orifice MIS (e.g. natural orifice transluminal endoscopic surgeries [6, 24, 48]), which further reduce the level of invasion and represent the future trend of MIS. Moreover, when combined with the RCM mechanisms, the CTRs provide additional angular displacement beyond the output range of motion (ROM) of the RCM manipulators [109]. This combination yields extended ROM inside the patient's body without expanding the overall device footprint or increasing the chance of collision of the surgical robot. Alternatively, it can be understood as achieving the same required ROM with a smaller device footprint or fewer collisions between robotic arms.

On the other hand, the complex and inefficient kinetostatic models cause difficulties towards the application of CTRs. The modelling of the CTRs is different to and much complex than that of the rigid-link manipulators, due to their compliant structures and the consequential interaction with external loads [115]. The modelling is based on the

combination of Cosserat rod theory [150] and the Newtonian equilibrium of force and moment. Assumptions and transformation of frames are extensively involved in the models [115], leading to a reduction in modelling precision. Further, the models, as well as the design optimisation algorithms and controllers that are built on top of them, must be computed numerically through iterative numerical integration [150], consuming substantial computational power and potentially posing difficulties in design optimisation and real-time control of the surgical robots.

1.3 Objectives and Contributions

To achieve the ultimate aim of improving the capability and dexterity of the surgical robots, the following objectives are defined for this research:

1. to develop RCM mechanisms with reduced footprints and stay distant from the remote centres, and validate their effectiveness quantitatively in surgical scenarios.

2. to derive computationally efficient kinetostatic modelling approaches of the CTRs, and quantify the improvement in surgical scenarios.

This research investigated both the RCM mechanisms and the modelling of the CTRs. A novel RCM mechanism with reduced device footprint was proposed, which can be adopted by the current RCM surgical robots manipulating non-cannula instruments. Thereby it achieved an increase in the performance by permitting the surgical robots to be operated in smaller workspaces. It is noteworthy that such an improvement poses minimum modification of the current surgical robot configurations and preserves the advantages (e.g. structural simplicity and decoupled DOFs) of existing systems. Secondly, a fundamental investigation on the kinetostatic modelling of CTRs was conducted towards fast computation and the potential increase in precision. The outcomes will benefit future applications as standalone (non-cannula and cannula) surgical robots or integration with the RCM manipulators, such that the advantage of CTRs can be fully utilised. A summary of research outcomes is listed in Table 1.1 and described further in this section.

Table 1.1: Research outcomes over duration of candidature

Aspects	Outcomes	Publications	Patents
RCM	Linkage-based DT linkage	[116], [113]	n/a
RCM	Cable-constrained DT linkage	[112], [111]	[33]
CTR	Modelling and computational efficiency	[115], [114]	n/a

The proposed two-DOF RCM mechanism adopts the widely used approach of combining a planar RCM mechanism with a revolute joint. A novel planar RCM mechanism, the dual-triangular (DT) linkage, was developed [116], featuring several significant advantages which are favoured for MIS applications, including small footprint, large clearance between the mechanism and the remote centre (RC), and decoupled relation between linkage size and the distance from the base joint to the RC. A cable-constrained design of the DT linkage was developed for further reduction in footprint as well as achieving backlash-free constraints [112]. The RCM function is achieved by a novel design of cable loops, which was proven mathematically and validated through prototype and finite element (FE) analysis. Quantitative comparison between the DT linkage and the conventional PB planar RCM linkage in simplified surgical models demonstrated up to 35-80% reduction in device footprint when described in different approaches [112, 116].

For the CTRs, the framework for kinetostatic modelling was investigated. Four robot-dependent mapping approaches were derived [115] based on Cosserat rod theory and Newtonian equilibrium of force and moment. The effects of each critical assumption were clearly identified, enabling future improvement towards more precise modelling. The computational efficiencies of models were compared through simulations of CTRs subjected to external loads, with one of the newly derived approaches demonstrating up to 25% improvement in overall computation time in the loading scenario that suits the application of CTRs as non-cannula instruments [115]. The effectiveness of another approach, which is equivalent to the existing one presented in [118], in the application as both non-cannula and cannula instruments was also highlighted.

1.4   Thesis Organisation

Chapter 2 presents the literature review on the existing RCM mechanisms and the CTRs. For the RCM robots, major existing RCM mechanisms for MIS applications are critically reviewed, with particular attention paid to the planar RCM mechanisms. For the CTRs, an overview of the evolution of CTR models, as well as the latest developments in the applications of CTR is provided.

Chapter 3 details the work on the design of DT linkage. The fundamental geometry relations between the links and essential constraints equations are derived. The design of the linkage-based prototype that realises the constraint equations is presented. The mathematical comparisons of the footprints between the DT linkage and PB linkage, as well as the resulting quantitative improvement of the DT linkage in the footprint are discussed.

Chapter 4 focuses on the cable-constrained DT linkage. The design of cable loops is detailed. Full proof of RCM function, as well as the numerical and analytical solutions of cable tension, are given, thus fully prove the functioning of the cable-constrained linkage. Outcomes from prototyping and FE simulation are presented to validate the mathematical analysis.

Chapter 5 describes the framework of kinetostatic modelling of CTR. The manipulations of key equations are presented, and the assumptions are listed and discussed. The results of the comparison of the computational efficiencies of CTR models under different loading scenarios are provided, and suitable applications for the models are identified correspondingly.

Chapter 6 summarises the outcomes of the research and discusses future work on RCM mechanisms and CTR towards their individual and combined applications in MIS.

Chapter 2

Literature Review

2.1 Remote Centre of Motion Mechanisms

The remote centre of motion (RCM) can be achieved through mechanical or virtual (software/control) approach [34]. The mechanical RCM approach is favourable in MIS applications where safety is the primary concern [34]. The mechanical RCM eliminates the violation of RCM caused by error in control, sensing or modelling [34,119], and hence promote the safety of both the patients and the surgeons [97]. The focus in this section is the mechanical RCM, the virtual RCM and their footprints.

2.1.1 Mechanical Remote Centre of Motion - Overview

By going through an incision port, a manipulator is limited to have four DOF: two orthogonal rotational DOF perpendicular to the longitudinal axis of incision, one rotational DOF around this axis, and one translational DOF along the axis [37, 97, 98, 120, 210]. Such 3R1T (three-rotation-one-translation) RCM cannot be achieved by a single, nonsynthetic mechanism [97]. The only exception being the isocentre type [97], which is discussed separately in Section 2.1.9.

The RCM mechanisms with lower DOF are combined to achieved the desired 3R1T

[97, 120], by mounting the succeeding mechanisms onto the output links of the previous mechanisms. Such approach is a simple and direct solution which also benefits the decoupling of DOF to increase operational intuitiveness [97]. The commonly used varieties are:

1. 1R + 1R + 1R +1T, where four one-DOF mechanisms are combined [120];

2. 1R + 1R1T + 1R, where one orthogonal rotational DOF and the translational DOF are achieved by one RCM mechanism [120];

3. 2R + 1R+ 1T, where two orthogonal rotational DOF are achieved by one RCM mechanism [98]

4. 3R + 1T, where all rotational DOF are achieved by one RCM mechanism [120].

where combining four one-DOF mechanisms is the most widely-used approach [120].

Various RCM mechanisms with lower DOF have been utilised for the synthesis of 3R1T RCM mechanisms. Further, systematic synthesis methods are proposed to create novel RCM mechanisms [107, 108, 120, 210, 213]. The RCM mechanisms, as well as sample RCM mechanisms generated by the synthesis methods, are briefed in the following subsections, with special attention paid to the device footprints. The 1R planar RCM mechanism on which this thesis is based [34] is introduced in Section 2.1.7.

2.1.2 Revolute Joint
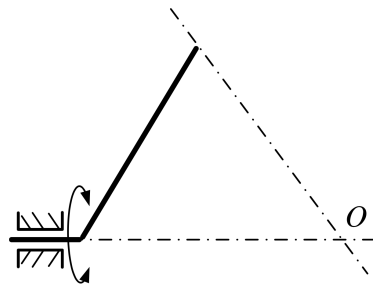
Figure 2.1: Sample 1R revolute joint, RC at Point O [213].

The revolute joint is the most widely-used approach to generate one-DOF RCM. A revolute joint, as shown in Fig. 2.1 creates infinite number of RC locating on its axis of rotation [213]. Such characteristic is unique among the RCM mechanisms and permit easy synthesis of multi-DOF RCM. When combining with another RCM mechanism, the additional DOF of the revolute joints can be added simply by aligning their axes of rotation with the existing RC. For this reason, the revolute joints are often utilised to provide one of the orthogonal rotational DOF and/or the rotational DOF along the axis of incision in multi-DOF RCM mechanisms, including the da Vinci systems [41, 134, 162] which use two revolute joints.

Another advantage of a revolute joint is its structure simplicity [213], as it has no additional link. It is trivial that the footprint of a multi-DOF, revolute-joint-based RCM mechanism is defined merely by parts other than the revolute joints. This characteristic enables the overall device footprint of a multi-DOF RCM mechanism to be optimised by reducing that of the non-revolute-joint parts. Such approach is the foundation of the novel RCM mechanisms proposed in this thesis.

2.1.3   Parallelogram
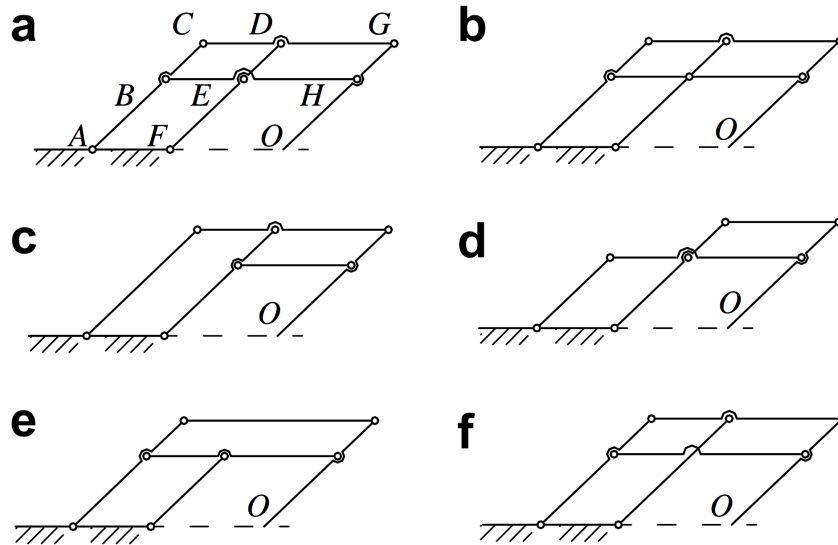
Figure 2.2: Sample double parallelograms, RC at Point O [213].

The parallelogram-based (PB) mechanism is the most commonly-used type of planar RCM mechanism [97, 213], capable in generating 1R and 1R1T RCM. More precisely, the term "parallelogram" refer to the double parallelogram structure that provides the rotational DOF [108]. Some sample configurations of double parallelograms are shown in Fig. 2.2 [213].

The fundamental principle of double parallelogram is identified in [213], which can be regarded as the combination of two virtual centre (VC) mechanisms, or equivalently, the expansion of one VC mechanism [213]. The VC mechanisms are similar to RCM mechanisms, except that they are only capable in rotating a point, rather than an entire link, around the RC [213]. Therefore, a link (for RCM) that rotates around an RC can be obtained by joining two points (for VC) that rotate around the same RC and are not coincident with each other [213]. The two VC mechanisms in this case are both ordinary parallelograms.
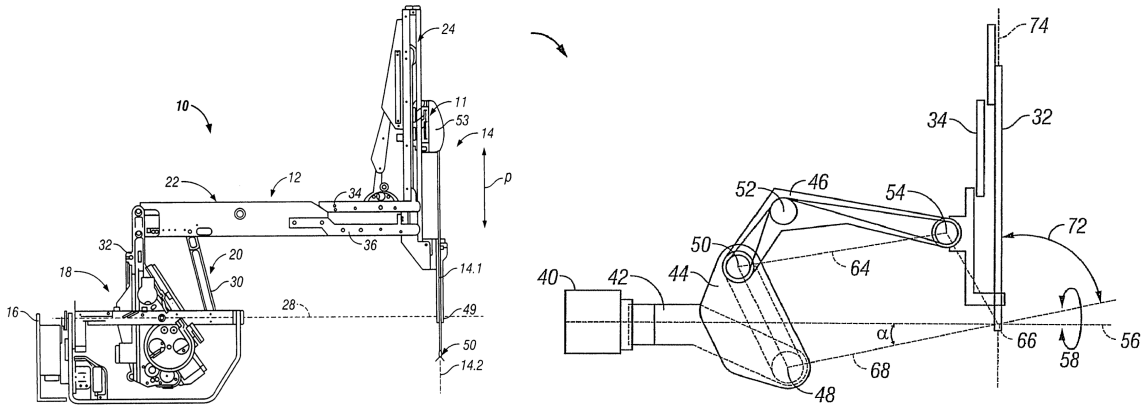
(a) Original da Vinci [134].   (b) da Vinci Si [41].

Figure 2.3: The linkage-based and cable-based da Vinci systems.
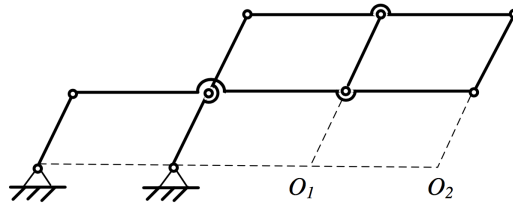
Figure 2.4: Sample PB mechanism with two RC at O_1 and O_2 [9].

Numerous RCM mechanisms have been constructed based on the double parallelograms

that generate orthogonal rotational DOF [12, 41, 45, 53, 55, 71, 72, 90, 93, 108, 121, 126, 134, 149, 158, 162–164, 168–172, 177–179, 185, 193, 210, 212]. Due the similarity in mechanical constraint (parallelism), cable loops are sometimes utilised to replace linkage-based parallelograms [41, 169, 172, 177]. Such replacement may help reducing the dimensions of links, as shown by the evolution from the original da Vinci system [134] to the later da Vinci S/Si/Xi systems [41, 162] (Fig. 2.3), thus it is adopted in the development of an improved RCM mechanism in this thesis. Apart from the ordinary single RC mechanisms, the parallelograms can also be used to synthesis mechanisms with multiple RC [8, 9], as illustrated in Fig. 2.4.
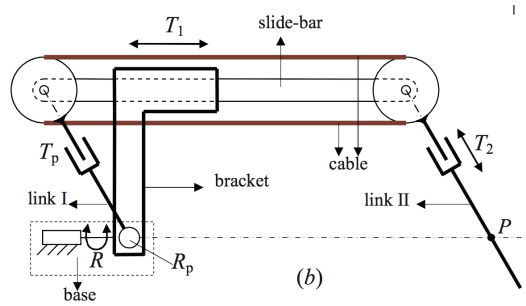
Figure 2.5: Sample alternative PB mechanism with cable loop [105].

Alternative 1R RCM mechanisms have been developed based on parallelogram [104, 105], as shown in Fig. 2.5. In this approach the height (vertical distance to ground link) of the horizontal link in the parallelogram is not changed, by introducing prismatic joints on the input and output links. The approach is also known as the synchronised transmission approach [96, 97].

The parallelograms have certain characteristics that allow easy integration of the translational DOF for 1R1T RCM [72, 108, 210]. Given constrained parallelism, the heights of the horizontal links in a double parallelogram does not affect the RCM function [108]. Therefore, the translational DOF can be achieved by shifting up and down the horizontal links. In [108], a diamond mechanism is introduced to actuate the lower horizontal link. Alternatively, both horizontal links are actuated in [72] (Fig. 2.6), by combining one additional parallelogram to form a triple parallelogram configuration. In another approach [210], a remote actuated chain has been designed based on two connected par-
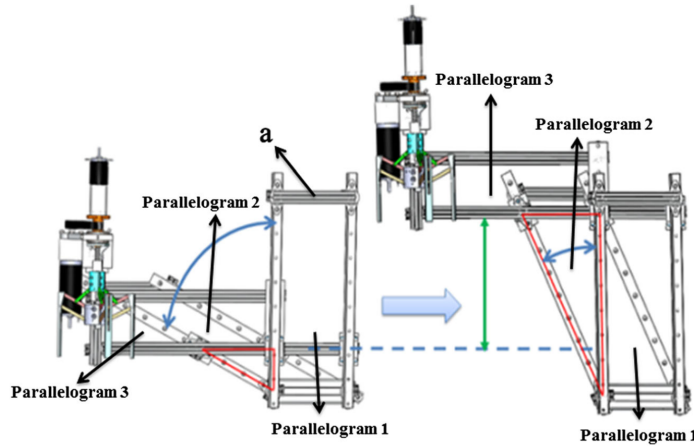
Figure 2.6: Sample 1R1T PB mechanism showing translational DOF [72].

allelograms, to drive a slider that moves along the output link of a double parallelogram. The parallelism of both mechanisms permits them to be integrated and share the input/output links, such that the translational DOF can be actuated from the proximal end of the combined manipulator without compromising the existing rotational DOF.

Despite their clinically-proven wide applications, the footprint issue of the PB RCM mechanisms (both 1R and 1R1T) is outstanding. Experiments indicate that the da Vinci system exhibits significant collisions and cannot perform surgical manipulations within a cube whose length of edge is less than 40 mm [181]. The system continues encountering difficulties in manipulation and higher rates of complications until the size of cube is increased to 70 mm [181].

The footprint of a PB mechanism is closely related to the size of the area enclosed by its outer boundary. It is obvious that such area is proportional to the lengths of links. Given that the minimum clearance between the mechanism and the RC is defined by the shorter between the "horizontal" and "vertical" links in a parallelogram, expanding such clearance extends either/both links. Therefore, displacing the PB mechanism further away from the RC leads to a larger footprint. In the contrast, a PB mechanism with small footprint suffers limited clearance between the mechanism and the RC. Examples of the former and the latter are [149,158,212] and [121], respectively, as illustrated in Fig. 2.7. In addition, the cantilever-like structure when a long horizontal link is used potentially raises
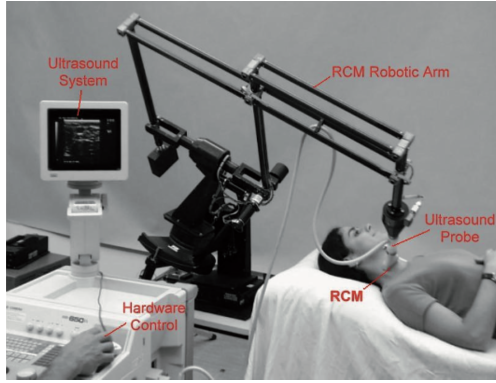
(a) PB faraway from RC, large footprint
[158].
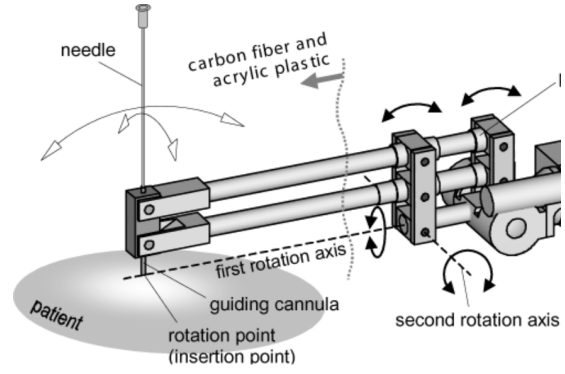
(b) PB close to RC, small footprint [121].

Figure 2.7: Comparison of PB mechanisms with different footprints and clearances to RC.

concerns on system stiffness and accuracy [37], especially when subjected to additional payloads of the succeeding mechanisms [97].

2.1.4   Circular Arc
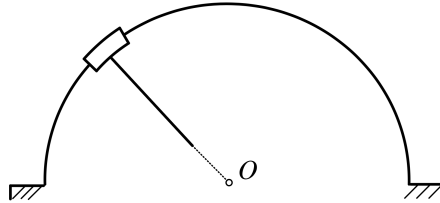
Figure 2.8: Sample 1R circular arc, RC at Point O [213].

The one-DOF circular arc approach is materialised by a slider that travels along a circular arc, where the centre of the arc is the RC [96]. A sample is shown in Fig. 2.8. In RCM synthesis, the additional DOF of the circular arc is added by positioning the arc centre coincidently with the existing RC [88, 122]. The advantage of circular arc is the compactness [213], or to be more specific, the down-scale-ability to realise small mechanism. Examples [16, 17, 22, 81, 88, 191, 192] show that the sizes of circular arcs can be relatively small comparing to the overall sizes of the manipulators, when positioned closely to the RCs.
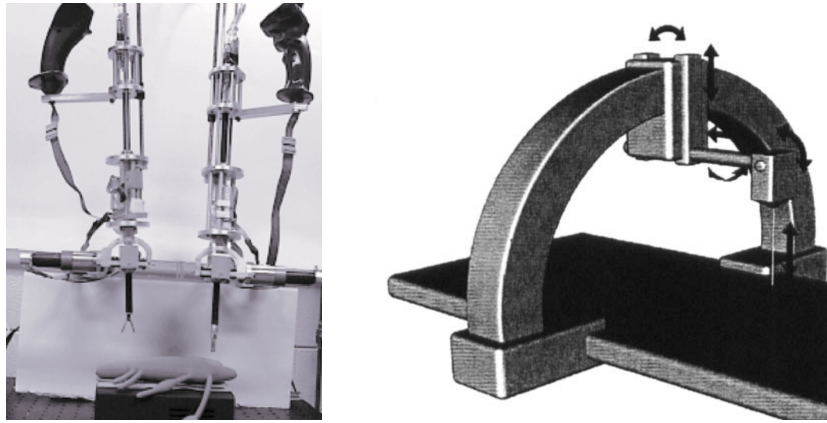
(a) Surgical manipulator
with small circular arc located close to RC (bottom
of manipulator) [88].

(b) Circular arc with size compatible to
an MRI bed, faraway from RC [77].

Figure 2.9: Circular arcs of different sizes.

One disadvantage of the circular arcs is that they require high manufacturing and assembling precision to minimise the error on RC [213]. However, the more critical issues lie on the device footprint [213]. It can be readily seen that to achieve the same ROM, the size of an arc is directly proportional to it radius. Such characteristic is problematic, as expanding the clearance between patient and the RCM mechanism results in large device dimension and footprint, as demonstrated in [44, 77, 129]. An example for comparison between sizes of circular arcs close to and distal from RC is shown in Fig. 2.9.

2.1.5   Spherical Linkage
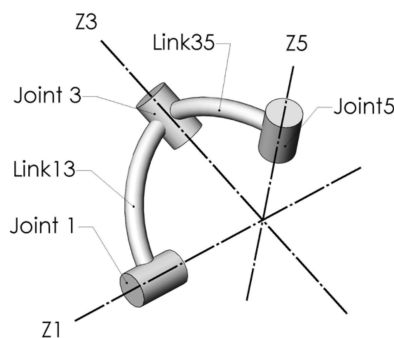
Figure 2.10: Sample 2R (passive Joint 5) or 3R (active Ioint 5) spherical linkage [123].

Figure 2.11: Sample serial spherical linkages (right) and its parallel (left) configuration [123].

The spherical linkage approach is based on the synthesis of two or three revolute joints that are not coincident with each other, and is capable in achieving two orthogonal rotational DOF or all three rotational DOF, respectively. A sample spherical linkage is shown in Fig. 2.10. According to Section 2.1.2, the RC is located at the intersection of the axes of rotation. A spherical linkage can be arranged in either serial [47, 103, 122, 161, 208, 209, 211] and parallel [18, 122, 123, 161] configurations. Figure 2.11 illustrates a sample serial spherical linkage and its parallel version. Apart from the curved links, gear trains can also be used to displace the rotation axes from each other [103, 211].

The issue of the spherical linkages in surgical manipulation is the coupled motion among all rotational DOF, which increases the complexity of the controller. A two-DOF spherical link often comes with a passive revolute joint at the distal end to decouple the along-the-incision-axis rotational DOF, as shown in [122, 123].

There exist two issues regarding the footprint of a spherical linkage. The first one is similar to that of a circular arc, where increasing the clearance between the mechanism and the RC causes expansion in dimension. The second one is a inherent problem associated with non-planar linkage, which is the relatively large transverse dimension even during the one-DOF planar motion. The second issue is more critical and motivated the usage of a planar RCM mechanism in this thesis.

2.1.6   Intersecting Planes
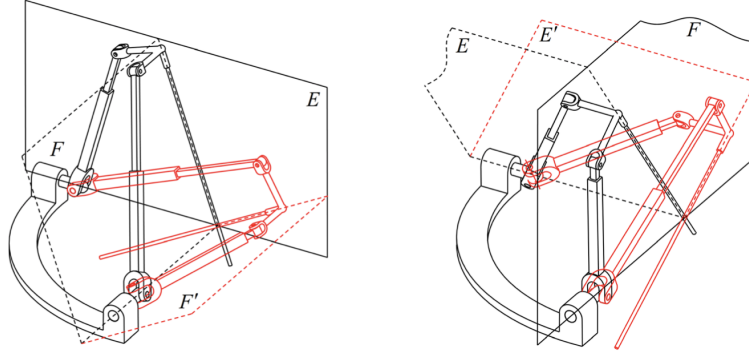
Figure 2.12: Sample intersecting-plane RCM mechanism based on intersection of two planes (Planes E and F) [98]. Note the rotation of planes (E to E' and F to F'').

The approach based on intersection of two or three planes generates parallel RCM manipulators with one or two orthogonal rotational DOF, or all three rotational DOF [12, 98, 106, 107]. A sample mechanism is shown in Fig. 2.12. In this approach, all intersecting planes have their own axes of rotation. The intersection point of the rotation axes is the RC, while the common intersecting line rotates around the RC. The intersection of planes is obtained by connecting all the in-plane serial manipulators. The number of output DOF is changed by alternating the in-plane serial manipulators and the number of intersection planes.

The intersecting planes share some disadvantages with the parallelograms and the spherical linkages. Firstly, the clearance between the manipulator and the RC is affected by the dimensions of the in-plane serial manipulators. Displacing the in-plane serial manipulators from the RC results in expansion in footprint. Further, these manipulators suffer the same problem of having cantilever-like structures as that in the parallelograms, despite that this effect is partially compensated by the parallel configuration. The second issue is the large transverse footprint associated with non-planar mechanism, similar to that of the spherical linkage.

Figure 2.13: Schematic structure of the 1R dual-triangular linkage [34].

2.1.7 Dual-Triangular Linkage

The dual-triangular linkage (DT linkage, Fig. 2.13) is motivated by the footprint issue associated with the PB mechanisms [34]. It generates the same DOF as the double parallelograms, i.e. one orthogonal rotational DOF. The DT linkage can be understood as a pantograph-like mechanism that scales up and reproduces the motion of a four-bar linkage (BCDG in Fig. 2.13). While the mechanism can be constructed from arbitrary four-bar linkage, a special configuration based on [135] is selected for optimal footprint and clearance between the mechanism and the RC [34].

The issue associated with the manipulation of DT linkage is the limit in ROM due to the singularity. Such singularity is introduced the four-bar linkage and the parallelograms, and limits the ROM of the mechanism to half of its theoretical maximum. In this thesis, linkage based auxiliary mechanisms and cable loops are proposed, respectively, to overcome the singularity and achieve full theoretical ROM without expanding the dimension of the mechanism.

The DT linkage is claimed to produce a smaller device footprint while keeping a larger clearance to RC, as the last joint of the mechanism stays faraway from the RC [34]. Moreover, the shorter links (comparing to double parallelograms) require less additional space behind the input joint during manipulation, which reduces the overall device footprint. Further benefits of having shorter links include lighter mechanism, higher rigidity and

better inertia profile. The claimed advantages on the device footprint are validated in this thesis, by quantitative comparison of device footprints between the DT linkage and the double parallelogram.

2.1.8   Systematic Synthesis

Apart from the aforementioned specific mechanisms, systematic synthesis methods are proposed [120, 213] for creation of novel RCM mechanisms. The approach presented in [213] is discussed previously in Section 2.1.3, where two arbitrary VC mechanisms, which can be of the same or different types, are utilised to construct planar RCM mechanisms that offer one orthogonal rotational DOF. The other approach [120] generates 1R1T RCM mechanisms, by reproducing the 1R1T DOF of serial manipulators remotely through pantograph mechanisms.

The RCM mechanisms generated from both approaches are strongly dependant on the base mechanisms used in the synthesis. The sample RCM mechanisms illustrated in the works have large footprints or are too close to the RC. Nevertheless, the footprint issue is not the focus of these works.

2.1.9   Isocentre

The isocentre [97] is claimed to be the only approach that is capable in achieving full 3R1T. The approach involves positioning a passive physical joint at the incision port, while the surgical end effector going through such joint is moved by human surgeons or robotic manipulators [59, 84, 92, 142, 157, 159, 167, 205]. Figure 2.14 shows such concept.

However, whether or not the manipulators based on this approach satisfy the definition of RCM remains questionable. Fundamentally, a mechanism is called an RCM mechanism by having no physical revolute joint at the RC [213], which conflicts with the configurations of these manipulators. On the other hand, apart from the passive joints, these manipulators themselves are self-contained robotic manipulators and are indeed

(a) Concept of 3R1T isocentre [96].

(b) ZEUS system based on isocentre [59, 96, 159].
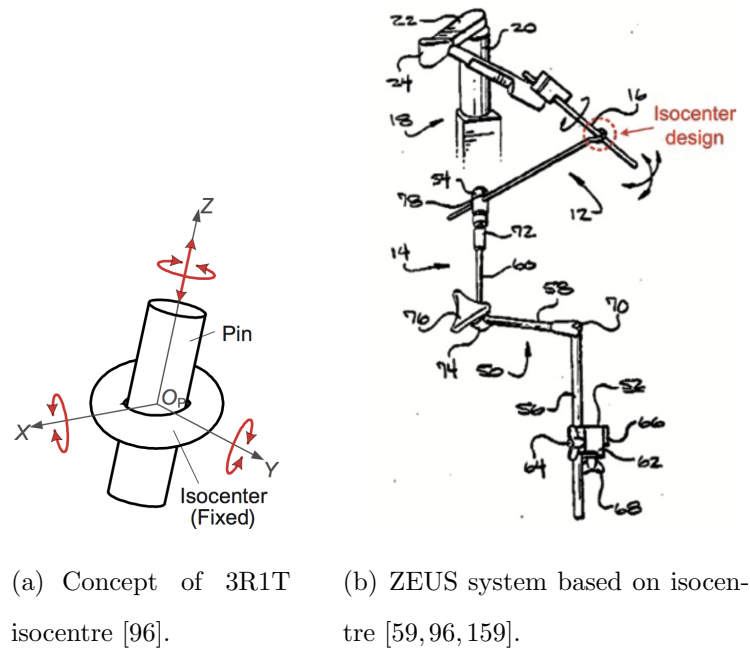
Figure 2.14: Sample 3R1T Isocentre manipulator

positioned distal from and rotate around the RC.
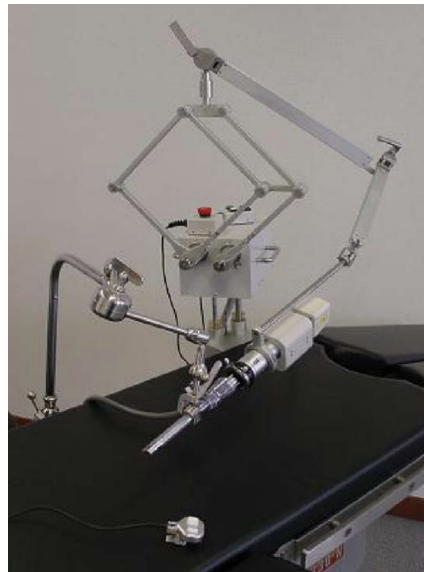
Figure 2.15: Surgical configuration of an isocentre RCM manipulator [205].

Regardless of the classification of the isocentre manipulators, such approach is not considered in this thesis, primary due to the additional mechanisms needed to position the joint at RC, as demonstrated in Fig. 2.15 (additional positioning mechanism at bottom left). The additional mechanisms are potential obstacles within the workspace of surgical robots or human surgeons.

2.1.10   Virtual Remote Centre of Motion

Despite being less safer, the virtual RCM approach is still worth mentioning. Firstly, control algorithms are more generalised approaches that can be adopted by general-purpose robotic manipulators, whose costs are significantly lower than those of the dedicated MIS robots with mechanical RCM [42, 119]. Secondly, surgical robots with mechanical RCM require precise alignment of their RC with the incision ports prior to any surgical manoeuvre. This consequentially requires additional multi-DOF supporting mechanism to define the positions of RC [94].

The virtual RCM approach has been implemented on a wide variety of robotic manipulators with different architectures. Some examples are summarised in Table 2.1, arranged in the order of increasing DOF. In "Architectures", "R", "T/P", "U", "S" and "C" represent revolute, prismatic (T for general convention and P for convention in parallel manipulators), universal, sphere and cylindrical joints, respectively. Note that the DOF refers to the DOF of the robotic manipulators rather than the DOF around incision port. Further details regarding the DOF of virtual RCM manipulators around incision port are well summarised in [96, 97] The asterisks represent the DOF of the mechanisms that are involved in RCM generation, while other parts of the manipulators (generating surgical dexterity) are neglected.

The ZEUS system discussed previously in Section 2.1.9 worth a separated mention, as it uses a hybrid approach to achieve the RCM. Partitioned control is used to alter the behaviour of the non-RCM manipulator, such that it adapts to the passive joint at the incision port and acts kinematically and dynamically as an RCM manipulator [19]. However, it has been reported that such approach can exhibit reduced precision and uncontrolled motion due to the backlash between the instrument and the trocar [42, 94].

For other surgical robots that rely purely on virtual RCM, the strategy is to implement position or force control on redundant robotic manipulators [34, 42]. Typical control algorithms reported include dynamic posture decoupling [131], forward kinematics optimisation [119], adaptive force control [94] and Cartesian control algorithm [142]. On the

Table 2.1: Summary of sample robotic manipulators with virtual RCM

Manipulator	DOF	Architectures	S/P	Reference
ER1	two*	active 1R1T, passive 3R	serial	[132]
IO-MRI robot	two*	active 2T (2-PR)	parallel	[89]
n/a (schematic only)	three	active 3R	serial	[131]
AESOP	four	active 3R1T, passive 3R	serial	[142]
UCB/UCSF	four*	active 1R3T (2-UPS, 1-UPU)	parallel	[30]
MIS/open-convertible	five*	active 5R	serial	[91]
UT-MRI	five	active 3T + passive 2R	serial	[76, 133]
MRI needle placement	five	active 2R3T	serial	[19]
Mitsubishi PA-10	six	active 6R	serial	[49, 119, 130]
PRAMiSS	six*	active 6T (6-RRCRR)	parallel	[42]

other hand, while the mainstream control algorithms are based on precise known kinematic models of the manipulators [19], an artificial intelligence (AI) based incremental adaptive motion control is proposed [19]. The approach enables the use of arbitrary unencoded, uncalibrated manipulators and does not require pre-operative registration [19]. Apart from the aforementioned algorithms that focus on the manipulators themselves, control algorithms with synergistic human-machine interface [76, 133] are proposed to allow the surgeons to move the manipulator directly by hand.

2.2 Cable System and Constraint Analysis

Cables can be used to actuate a manipulators remotely without having bulky terminal energy transformation systems [86, 87]. The cables have low mass, small inertia and

occupy minimum volume [67, 99, 146], which are highly valuable for robotic manipulators and especially the surgical robots working in the tight space. As such, cables are used extensively in the robotic manipulators of various types, including serial [101, 137], parallel [1, 20, 166, 176, 204, 206] and continuum [29, 196]. As described in Section 2.1.3, the effectiveness of cable in reduction of manipulator footprint has been proven by the da Vinci systems. In this thesis, the same approach is adopted, by replacing links and gear trains in the novel RCM mechanism with cable loops.

2.2.1   The Constraint Analysis

Tension is critical to guarantee the functioning of a cable driven or constrained system. Several approaches have been proposed to compute tension in serial [101, 137] and parallel [1, 58, 74, 75, 145, 206] manipulators. Apart from those, since cable loops are not as intuitive to design as the conventional rigid links, algorithms for optimal cable routing and kinematic analysis have also been developed [38, 186].

On the other hand, the analysis to prove the function of the proposed cable-constrained RCM mechanism in this thesis was conducted through a constraint-based analysis [32]. This approach is a generalised algorithm that takes into account mechanical constraints of all kinds. Such characteristic is vital for the analysis on the proposed RCM mechanism, as the mechanical constraints of the system are sourced from both the cable loops and the rigid links/joints. Further, assuming all cable loops are correctly tensioned, a full mathematical proof including the RCM function as well as the fully constrained (singularity-free) status is needed. The cable tension analysis based on constraint approach can share the generalised coordinates and the mathematical constraint equations with the mathematical proof, simplifying the procedure of full analysis on the RCM mechanism. In addition, the constraint approach also solves for joint loads, which provides guidelines in prototyping.

A brief summary of the constraint approach was published as part of the author's work in [112], including its principle, key equations and the projection of the generalised vari-

ables onto those of the cable system. In short, the approach models the generalised constraint forces along the mechanical constraints as a Lagrange multiplier, which relates the generalised external loads applied onto a system to the mechanical constraints and the generalised coordinates that describe the configuration of this system. The cable tension and the joint loads are contained in the generalised constraint force terms. All cable loops are described as constraint equations that link the rotation of two connected pulleys in the cable loops. Further, the constraint status of the RCM mechanism can be verified, by comparing the number of generalised coordinates and that of the constraint equations. The full manuscript of [112] is attached in Chapter 4 along with the completed analysis on the cable-constrained RCM mechanism.

2.2.2   Cable Loop Configurations

(a) Sample closed-loop configuration [86].   (b) Sample open-loop configuration [86].
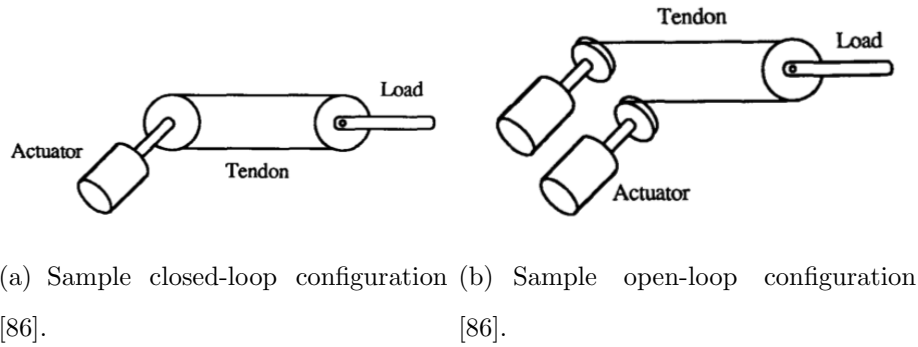
Figure 2.16: Two configurations of a cable loop.

A cable loop can be realised in two forms: the closed-loop and open-loop configurations, respectively [86, 143, 184], as shown in Fig. 2.16. A closed-loop cable can be driven in either directions through one actuator, resulting in a simpler mechanical structure [184]. Pretension of cable is often introduced to prevent slacking of cable at high speed [184]. However, such pretension also introduces side effects such as friction and backlash due to cable elasticity [184]. The open-loop cable features a bio-inspired antagonistic configuration [184], where the two cable sections are connected to their own actuators, respectively. The open-loop configuration resolves the pretension-related issues of the closed-loop, in the expanse of mechanical simplicity.

In this thesis, the closed-loop configuration is chosen to improve the performance of the novel RCM mechanism for two reasons. Firstly, the cable loops are used to constrain rather than actuate the mechanism. Secondly and more importantly, the simpler structure of closed-loop configuration reduces the complexity and thus device footprint of the mechanism. To minimise the negative impacts of closed-loop configuration, the toothed cable [184], i.e. timing belt, is used in the prototyping.

2.3 Concentric Tube Robots

2.3.1 Concentric Tube Robots - Overview
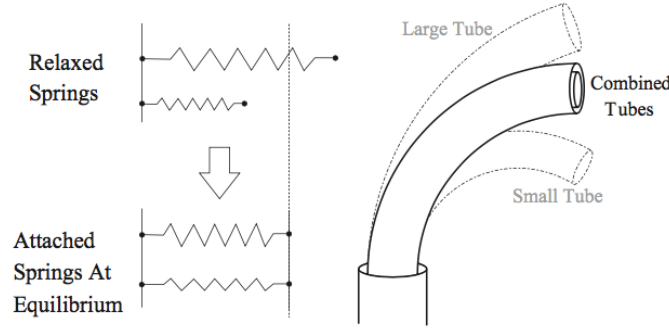
Figure 2.17: Principle of CTR by analogy with 2D springs [194].

The concentric tube robots (CTR) are formed by inserting elastic tubes concentrically into each other [62]. Each elastic tubes, having their own pre-defined curved shapes, interact with each other to define the overall shape of a combined CTR. In this process, individual elastic tubes can experience bending (around two axes orthogonal to the local longitudinal axis) or torsional (around the local longitudinal axis) deformation [62], where the stable final shape is achieved upon equilibrium of force and moment. The principle concept of CTR is illustrated in Fig. 2.17.

The shape of a CTR is controlled by altering the local pre-defined curvatures of the elastic tubes at each cross-sections of the combined CTR. To achieve so, the elastic tubes rotate and translate with respect to each other [196] and hence each tube is driven by

two input DOF at its proximal end, which are the rotation around and translation along the proximal longitudinal axis, respectively.

The structural simplicity and the actuation method of the CTR yield advantages in MIS applications over the conventional rigid link manipulators and the tendon-driven continuum manipulators. Without dedicated backbones [196] or transmission (e.g. actuation tendons) running through the body, the mechanical structure of the CTR is highly simplified. As such, the CTR can be downscale easily to needle-size for reducing the level of invasion [110]. On the other hand, by introducing the translational DOF, the CTR are inherently capably in long extension, i.e. advance of distal tip [165] and provide better workspace coverage [110]. Further, "follow the lead" incision [61, 63, 140, 165] can be achieved by telescopic extrusion [165] of individual elastic tubes. In the contrast, long extension is difficult to achieve on tendon-driven continuum manipulators due to the limited ability to extend the backbone, e.g. in [141].

The existing clinical applications of CTR have been well summarised in [62] and can be broadly categorised into two aspects: the active cannulae [13, 15, 23, 25, 26, 28, 39, 40, 64–66, 95, 173, 175, 182, 183, 187–189, 198, 199, 207], and miniature non-cannula manipulator [24, 27, 79, 80, 174]. The surgical procedures involved include percutaneous [26, 39, 173], transvascular [13, 28, 65, 66, 187–189], and trans-natural-orifices [24, 27, 79, 80, 95, 125, 174, 175, 182, 183], and the targeted organs include brain [15, 26, 39, 64], eyes [198, 199, 207], beating heart [13, 15, 28, 188, 189], lung [95, 125, 175, 183], liver [23], and prostate [79, 80]. Among all procedures, the trans-natural-orifices ones are of least level of invasion. Corresponding incision paths include nasal sinus [24, 27, 174], bronchial tube [95, 125, 175, 183], and urethra [79, 80].

2.3.2 Kinetostatic Modelling - Robot Independent Mapping

Kinetostatic modelling of continuum robots comprises of two mappings [196]: the robot independent (RI) mapping which computes the positions and orientations of the nodes on the robot (task space) using the local curvatures (joint space), and the robot dependent

(RD) mapping that determines the local curvatures based on the robot's mechanical structure and actuator inputs. As such, specific attention is paid to investigate the RD mapping of CTR, while existing RI mappings are adopted to complete the full models. This thesis follows the same strategy by focusing primarily on the RD mappings. The commonly-used RI mapping described in [144] is used.

A CTR is modelled as a collection of frames that are attached to the cross-sections of both the combined CTR and the individual elastic tubes [50, 52, 118, 151–153]. The RI mapping relates the adjacent frames through local curvatures. And by propagating from the proximal end of a CTR to the distal end, the positions and orientations of all the cross-sections can be described in a global reference frame. The RI mapping approaches used in continuum robot modelling are summarised in [196], including Denavit-Hartenburg parameters in [73], Frenet-Serret frames in [35, 73] and exponential coordinates in [82, 151, 152, 156, 165, 194, 195, 197, 203]. The exponential coordinates approach, detailed in [136], is widely used in the CTR models due to easy inclusion of the curvature terms, which are the outputs of RD mappings.

In a CTR, all the frames attached to the same tube (combined CTR or individual elastic tubes) can be regarded as the instantaneous configurations on the trajectory of a moving frame that travels from the proximal end to the distal end of the tube [50, 52, 118]. This enables the RI mapping to be developed based on an analogy to rigid body motion [144, 152]. The difference being that the time derivative in rigid body motion becomes the spatial derivative in the RI mapping, i.e. derivative with respect to arc length.

In rigid body motion, the exponential coordinates approach relates two configurations of a moving body (two frames) through linear and angular velocities. Therefore, it can be implemented in the RI mapping simply by replacing the time velocity terms with spatial velocities, i.e. strains. Since the angular spatial velocity represents the curvature, the output three-component (xyz) local curvatures computed by the RD mapping can be directly substituted into the RI mapping without further modification. Moreover, as the CTR models are solved through numerical integrations, the expressions in RI mapping are written in discretised form, as presented in [144]. Note that for the early

RD mappings [165, 194, 195, 197] where an arc is described as the combination of in-plane scalar curvature and rotation angle of the plane, the expressions for the exponential coordinates are slightly different from those based on three-component curvature. The corresponding expressions are presented in [165, 196].

2.3.3   Kinetostatic Modelling - Robot Dependent Mapping

The RD mapping of CTR can be derived through two strategies [62] that are based on the potential energy and the Newtonian equilibrium of force and moment, respectively. The former include [82, 153, 156, 194, 195, 197]. The latter include [10, 118, 151, 152, 165, 203]. The two strategies are shown to be identical in [50, 62, 152].

Regardless of the strategy taken to derive the RD mapping, some common assumptions are made [120]. These assumptions play vital roles in the derivation of RD mappings by enabling significant simplifications of the key equations and increase in the computational efficiency. On the other hand, they also affect the modelling accuracy. The assumptions are listed below:

1. No longitudinal elongation and shear of elastic tubes. This is a standard assumption in the Kirchoff rod theory, which is a special case of the Cosserat rod [152]. Calculations performed in [152] show an elongation of 10 micrometers when 10.1 N of tension is applied to a Nitinol super-elastic tube with 1.75 mm outer diameter and 207 mm length.

2. Linear constitutive law for bending and torsion, i.e. moments are directly proportional to the deformation. This assumption is another standard one in the Kirchoff rod theory. When used as an active cannula, the predicted strain of a Nitinol super-elastic tube is normally below 3% [152], which stays within the 6-11 % linear range of Nitinol [52, 197].

3. Zero gap between elastic tubes, which ensures the centre lines of all tubes (thus the origins and z-axes of local frames at the all cross-sections) are perfectly aligned.

4. Zero friction between elastic tubes. The assumption is adopted by all RD mapping approaches to date, while a separate investigation on friction is conducted in [117].

5. Zero mass of elastic tubes. The assumption is somewhat validated by observing a tip deflection of less than 0.3 mm on a 150 mm Nitinol CTR with outer diameter 2.77 mm [118].

The potential-energy-based strategy is mostly adopted by the early RD mapping approaches, presumable due to inherent connection between elastic deformation of tubes and elastic potential energy. These approaches do not consider external loads, except for the one presented in [82]. The principle of the strategy is the minimisation of potential energy in a CTR [62, 82], which states that the equilibrium conformation of a CTR is reached when the total potential energy stored in the CTR is minimised.

In the cases where no external loads are considered, the overall potential energy of a CTR is obtained by summing the elastic potential energy of the elastic tubes. The sources of such elastic potential energy are the bending deformation over the entire elastic tubes, and the torsional deformation in their straight sections [194, 197] or over the entire elastic tubes [82, 156, 195]. Euler-Lagrange/Euler-Poincaré equations, and optimal control theory [21] are used in [156, 195] and [82], respectively, to derive the differential equations which are solved for the local curvatures corresponding to the minimum potential energy of a CTR.

The external forces applied at the tip of a CTR is modelled as gravitational potential energy in [82], where the reference plane of zero potential energy passes through the proximal end of the CTR and is perpendicular to the direction in which the tip force is applied. On the other hand, the potential-energy-based approaches have not explored the distributed external forces, nor the external moments.

The Newtonian-based strategy is the foundation of most current RD mapping approaches, due to easy and explicit consideration of external loads of all kinds. Newtonian-based RD mapping starts with CTR subjected to bending deformation (no torsion) and zero external load [165], then further developed to include torsion [50, 52] and eventually both

torsion and external loads [10, 118, 151, 152, 203].

The Newtonian RD mapping is developed based on the Cosserat rod theory [5, 144, 150]. The approaches consist of two steps [52, 118, 152, 203]: the Newtonian equilibrium of force and moment to compute the concentrated forces and moments at each cross-section of a CTR from the external loads, and the constitutive law that maps the moments to the local curvatures. By applying the Newtonian equilibrium of force and moment on a finite CTR section, a set of differential expressions [5] are derived, which describes the spatial rates of changes of concentrated force and moment at a cross-section as a function of local curvatures and the local concentrated force and moment themselves. A 6×6 transformation matrix is used [54] to deal with derivatives with respect to changing frames [144], such that the objective evolution of the force and moment can be distinguished from the changes due to the altered frames.

The Newtonian equations and the constitutive law can be used separately (one after another at a cross-section) [52, 118, 203] or combined into a united expression [151, 152] in an RD mapping approach. Further, the force and moment in the Newtonian equations can be written as two separated terms [52, 118, 203] or as one combined term [151, 152]. The combined force/moment is achieved in the expanse of the implicit force information, as well as the inability to deal with external forces described in local frames. The combinations of two key steps and the two forms of loads result in RD mapping approaches with different computational efficiencies.

The solution of a CTR model involves solving differential equations whose boundary conditions are separated at two ends of the CTR. The analytical solutions exist only for simplified models with no torsion, or simple cases where the CTR contains two elastic tubes or are of constant pre-defined curvatures [62]. All other cases, which are much closer to the configurations of CTR in MIS applications, must be solved iteratively through numerical integration. The shooting method is used to solve the boundary value problem (BVP, separated boundary conditions), by making initial guesses to fix up the unknown elements and convert the BVP into an initial value problem (IVP). Alternatively, force/-torque sensors (FT sensors) are introduced to measure the actuator input forces and

moments at the proximal end of a CTR for the conversion to IVP [203]. The numerical integration can be started from both the proximal [155, 203] and distal ends [118] of a CTR.

Provided that the CTR models are solved numerically, and the fact that the succeeding design optimisation as well as control algorithms of CTR are all developed based on the kinetostatic models, the substantial complexity (and thus the high computing time/cost) is obstructing the further developments of CTR models towards higher accuracy, faster solution time and less computational cost. It has been concluded that the current balance between complexity and accuracy of CTR models is at a "sweet point" [62]. In this thesis, fundamental study on the framework of RD mapping was conducted in the attempt to improve the computational efficiency and enable faster solution of CTR model.

2.3.4   Design, Control and Path Planning

Although design, control and path planning of the CTR are beyond the scopes of this thesis, they are essential components towards the applications. For the comprehensiveness of the review, a brief summary regarding the development in these aspects is provided below.

The snapping of CTR is a concern in the MIS applications, which involves sudden change in configuration of a CTR and has been recognised in the early works on CTR models [50, 52, 195, 197]. Such snapping is extremely dangerous, especially given that the CTR will be used in neuro or cardiac surgeries to handle delicate but vital tissues [69]. From the potential energy point of view, the principle of snapping is the rapid release of elastic potential energy, and the fast transformation from one local minimum to another local minimum point that is nearby and has a lower energy [69, 202]. The snapping issue can be reduced or eliminated through control or optimal design approaches [78]. For the control approach, a path planning algorithm has been derived to actuate the CTR so that it stays within the snap-free configurations [14]. On the design side, stability conditions have been derived [60, 69], and design algorithms have been proposed for the optimal

selections of pre-defined shapes [70, 78] or optimal engraved patterns on the surfaces of elastic tubes [7, 102], such that the stability of a CTR is improved when it is manoeuvred within the targeted workspace.

With the torsional effect considered in the kinetostatic models, there are three basic approaches for position control of a CTR. The first one involves pre-computation of kinetostatic solution over the entire workspace of a CTR, and then the solution of the inverse kinematic problem as a root-finding problem [51, 52]. While achieving fast computation, a major drawback of this approach is the inability to deal with cases where multiple direction kinematic solutions exist [62]. The second approach relies on fast computation of arc length parameterised Jacobians and compliance matrices [154]. Such approach is a generalised one which can be implemented on continuum robots of arbitrary architectures [154]. Further it addresses the issues associated with multiple direct kinematic solutions [62]. However, it is less computationally efficient and cannot guarantee the convergence of direct kinematic root-finding [62]. The last approach is also a Jacobian-based approach [201]. It is developed based on a unique fast kinetostatic model [203] that in cooperates actuator input forces and torques measured by force/torque sensors (FT sensors). The introduction of FT sensors increases computational efficiency [203] in the expanse of complex prototype design and being affected by sensor errors [62].

The advantages of CTR over other robotic manipulators lie on the ability to follow the spatial curves and avoid obstacles. As such, tip position control alone is not sufficient to fully utilise the advantages for MIS applications.

To compute the collision-free incision paths, an algorithm [124] has been proposed based on potential fields [36] and thereby converts the path planning into a constrained non-linear optimisation problem. One limitation of this approach is that the obstacles are represented by discrete spheres and does not consider continuum body vessels. However, a more critical issue is that the kinetostatic model [57] on which it is based is overly simplified and does not consider torsional deformation of elastic tubes. The algorithm has been further developed [125] based on an improved kinetostatic model [197] that consider the twist of elastic tubes in their straight sections. The targeted incision path is the

bronchial tube. The mechanics-based model that takes into account torsion in the entire lengths of elastic tubes is utilised in [182], which computes the path through Rapidly-Exploring Roadmap [2]. The approach has been validated for transnasal incision that avoids bones, critical blood vessels and healthy brain tissue [182] and further implemented for use in the bronchial tube [183].

Despite the generalised path planning approaches, design optimisation frameworks [4, 15, 183] have been proposed, which generate CTR that fit specific anatomical structures, by taken into account the corresponding obstacles and desired incision paths. The reason being that the dexterity of individual CTR is limited [110] and highly dependent on the design (selection of elastic tubes and pre-defined shape).

The algorithm in [4] computes the optimal incision path that goes through a series of pre-defined spatial points. The outcome is an incision path with optimal number of curved sections, as well as the length and final curvature of each section, which serve as design parameters of the corresponding CTR. The pre-determined anatomical constraints and way points are described as cost functions in the optimisation. The algorithm in [183] combines the search in the design space with sampling-based motion planning in the configuration space to generate a completed solution for the given anatomical structure [62, 183]. The algorithm in [15] utilises a torsional compliant kinetostatic model [52] and a penalty function that included anatomical constraints in the cost function, by fast computation of initial CTR designs with torsionally-rigid assumption and refine theses designs without.

To promote safer incision, systematic investigation on the follow-the-lead capability of CTR has been conducted in [61, 63] to eliminate the change in shape of CTR during advancing. Necessary constraint conditions have been derived, and the CTR are proven to be capable of follow-the-lead incision given appropriate planar or helical pre-defined curvatures and sequence of deployment. In another work, more generalised constraint equations have been derived independently, which can be implemented on arbitrary extendible continuum robots [15].

Apart from the position control and incision path planning algorithms, a stiffness controller has been designed [127, 128] from a modified position controller. The controller links the sensed CTR tip displacement with the actuator inputs, and thereby achieves user-defined relation between tip displacement and force [62]. Such controller paves the way to realise intrinsic sensing and control of tip force [128].

Chapter 3

The Dual-Triangular Linkage

A novel remote one-degree-of-freedom (one-DOF) planar remote centre of motion mechanism, the dual-triangular linkage (DT linkage) [34], was proposed to achieve the minimised footprint (chance of collisions), distantly-placed mechanism while preserving the decoupled DOF on the current surgical robots with RCM. However, the range of motion (ROM) of the proposed RCM mechanism was limited due to the singularities. Such singularities compromised the reduction in the footprint, as the large required ROM of the MIS applications could only be achieved by a dual-triangular linkage with large dimensions (and thus having a expanded footprint). Further, the claimed advantages of the proposed RCM mechanism were not validated.

Based on the aforementioned research gaps, the specific objectives of the work presented in this chapter were defined as follows:

1. To derive the constraint equations for the DT linkage, for the removal of singularities (expansion in ROM).

2. To design auxiliary mechanisms that materialise the constraint equations.

3. To quantify the footprint of the DT linkage and compare to that of the parallelogram based (PB) planar RCM mechanism.

The work presented is published in [116], and the full manuscripts is attached below. The major research outcomes are:

1. Two sources of singularities, which are the four-bar linkage and the parallelogram, were identified.

2. Two constraint equations corresponding to the four-bar linkage and the parallelogram were derived, respectively.

3. Two auxiliary mechanisms corresponding to the constraints were designed.

4. The ROM of the dual-triangular linkage was doubled.

5. The footprint of the DT linkage was compared to that of the PB design in a simplified surgical scenario, and demonstrated up to 38% reduction.

6. A prototype, implementing the designs of the auxiliary mechanisms, was constructed to experimentally validate the RCM function.

All mathematical simulations regarding the footprint comparison were conducted with Matlab. Supplementary information on the prototype is presented in Section 3.1.

Shao T. Liu
Laboratory of Motion Generation and Analysis,
Department of Mechanical and
Aerospace Engineering,
Monash University,
Victoria 3800, Australia
e-mail: shao.liu@monash.edu

Laurence Harewood
Epworth Freemansons Medical Center,
East Melbourne, Victoria 3002, Australia
e-mail: laurenceharewood@urologyvictoria.com

Bernard Chen
Department of Mechanical and
Aerospace Engineering,
Monash University,
Victoria 3800, Australia
e-mail: bernard.chen@monash.edu

Chao Chen
Laboratory of Motion Generation and Analysis,
Department of Mechanical and
Aerospace Engineering,
Monash University,
Victoria 3800, Australia
e-mail: chao.chen@monash.edu

A Skeletal Prototype of Surgical Arm Based on Dual-Triangular Mechanism

The parallelogram-based remote center of motion (RCM) mechanism used for robotic minimally invasive surgery (MIS) manipulators generates a relatively large device footprint. The consequence being larger chance of interference between the robotic arms and restricted workspace, hence obstruct optimal surgical functioning. A novel mechanism with RCM, dual-triangular linkage (DT-linkage), is introduced to reduce the occupied space by the linkage while keeping sufficient space around the incision. Hence, the chance of collisions among arms and tools can be reduced. The concept of this dual-triangular linkage is proven mathematically and validated by a prototype. Auxiliary mechanisms are introduced to remove the singularity at the fully folded configuration. The characterized footprints of this new linkage and the one based on parallelograms are analyzed and compared. [DOI: 10.1115/1.4032976]

1 Introduction

Robotic systems are generally considered to have higher precision than human operators [1] and are able to recover the lost dexterity or degrees-of-freedom (DOF) caused by the incision of surgical devices into the patients' bodies [2,3]. These advantages, driven by the desire of providing less invasive and inherently safer surgical procedures, have led to increasing involvement of robotic systems in MIS.

To promote safety, robotic surgical systems include RCM property as one of their central function [4], which allows the manipulators to be pivoted around their incision ports. The RCM function is normally achieved by the implementation of RCM mechanisms. In addition to the RCM mechanisms, other mechanisms have to be also integrated to provide the incision/retraction motion through the incision port as well as the multi-DOF surgical manipulation inside the patient's body.

By definition, if a link of the mechanism can rotate around a fixed point distal from the mechanism, while there is no physical revolute joint at the fixed point, the mechanism is referred to as an RCM mechanism [1,5]. A remote center (RC) can be constrained virtually or mechanically [6]. In a virtual RCM, the RC is constrained by control strategies on a redundant robotic manipulator, based on precise kinematic or dynamic model of the robot. The strategies include dynamics posture decoupling [7], forward kinematics optimization method [8], adaptive force control [9], and Cartesian control algorithm [10].

However for surgical procedures in which safety is vital, virtual RCM mechanisms are less favorable due to possible error in control, sensing, or modeling. On the other hand, mechanical RCM mechanisms are more reliable and considered suitable for clinical applications [1]. Mechanical RCMs applied on surgical robots have been well documented, which include isocenters [11], circular tracking arcs [12,13], parallelograms [2,14–18], synchronous transmissions [19], and spherical linkages [20]. Mechanisms that achieve multiple RCs mechanically are explored [21].

In practice, a common approach to generate the two-DOF RC required in an MIS is to combine a selected one-DOF planar RCM mechanism with a single revolute joint [1]. In this approach, the planar RCM mechanism is located on the rotation axis of the revolute joint so that the second DOF can be added. Parallelogram is the selected planar RCM mechanism for many surgical robot systems of this type [1], including the most widely deployed da Vinci series [15,22,23].

Despite being proven through clinical applications to be a reliable solution, most of the issues associated with a parallelogram-based linkage (PB-linkage) are due to its footprint, which is closely related to the output joint of the parallelogram. The presence of the output joint close to the incision port occupies additional space in the region near the RC. However, pushing such joint further away from the RC to reduce the device footprint within this region leads to longer output link, hence enlarges the geometry of the parallelogram. This in turn expands the device footprint, as it is generated by rotating the enclosed area of the parallelogram around the axis of the single revolute joint. The graphical illustration as well as details regarding mathematical simulation are presented later in Sec. 3.

More significantly, the use of PB-linkage introduces negative impact on the integration of the translational stage, which provides the translational DOF through the RC. On a PB-linkage, the translational stage with its actuation needs to be mounted directly onto the output link, which is operated within the region near the RC. Thus, it increases the device footprint as well as the chance of interference. The alternative solution is to mount the actuation elsewhere, which forces the transmission to go through the RCM mechanism, thus results in coupled motion and introduce difficulty in the design of the mechanical structure as well as control system. Poor access for bedside assistance [23] and larger chance of collisions or restricted workspace for individuals have been reported, hence prevent optimal surgical functioning [24]. Note that while there exist RCM mechanisms that generate both rotation and translation, they have coupled DOFs [25], or are relatively bulky in transverse dimensions [26], or are parallelogram-based which the footprint issue partially persists [27]. For reducing complexity in control, promotion of confidence

in safety in MIS applications and rapid manual positioning of the center device or certain DOF [28], this paper focuses on the nonparallelogram-based, planar RCM mechanisms that generate one-DOF rotation only.

A novel RCM mechanism, named the DT-linkage, was invented to minimize the footprint of robotic surgical arms, especially in region near the RC [29]. The first prototype, which is a passive skeletal prototype based on the DT-linkage, was built for proving the RCM function [6]. The new prototype is designed taken into account the range of motion (ROM) requirements of abdominal MIS applications, which is absent on the previous prototype. It also contains the mechanisms for defining the position of the RC in the space, as well as the actuations and control system of the two-DOF RCM mechanism. Most importantly, this prototype has auxiliary mechanisms that remove singularity from the DT-linkage and double the ROM (comparing to the unconstrained previous prototype) without increasing the device footprint. Section 2 provides brief description on the conceptual design as well as the auxiliary mechanisms to overcome singularity. Section 3 produces an analysis on the footprints of the DT-linkage and the PB-linkage. Section 4 presents the prototyping.

2 The DT-Linkage

The concept of the DT-linkage is shown in Fig. 1, which is based on two pairs of similar triangles: one pair of OFG and OAC and another pair of OHG and OEC. The similarities of these two pairs are enforced by two parallelograms ABGF and EDGH, respectively. The lengths of the links are constrained by

$$\frac{c}{b} = \frac{f}{e} = r \tag{1}$$

where c, b, f, and e are the lengths of links AC, FG (AB), CE, and GH (DE), respectively. Parameter r is a constant greater than 1.

The outer shape of the mechanism, since it can be adapted to arbitrary four-bar linkage, was chosen according to a novel classification of four-bar linkage [30]. The selected final shape is known as 2 K-SLLS structure. In such structure, 2 stands for two link lengths, K stands for the symmetry kite shape, SLLS (short-long-long-short) stands for the configuration of links in which the links with the same length are adjacent to each other, while the ground and output links being the longer ones. The 2 K-SLLS shape simplifies the geometry of the DT-linkage, as the geometry is fully defined by two rather than four link lengths. In addition, the symmetry shape leads to easy implementation of auxiliary mechanisms for removing the singularity, which is described in Sec. 3. The reason why 2 K-SLLS is used instead of 2 K-LSSL is that its input and connector links are shorter than the ground and output links, hence the DT-linkage is pushed relatively further away from the RC. In this planar RCM mechanism, links AF (AO), AC,

CE, and EH (EO) are the ground, input, connector, and output links, respectively. Point O is the RC. Links BG, FG, DG, and GH belong to parallelograms ABGF and DEHG for constraining the RCM function. To adapt to the 2 K-SLLS outer shape of the four-bar linkage, the lengths of links satisfy the following conditions to achieve the symmetric outer shape (2 K condition):

$$\begin{aligned} c &= f \\ b &= e \end{aligned} \tag{2}$$

The straight link that is rigidly connected to output link EH represents the cantilever that connects the DT-linkage and the surgical tool. The distance from the input joint to the RC is independent of the size of the linkage. Therefore, the major part of the mechanical structure is maintained distal from the RC, leaving a single cantilever in the region near the restricted space near the incision port. The mathematical proof of the RCM property is provided in Ref. [6].

The DT-linkage can also be derived from the planar Kempe focal point linkage [31], as shown in Fig. 2. The linkage is originated as part of a mathematical problem, in which the mobility conditions of highly constrained eight-piece linkage are investigated. The solutions are six classes of mobile linkages that are distinguished based on the link length relations, and the Kempe focal point linkage is a special case of one of those. The mobility condition of the Kempe focal point linkage is given by [32]

$$\begin{aligned} \frac{a_1}{a_2} &= \frac{c_2}{c_1} \\ \frac{b_1}{b_2} &= \frac{d_2}{d_1} \end{aligned} \tag{3}$$

When the DT-linkage is compared to the Kempe mechanism, links AF, AC, CE, and EH of the DT-linkage correspond to links LY, LM, MN, and NX of the Kempe mechanism, respectively. Links FG, BG, DG, and GH of the DT-linkage correspond to links YP, UP, VP, and PX of the Kempe mechanism, respectively. The virtual links, links FO and HO, of the DT-linkage correspond to the physical links, links YR and XR, of the Kempe mechanism. The RC O of the DT-linkage correspond to the focal point R of the Kempe mechanism. By comparing Figs. 1 and 2, Eq. (3) in terms of link lengths for the DT-linkage is rewritten as

$$\begin{aligned} \frac{b}{c-b} &= \frac{\overline{FG}}{\overline{BC}} = \frac{\overline{HO}}{\overline{EH}} \\ \frac{f-e}{e} &= \frac{\overline{CD}}{\overline{GH}} = \frac{\overline{AF}}{\overline{FO}} \end{aligned} \tag{4}$$

On the other hand, combining Eqs. (1) and (2) with similar triangles BCG, FGO, DCG, and HGO yields
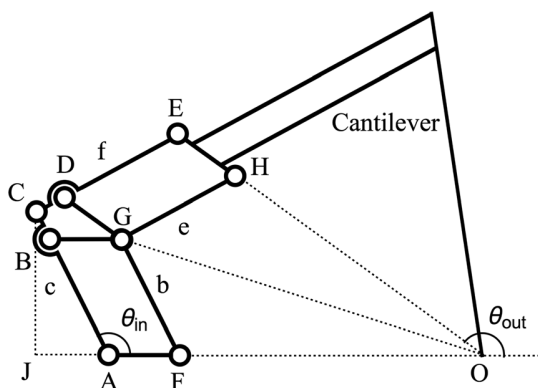

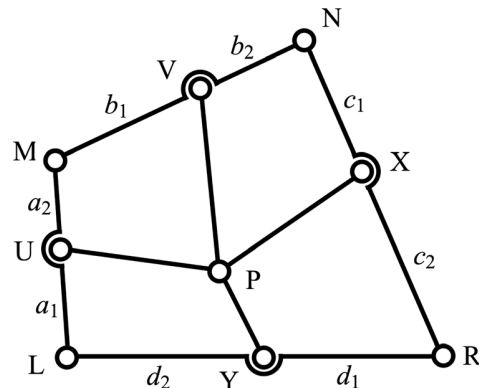Fig. 1 Conceptual design using the DT-linkage

Fig. 2 The planar Kempe linkage in its general form

$$\frac{\overline{AF}}{\overline{FO}} = \frac{\overline{BG}}{\overline{FO}} = \frac{\overline{BC}}{\overline{FG}} = \frac{\overline{CD}}{\overline{GH}} = \frac{\overline{DG}}{\overline{HO}} = \frac{\overline{EH}}{\overline{HO}} \qquad (5)$$

By comparing Eqs. (4) and (5), it is proven that an arbitrary DT-linkage unconditionally satisfies Eq. (4). Therefore, the DT-linkage is shown to be a special case of the Kempe mechanism by removing the focal point R.

Referring to Fig. 1, the input–output function of the RCM mechanism can be found readily as

$$\theta_{\text{out}} = \pi - 2\arctan\frac{\overline{CJ}}{\overline{JO}} = \pi - 2\arctan\frac{\overline{AC}\sin\theta_{\text{in}}}{\overline{AO} - \overline{AC}\cos\theta_{\text{in}}} \qquad (6)$$

where θ_{in} and θ_{out} are the input angle measured from link AO to AC counterclockwise and the output angle measured from AO to OE counterclockwise, respectively.

The limit in ROM, i.e., the minimum θ_{out}, is reached at the fully stretched-out configuration where links AC and CE are inline with each other. Link AC is perpendicular to line CO, thus the ROM is written as

$$\text{ROM} = 2\arcsin(\nu) \qquad (7)$$

where

$$\nu = \frac{\overline{AC}}{\overline{AO}} \qquad (8)$$

It is known that parallelograms encounter singularity when all links are collinear. Two identical auxiliary parallelograms, AA'F'F and DD'G'G, are introduced to constrain parallelograms ABGF and DEHG, respectively, as shown in Fig. 3. Links AA', FF', DD', and GG' are machined as part of links AC, FG, CE, and GH, respectively, and they are angularly displaced from the links they are attached to. Links A'F' and G'D' are introduced additionally to complete the auxiliary parallelograms. These auxiliary parallelograms are not in the singular configuration simultaneously with the existing ones, hence are constraining each other and remove singularity.

Another type of singularities is due to the virtual four-bar linkage OACE with the symmetry kite shape as shown in Fig. 1. The singularities happen when links OE and OA overlap, i.e.,

$$\angle OAC = \angle OEC = 0 \qquad (9)$$

and

$$\angle OAC = \angle OEC = \pi \qquad (10)$$

where links CE and CA overlap as well. The DT-linkage is designed to fold toward right from the fully stretched-out configuration as shown in Fig. 3. Therefore, the only singular configuration encountered is the case in Eq. (10). This singularity is also a
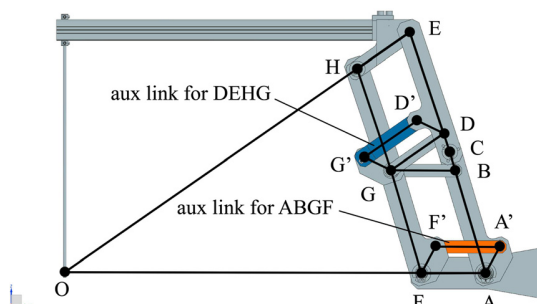
bifurcation point where two possible configurations can be reached by passing it, which are given by

$$\angle ACE = 0 \qquad (11)$$

or

$$\angle ACE = 2\angle OCA \qquad (12)$$

The former case is an undesired configuration where the output link stays overlapped with the ground axis. To overcome the singularity, constraints as shown in Eq. (12) are enforced.

The design of auxiliary mechanism for four-bar linkage is shown in Figs. 4 and 5. The figures are the right and left views, respectively. The auxiliary mechanism consists of a diagonal link group CG and a gear train. Referring to the two figures, links AC (lower) and CE (upper) that are synchronized are colored green. The diagonal link group CG with the translational joint is colored blue. Gears 2 (visible in Fig. 4 only) and 3 (visible in Fig. 5 only) are colored orange. The remaining gear, Gear 4 (visible in Fig. 5 only) is colored red.

Link group CG is coincident with the symmetry line CO of the four-bar linkage. It provides a reference for synchronizing $\angle OCE$ and $\angle OCA$. To accommodate for the change in distance between joints C and G, a translational joint is introduced to divide link CG into two parts, which are connected to joints C and G, respectively. The gear train consists of five gears. Gears 1 and 5 are rigidly attached to links AC and CE, respectively. Gears 2–4 rotate freely on link group CG. Gear 2 measures $\angle OCA$. Gear 3 is rigidly connected to and rotates with gear 2, in order to reach gear 4 on the other side of link group CG. Gear 4 measures $\angle OCE$. It engages with gear 3 to ensure the two angles are synchronized and stay in opposite in direction. Therefore, the constraint shown
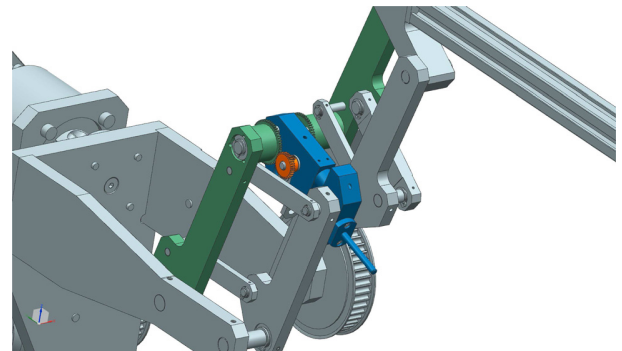

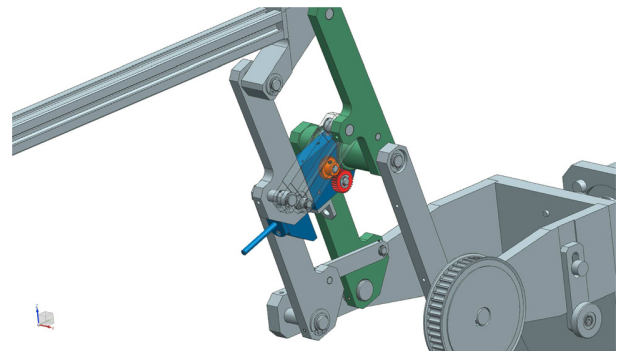**Fig. 4 Configuration of auxiliary mechanism for four-bar linkage—right view**

Fig. 5 Configuration of auxiliary mechanism for four-bar linkage—left view

Fig. 3 Configuration of auxiliary parallelograms

in Eq. (12) is enforced, and the four-bar linkage is fully constrained.

By permitting the linkage to cross the singular configuration, the DT-linkage is able to reach two extreme configurations, in which links AC and CE are inline with each other above and below the singular configuration. Therefore, the extended ROM of the DT-linkage is given, based on Eq. (7), by

$$ROM = 4\arcsin(\nu) \qquad (13)$$

3 Analysis of Footprint

The footprint of the DT-linkage is analyzed against the typical PB-linkage used in a number of machines [2,14–18]. Since the two-DOF RCM mechanism is formed by combining a planar RCM mechanism with a revolute joint, the overall device footprint is generated by rotating the planar area enclosed by the boundary of the planar RCM mechanism. For this reason, the analysis on the overall device footprint can be simplified as analysis on planar enclosed area of the planar RCM mechanism. Such area is called characteristic area for convenience. The details regarding the calculation of characteristic area are presented in the later paragraphs.

The circle centered at RC represents a restricted region with radius of R, where the RCM mechanisms and the cantilever are prevented from accessing, in order to yield more space around the incision for the surgical tools and human surgeons. Here, only the surgical tool mounted on the output link can access this region. The left and right solid lines within the circle represent the left and right boundaries of the ROM. The surgical tools in Fig. 6 are the middle position of the ROM. The configurations of the RCM mechanisms at RHS and LHS boundaries are as shown in Figs. 7 and 8, respectively.

The bold lines in the figures represent the simplified outlines of the RCM mechanisms, where the bold circles are the joints. The dashed lines indicate the ground axis. All other links or auxiliary mechanisms are hidden and the RCM mechanisms are assumed to be fully constrained. The DT-linkage is arranged in its fully folded configuration when reaching the midposition of the operational
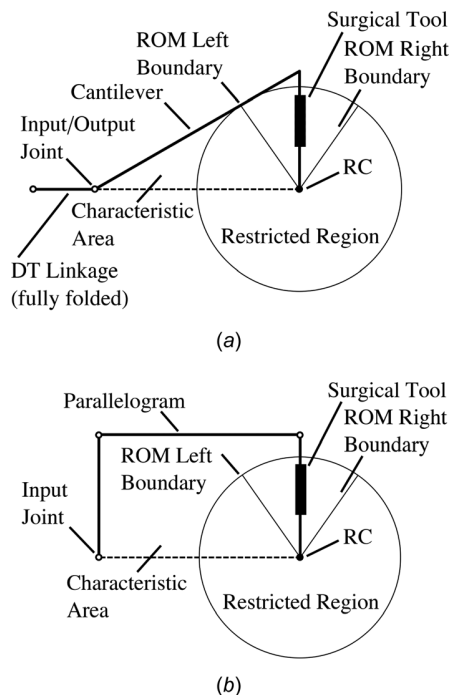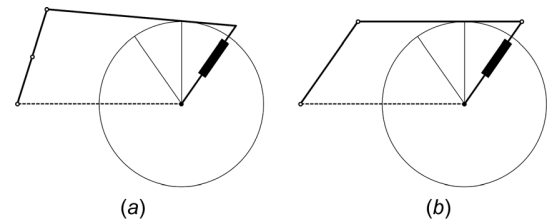

Fig. 7 Planar RCM mechanisms at right boundary of ROM: (a) DT-linkage and (b) PB-linkage
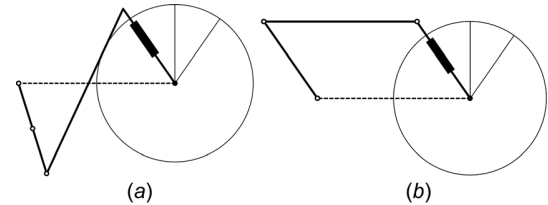

Fig. 8 Planar RCM mechanisms at left boundary of ROM: (a) DT-linkage and (b) PB-linkage

range. The shape of the cantilever is designed to be straight, although it can be further optimized. Note that a cantilever is necessary for the DT-linkage, as its output ROM (without the cantilever) does not align with the required one.

The geometries of the RCM mechanisms are set to be the minimum that do not invade the restricted region. For the DT-linkage, the length of surgical tool is minimized so that the cantilever is always tangent to the circle of the restricted region, as shown in Figs. 6–8. For the PB-linkage, the length of the surgical tool is set so that the connector link of the parallelogram is tangent to the circle of the restricted region when reaching the boundaries of the ROM, as shown in Figs. 7. As a result, the connector link of the PB-linkage is located above the circle at the midposition, as shown in Figs. 6.

The characteristic area is the area bounded by the RCM mechanisms, the cantilever, the surgical tool, and the ground axis. For example, in Fig. 6, the characteristic areas are the triangle and the rectangle for the DT-linkage and PB-linkage, respectively. In Fig. 8, the characteristic area of the DT-linkage is calculated as the sum of areas of two triangles. To evaluate the footprints of the RCM mechanisms over the ROM, the average value of the characteristic areas at the left, middle, and right positions are taken to assess the footprint of a design.

In the analysis, the radius R is varied from 30 to 300 mm, while the ROM is varied from 30 to 150 deg. The distance L between the input joints of the RCM mechanisms and RC is fixed at 400 mm. The average characteristic areas of the DT-linkage and PB-linkage with respect to R and ROM are presented in Figs. 9(a) and 9(b), respectively. The maximum average characteristic area is 995 cm^2 and 1332 cm^2 for the DT-linkage and PB-linkage, respectively. The minimum average characteristic area is 167 cm^2 and 121 cm^2 for the DT-linkage and PB-linkage, respectively.

The difference between the average characteristic areas of the PB-linkage and DT-linkage is shown in Fig. 10, with the maximum and minimum differences being 402 cm^2 and −330 cm^2, respectively. The triangular cyan region in top right corner of Fig. 10 is a region where both RCM mechanisms violate the restricted region. More than half of the combinations of ROM and radius, the average characteristic area of the DT-linkage is smaller than that of the PB-linkage. When the radius is greater than around 100 mm, the average characteristic area of the DT-linkage is smaller within the full range of ROM. The percentage of the difference is shown in Fig. 11, where only positive percentages are displayed. A positive percentage indicates the percentage of the average characteristic area reduced by the DT-linkage over that of the PB-linkage. The improvements are from 20% to 38.5%

Fig. 6 Planar RCM mechanisms at midposition of ROM: (a) DT-linkage and (b) PB-linkage
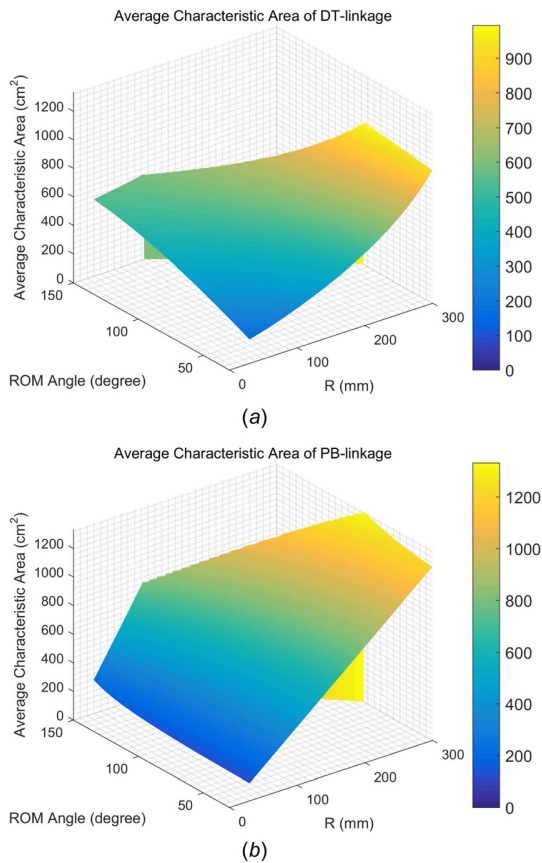
Fig. 9 Average footprints of RCM mechanisms: (*a*) DT-linkage and (*b*) PB-linkage

Fig. 10 Difference in characteristic areas of the RCM mechanisms

Fig. 11 Percentage difference in characteristic areas of the RCM mechanisms—DT-linkage supremacy region

Fig. 12 Skeletal prototype of two-DOF surgical arm

(1) the two-DOF RCM mechanism based on DT-linkage
(2) the three-DOF passive robotic arm for defining the position of RC in 3D space
(3) the base that holds the above-mentioned mechanisms

In the final prototype, the ROMs of the rotations around the first and second axes are 69 deg and 270 deg, respectively, satisfying the requirement in an abdominal MIS [13]. According to the input–output relation of the DT-linkage, as shown in Fig. 13, the effective working range is from 150 to 210 deg.

Figure 14 shows the two-DOF RCM mechanism with servos. The DT-linkage is at its upper limit position and the first axis revolute joint is in home position. The first axis mechanism is merely a servo. The second servo is mounted onto the frame of DT-linkage and drives the input link through pulleys. The timing belt is not shown. Note that the cantilever that is rigidly mounted to the output link of the RCM mechanism is not optimized for the smallest footprint.

The three-DOF passive robotic arm for defining the position of RC utilizes the SCARA structure. All three revolute joints on the passive arm are equipped with normally closed magnetic brakes to secure the defined horizontal position of the RC. The table-like

in a large area as shown in Fig. 11. The configuration where the average characteristic area of the DT-linage reaches the highest percentage difference is at ROM of 30 deg and radius of 174 mm. The footprints are 432 cm² and 703 cm², respectively. The percentage difference is 38.5%. Another advantage of the DT-linkage is the cantilever rigidly connected to the output link can be designed in any shape to accommodate actuators for driving surgical tools.

4 Prototyping

A scaled-down skeletal prototype of a two-DOF surgical arm based on the DT-linkage, as shown in Fig. 12, was developed to validate the conceptual design. The prototype consists of three mechanical parts:

Fig. 13 Input–output plot of the DT-linkage

Fig. 14 CAD model of the two-DOF RCM mechanism

structure underneath the elevation stage is the lockable mobile base with a cabinet to hold the electronic components.

Different configurations of the prototype two-DOF RCM mechanism are presented in Fig. 15. The RC is located at the lower end of the rod attached to the cantilever. The top left, top right, and bottom left figures correspond to the upper extreme, center of ROM and the lower extreme of the DT-linkage, respectively.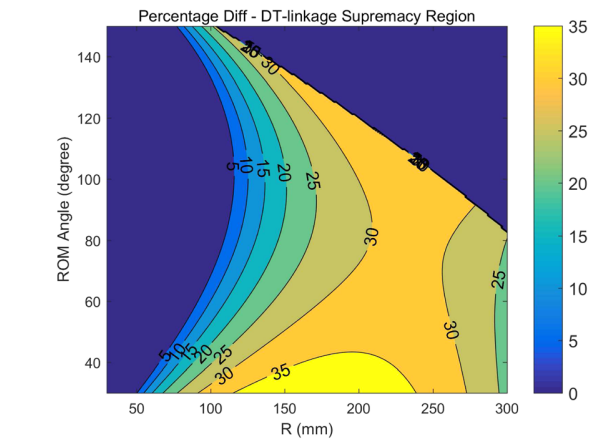 The first axis of rotation is in home position in these configurations. In bottom right figure, the first axis of rotation is maneuvered to one of its extreme, with the DT-linkage moved to the lower extreme.

Preliminary experiment was conducted to verify the positioning accuracy of the RC. Since the first axis of rotation of the prototype is merely a revolute joint, the experiment was conducted for the DT-linkage only. The experimental setup is shown in Fig. 16. The lenses of the camera, the DT-linkage, and the screen that displays the scales were adjusted in such a way that they are in three parallel planes. The position of the screen was adjusted according to
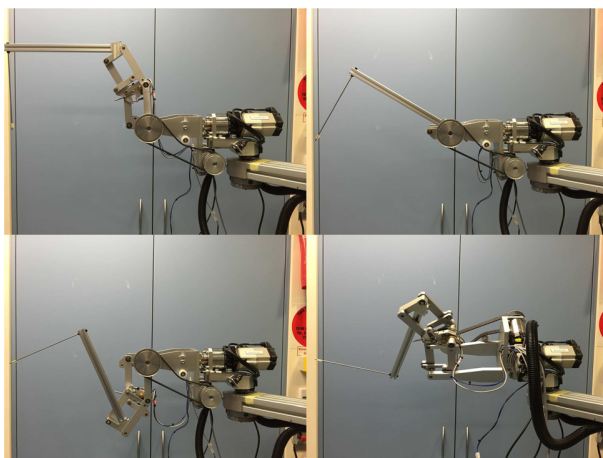
Fig. 15 Different configurations of the two-DOF RCM mechanism
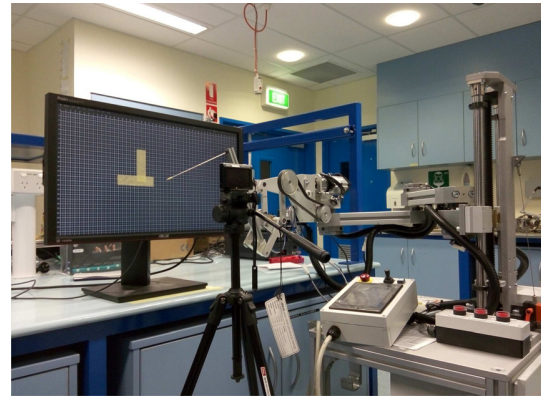
Fig. 16 The experimental setup
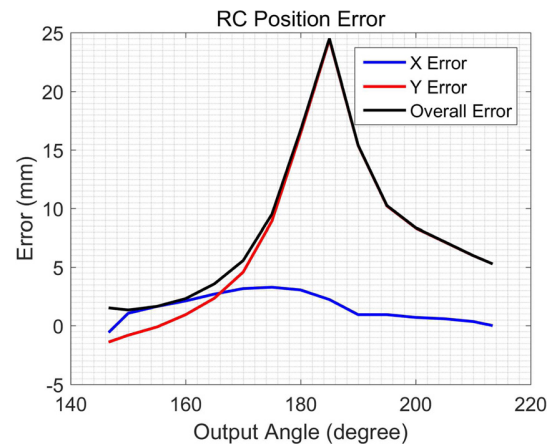
Fig. 17 RC position error of DT-linkage

the position of the revolute joint (first axis of rotation) of the RCM prototype, so that the center of the screen is coincident with the theoretical RC. Grids are displayed on the screen for measuring the position of the output RC of the DT-linkage. The position of the camera was adjusted in the same way, such that the center of the lenses is coincident with the theoretical RC.
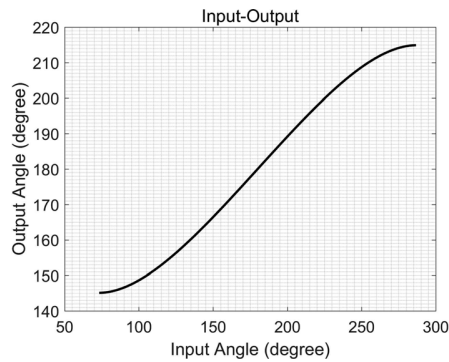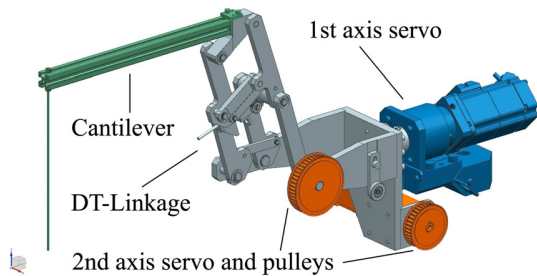
In the experiment, the DT-linkage was actuated from one end of its ROM to the other, with an interval of 5 deg. The purpose is to examine the positioning accuracy of the DT-linkage within its full ROM. Photos of the output rod of the DT-linkage were taken and the positions of the output RC (marked on the output rod) were read and recorded from the photos. The results are presented in Fig. 17. The *x* and *y* correspond to the horizontal and vertical directions, respectively. The overall error is the distance between the actual and the theoretical output RCs, which is calculated from the horizontal and vertical components.

Although the RCM of the DT-linkage is proven mathematically, the horizontal positioning error (<3.5 mm) and the vertical positioning error (<24.5 mm) were found while the maximum error appears close to where the DT-linkage is fully folded. The factors to these errors include the machining and assembly errors, backlashes in gear transmission, geometry misalignment, and the image errors due to the equipment errors due to the experiment setup. In the design and machining procedures, the lengths of links FG and GH require rounding. More significantly, some custom-made shafts were bent during the hardening process. Straightening process was carried out in the attempt to correct the bend, but it failed to restore the shafts to the perfectly straight condition, which in turn leads to geometry misalignment. In addition, it removed materials from the surfaces of the shafts, resulting in loose clearance fit on the joints that permits the links to wobble

around the shafts. These manufacturing issues together dominate the significant positioning error on the output RC of the prototype.

5 Conclusion

A new RCM mechanism, the DT-linkage, was introduced. The concept was proven mathematically and validated by experiments. The singularity of the planar RCM mechanism was analyzed and overcome by auxiliary mechanisms, so that the ROM of the RCM mechanism is doubled without increasing the footprint of the mechanism. A skeletal prototype of a surgical robotic arm based on the DT-linkage was developed. According to the footprint analysis, the DT-linkage reduces the footprint occupied by the linkage by 20–30%, as compared to that of the PB-linkage, in a large design area.

Acknowledgment

References

[1] Kuo, C.-H., and Dai, J. S., 2009, "Robotics for Minimally Invasive Surgery: A Historical Review From the Perspective of Kinematics," *International Symposium on History of Machines and Mechanisms*, Springer, Berlin, pp. 337–354.

[2] Madhani, A. J., Niemeyer, G., and Salisbury, J. K., Jr., 1998, "The Black Falcon: A Teleoperated Surgical Instrument for Minimally Invasive Surgery," 1998 IEEE/RSJ International Conference on Intelligent Robots and Systems, Victoria, Canada, Oct. 13–18, IEEE, Vol. 2, IEEE, pp. 936–944.

[3] Rininsland, H., 1999, "Artemis. A Telemanipulator for Cardiac Surgery," Eur. J. Cardiothorac. Surg., **16**(Suppl 2), pp. S106–S111.

[4] Taylor, R. H., Menciassi, A., Fichtinger, G., and Dario, P., 2008, "Medical Robotics and Computer-Integrated Surgery," *Springer Handbook of Robotics*, Springer, Berlin, pp. 1199–1222.

[5] Zong, G., Pei, X., Yu, J., and Bi, S., 2008, "Classification and Type Synthesis of 1-DOF Remote Center of Motion Mechanisms," Mech. Mach. Theory, **43**(12), pp. 1585–1595.

[6] Chen, C., and Pamieta, M., 2013, "Novel Linkage With Remote Center of Motion," 3rd IFToMM International Symposium on Robotics and Mechatronics Singapore, Oct. 2–4, Research Publishing Services, pp. 139–147.

[7] Michelin, M., Poignet, P., and Dombre, E., 2004, "Dynamic Task/Posture Decoupling for Minimally Invasive Surgery Motions: Simulation Results," 2004 IEEE/RSJ International Conference on Intelligent Robots and Systems, 2004 (IROS 2004), Sept. 28–Oct. 2, IEEE, Vol. 4, pp. 3625–3630.

[8] Locke, R. C., and Patel, R. V., 2007, "Optimal Remote Center-of-Motion Location for Robotics-Assisted Minimally-Invasive Surgery," 2007 IEEE International Conference on Robotics and Automation, Rome, Italy, Apr. 10–14, IEEE, pp. 1900–1905.

[9] Krupa, A., Morel, G., and De Mathelin, M., 2004, "Achieving High-Precision Laparoscopic Manipulation Through Adaptive Force Control," Adv. Robot., **18**(9), pp. 905–926.

[10] Ortmaier, T., and Hirzinger, G., 2000, "Cartesian Control Issues for Minimally Invasive Robot Surgery," 2000 IEEE/RSJ International Conference on Intelligent Robots and Systems, 2000 (IROS 2000), Takamatsu, Japan, IEEE, Vol. 1, pp. 565–571.

[11] Ghodoussi, M., Butner, S. E., and Wang, Y., 2002, "Robotic Surgery—The Transatlantic Case," IEEE International Conference on Robotics and Automation, 2002, ICRA'02, IEEE, Vol. 2, pp. 1882–1888.

[12] Guerrouad, A., and Vidal, P., 1989, "SMOS: Stereotaxical Microtelemanipulator for Ocular Surgery," Annual International Conference of the IEEE Engineering in Images of the Twenty-First Century, Engineering in Medicine and Biology Society, IEEE, pp. 879–880.

[13] Hempel, E., Fischer, H., Gumb, L., Höhn, T., Krause, H., Voges, U., Breitwieser, H., Gutmann, B., Durke, J., Bock, M., and Melzer, A., 2003, "An MRI-Compatible Surgical Robot for Precise Radiological Interventions," Comput. Aided Surg., **8**(4), pp. 180–191.

[14] Taylor, R. H., Funda, J., Grossman, D. D., Karidis, J. P., and LaRose, D. A., 1995, "Remote Center-of-Motion Robot for Surgery," U.S. Patent 5,397,323.

[15] Blumenkranz, S. J., and Rosa, D. J., 2001, "Manipulator Positioning Linkage for Robotic Surgery," U.S. Patent 6,246,200.

[16] Feng, M., Fu, Y., Pan, B., and Liu, C., 2012, "Development of a Medical Robot System for Minimally Invasive Surgery," Int. J. Med. Rob. Comput. Assisted Surg., **8**(1), pp. 85–96.

[17] Kim, K.-Y., Song, H.-S., Park, S.-H., Lee, J.-J., and Yoon, Y.-S., 2010, "Design and Evaluation of a Teleoperated Surgical Manipulator With an Additional Degree of Freedom for Laparoscopic Surgery," Adv. Rob., **24**(12), pp. 1695–1718.

[18] Zhu, W.-H., Salcudean, S., Bachmann, S., and Abolmaesumi, P., 2000, "Motion/Force/Image Control of a Diagnostic Ultrasound Robot," ICRA'00, IEEE International Conference on Robotics and Automation, San Francisco, CA, IEEE, Vol. 2, pp. 1580–1585.

[19] Stoianovici, D., Whitcomb, L. L., Mazilu, D., Taylor, R. H., and Kavoussi, L. R., 2006, "Remote Center of Motion Robotic System and Method," U.S. Patent 7,021,173.

[20] Lum, M. J., Friedman, D. C., Sankaranarayanan, G., King, H., Fodero, K., Leuschke, R., Hannaford, B., Rosen, J., and Sinanan, M. N., 2009, "The Raven: Design and Validation of a Telesurgery System," Int. J. Rob. Res., **28**(9), pp. 1183–1197.

[21] Bai, G., Li, D., Wei, S., and Liao, Q., 2014, "Kinematics and Synthesis of a Type of Mechanisms With Multiple Remote Centers of Motion," Proc. Inst. Mech. Eng., Part C, **228**(18), pp. 3430–3440.

[22] Solomon, T., and Cooper, T., 2006, "Multiply Strap Drive Trains for Robotic Arms," U.S. Patent 20,070,089,557.

[23] Haber, G.-P., White, M. A., Autorino, R., Escobar, P. F., Kroh, M. D., Chalikonda, S., Khanna, R., Forest, S., Yang, B., Altunrende, F., Stein, R. J., and Kaouk, J. H., 2010, "Novel Robotic da Vinci Instruments for Laparoendoscopic Single-Site Surgery," Urology, **76**(6), pp. 1279–1282.

[24] Thakre, A., Bailly, Y., Sun, L., Van Meer, F., and Yeung, C., 2008, "Is Smaller Workspace a Limitation for Robot Performance in Laparoscopy?" J. Urol., **179**(3), pp. 1138–1143.

[25] Long, H., Yang, Y., Jingjing, X., and Peng, S., 2016, "Type Synthesis of 1r1t Remote Center of Motion Mechanisms Based on Pantograph Mechanisms," ASME J. Mech. Des., **138**(1), p. 014501.

[26] Li, J., Xing, Y., Liang, K., and Wang, S., 2015, "Kinematic Design of a Novel Spatial Remote Center-of-Motion Mechanism for Minimally Invasive Surgical Robot," ASME J. Med. Dev., **9**(1), p. 011003.

[27] Hadavand, M., Mirbagheri, A., Behzadipour, S., and Farahmand, F., 2014, "A Novel Remote Center of Motion Mechanism for the Force-Reflective Master Robot of Haptic Tele-Surgery Systems," Int. J. Med. Rob. Comput. Assisted Surg., **10**(2), pp. 129–139.

[28] Kuo, C.-H., Dai, J. S., and Dasgupta, P., 2012, "Kinematic Design Considerations for Minimally Invasive Surgical Robots: An Overview," Int. J. Med. Rob. Comput. Assisted Surg., **8**(2), pp. 127–145.

[29] Chen, C., 2012, "Mechanical Remote Center of Motion," Australian Patent 2012902769.

[30] Muller, M., 1996, "A Novel Classification of Planar Four-Bar Linkages and Its Application to the Mechanical Analysis of Animal Systems," Philos. Trans. R. Soc. London B, **351**(1340), pp. 689–720.

[31] Kempe, A., 1877, "On Conjugate Four-Piece Linkages," Proc. London Math. Soc., **1**(1), pp. 133–149.

[32] Baker, J. E., and Hon-Cheung, Y., 1983, "Re-Examination of a Kempe Linkage," Mech. Mach. Theory, **18**(1), pp. 7–22.

3.1 Supplementary Information on the Prototype

With Eq. (12) defining the necessary mechanical constraint, several mechanical designs have been considered to materialise this constraint equation. The options are below.

1. Gear train (as used on the final prototype).

2. Cable.

3. Active control with additional actuator.

The gear train with simple spur gears is selected because of its compact size. The use of anti-backlash gears has been considered, which include the use of readily available stock models as well as designing customised anti-backlash mechanism with simple spur gears. However, the anti-backlash option is not implemented due to the large size and design complexity.

The cable option is abandoned on this prototype due to the complexity of cable tension/stiffness analysis and the need to introduce tensioners in the prototype. It is not until the completion of the cable tension/stiffness analysis (detailed in Chapter 4) that a cable-based design is feasible.

The active control scheme involves an additional actuator that is mounted at joints C or G and actively forces the DT-linkage to stay in the desired configuration. This option is not implemented as the additional actuator can significantly compromise the compact footprint of the DT-linkage. Also, the synchronisation between the additional actuator with the existing actuator is complicated.

Chapter 4

The Cable-Constrained Dual-Triangular Linkage

The prototype of the improved DT linkage presented in Chapter 3 has the following issues:

1. The gear-based auxiliary mechanism for constraining the four-bar linkage introduces backlash.

2. The auxiliary parallelograms occupy additional space between the input joint and the remote centre, which conflicts with the design concept of maximising such clearance.

3. The parallelograms occupy too many "layers" in the transverse direction, potentially introducing difficulties in design optimisation towards slimmer mechanism.

In addition, the footprint study conducted previously did not fully demonstrate the advantages of the DT linkage.

These drawbacks motivated the development of the cable-constrained DT linkage and the further investigation regarding the device footprint in this chapter. The specific objectives of the work were:

1. To design cable loops that fully-constrain the DT linkage.

2. To prove the functioning of the cable-based mechanism.

3. To quantify the footprint of the DT linkage through more approaches, and compare to that of the PB planar RCM mechanism.

The work presented is published in [112], and the full manuscripts is attached below. The major research outcomes are:

1. A new design of the DT linkage, consisting of three cable loops, was proposed.

2. The RCM function and the cable tension were proven mathematically through a constraint-based analysis.

3. The mathematical analysis was further verified through finite element analysis and a new prototype.

4. The footprint comparison was conducted, where the footprint was described through three approaches as the sweeping volume, the additional space needed to manipulate the RCM mechanism, and the weight of the RCM mechanism. The corresponding reduction in the footprint of the DT linkage were up to 35%, 83% and 80%, respectively.

5. The new cable-based prototype demonstrated larger clearance between the base joint and the remote centre than that in the previous prototype. Further, the transverse dimension was reduced and the backlash was eliminated.

The numerical calculations of cable tension and the mathematical simulations regarding the improved footprint comparison were conducted in Matlab.

Apart from the work published, another prototype (Figs. 4.1 and 4.2) with higher stiffness and better RC precision was constructed for future research and patent application. The second cable-based prototype features metal links, steel wire rope cable and precise ball bearings to replace the 3D-printed plastic links, polymer cable and bushings on the first
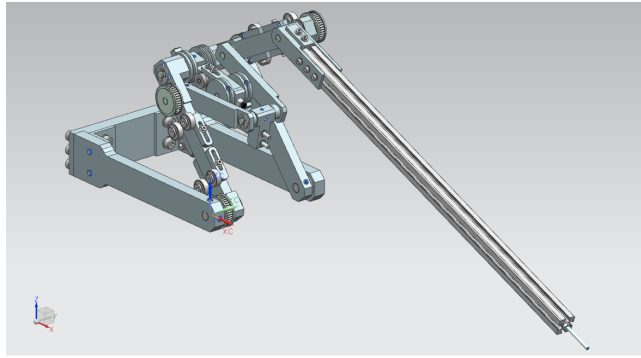
Figure 4.1: CAD model of the improved cable prototype.

Figure 4.2: The improved cable-based prototype.

cable-based prototype, respectively.

A cable linkage with remote centre of motion

S. Liu[a], B. Chen[a], S. Caro[b], S. Briot[b], L. Harewood[c], C. Chen[a],*

[a]Laboratory of Motion Generation and Automation, Room G50, 17 Alliance Lane, Monash University, Victoria 3800, Australia
[b]CNRS-IRCCyN, 1 rue de la Noë, BP 92101, Nantes Cedex 3 44321, France
[c]Suite 103, Epworth Freemasons Medical Centre, 320 Victoria Parade, East Melbourne, Victoria 3002, Australia

ARTICLE INFO

ABSTRACT

Mechanical remote centre of motion (RCM) mechanisms are often used to construct robotic minimally-invasive surgical manipulators, such that potential damage on the incision ports is eliminated. Current parallelogram-based RCM linkages (PB-linkage) typically have large footprints that compromise optimal surgical operations. A novel cable system with remote centre of motion is proposed to reduce the footprint. The RCM function of the cable system is proven mathematically. A new approach based on constraint analysis is conducted to determine the magnitudes of tension. The results are validated by finite element analysis, hence proves the use of constraint approach and the functioning of the cable system. Upon verification, the footprint of the cable linkage is compared to that of a PB-linkage in a simplified surgical scenario through three approaches. The quantitative analysis shows that the cable linkage has a smaller footprint in more than half of the design points in all approaches. A prototype is built for proofing the concept of the cable linkage.

1. Introduction

In a minimally-invasive surgery (MIS), the surgical instrument is constrained to have four degrees-of-freedom (DOF) through the incision port [1]: pitch, yaw, translation along the longitudinal axis and roll. The first three DOF in combine function as a spherical coordinate system to define the position of end-effector inside the patient's body. Remote centre of motion (RCM) mechanisms provide the two rotational DOF while permitting the surgical instrument to pivot around the incision port, hence eliminate potential damage to the incision port and promote the safety of MIS procedures [2].The RCM function refers to the capability of a mechanism to rotate its link(s) around a remote point without having a physical revolute joint at the point [3,4]. A remote centre (RC) can be constrained virtually or mechanically [5]. Mechanical RCM mechanisms are more reliable and considered suitable for clinical applications [3]. Mechanical RCM mechanisms that generate single RC and are applied on robotic MIS systems include isocentres [6], circular tracking arcs [7,8], parallelograms [9–14], synchronous transmissions [15] and spherical linkages [16]. In addition, there are RCM mechanisms that generate multiple RCs [17].

A commonly used approach to synthesise a two-DOF RCM mechanism is to combine a planar RCM mechanism with a revolute joint [3]. The axis of the revolute joint coincides with the one-DOF RC to add the second DOF. Such approach results in fully

---

decoupled rotational DOF, whose benefits include reduced complexity in control, promoted level of confidence in safety as well as rapid and intuitive manual positioning of the entire mechanism or individual DOF [1].

The translational DOF required in the MIS applications is often achieved by mounting an independent translational mechanism on the two-DOF RCM mechanism. A typical example of such three-DOF mechanism is the clinically-approved da Vinci series robotic surgical system [11,18,19]. In other approaches, various types of RCM mechanisms that also provide translational DOF are explored [20–22]. However, these mechanisms have coupled DOF [20], or are relatively bulky in terms of the transverse dimension [21], or have large sweeping volume upon rotation of the planar RCM mechanism around the revolute joint, due to the large enclosed area by the outer boundary of the planar RCM mechanism [22].

The parallelogram-based structure is widely used as the planar RCM mechanism in the robotic MIS systems [3]. However, there are footprint issues associated with the parallelogram-base linkages (PB-linkage), which the consequences being poor access for bedside assistance [19] and the compromise in optimal surgical functioning [23]. The term "footprint" is mostly referred to as the sweeping volume of the RCM mechanism, which is generated by the rotation of the planar RCM mechanism around the revolute joint. The sweeping volume is thus related to the area enclosed by the outer boundary of the planar RCM mechanism.

When the output link of the parallelogram is short, the output joint of the PB-linkage is positioned closely to the incision ports. Given that the space around an incision port is often crowded with robotic or manual surgical tools, the collision-free workspace is reduced and the chance of interference is increased. The transmission for the translational mechanism mounted on the output link of the PB-linkage goes through the output joint, causing further expansion in size.

In opposite case where a longer output link is used to displace the output joint away from the mechanism, the size of the parallelogram and thus the enclosed area is increased. The consequence being the increase in the sweeping volume, which again leads to increase in chance of interference. Apart from the sweeping volume, longer links occupy more space even when the linkage is stationary. It also increases the weight and inertia of the system. Quantitative analysis on the footprint of the PB-linkage though three approaches is presented in Section 5.

This paper proposes a cable linkage with RCM, in the attempt to address the footprint issue associated with the PB-linkage. The entire RCM mechanism is kept relatively faraway from the RC, when the distance between the input joint and the RC is given. A cantilever is rigidly mounted on to the output link. It is the only part of the entire RCM mechanism that is operated near the RC. Therefore, the cable system can leave more collision-free workspace for the neighbouring robotic surgical arms or human surgeons to operate. In addition, the enclosed area of the planar RCM is relatively small, resulting in a smaller sweeping volume. Further, the links are relatively short, which reduces the space taken by the links when stationary, and potentially reduce the weight and inertia of the mechanism. A comparison between footprint of the proposed linkage and the PB-linkage is presented in Section 5.

Cable-pulley mechanism provides advantages such as structure simplicity, compactness, light weight, low friction and low backlash [24]. Therefore it is widely applied on serial and parallel robotic manipulators, as summarised in [25] and [26], respectively. In MIS applications, the evolution from linkage-based da Vinci system [11] to cable-based da Vinci systems [18,19] shows significant deduction in the size of linkage. As such, the proposed planar RCM mechanism is developed based on cable-pulley mechanism.

Cable tension analysis is essential for proof of functioning of the cable linkage. Approaches for describing cable tension of cable-constrained open-chain linkage and multi-link parallel manipulator are available in [27] and [28], respectively. However, a more generalised approach based on mechanical constraint [29] is used in the analysis. The reason being that the proposed linkage is based on four-bar linkage and is affected by the singularity of an unconstrained four-bar linkage. The constraint approach provides indication on the constraint status of the mechanism, thus enable justification on the removal of singularity. The cable tension is solved as generalised force along mechanical constraints. Numerical solution of cable tension is obtained using QR decomposition and verified with static finite element simulation in ANSYS.

The rest of the paper is arranged as follows. Section 2 describes the design of the cable linkage and the proof of the RCM function. Section 3 applies the constraint-based analysis. Constraint equations are derived. Cable tension is solved and verified with finite element analysis. The functioning of the cable loops is hence proven. Section 4 calculates the minimum required cable stiffness to achieve a given overall stiffness of the linkage. Section 5 compares the footprints of the cable linkage and PB-linkage in a simplified surgical scenario. Section 6 introduces the prototype of the cable linkage.

2. The cable linkage with RCM

In this section, the design of cable linkage with RCM is presented, along with the proof of RCM under the condition that the cable is in tension.

2.1. Design of cable linkage

The design of the cable linkage with RCM is illustrated in Figs. 1 and 2, where the schematic diagram of links (without cable loops) and the full schematic diagram are presented, respectively. The cable linkage consists of eight links and seven pulleys that are arranged in three cable loops. As illustrated in Fig. 1, the links are AF, AC, CE, EH, BG, DG, CI and IG, respectively. Joint I is a passive prismatic joint while all other joints (indicated by the small circles) are revolute joints. Note that joints B and D do not divide links AC and CE, respectively. For convenience, links CI, IG and passive prismatic joint I are grouped and termed "diagonal link CG" in the later descriptions. Different configurations of the cable linkage are presented in Figs. 3 and 4. ROM in
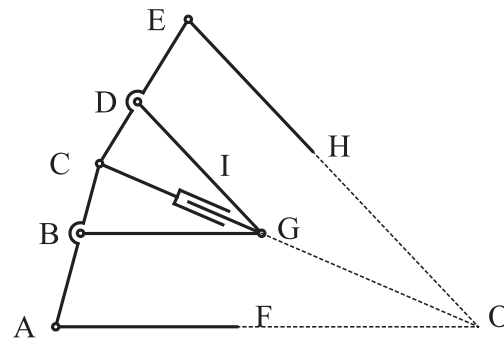
Fig. 1. Configuration of links.
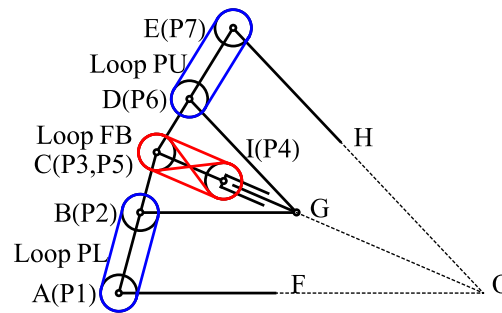
Fig. 2. Configuration of links and cable loops.

the figures stands for range of motion. The limits in ROM above and below the ground (AO), and the centre configuration where all links are overlapped with the ground are illustrated in Fig. 3. Two mid-point configurations in between the centre and two limits in ROM are illustrated in Fig. 4. Note that pulleys and cable loops are not drawn for clarity of figures. In Fig. 3, all labelled joints are for the centre configuration only, where all the links overlap with the ground while D, E and H are coincident with B, A and F, respectively.

Point O is the remote centre. Links AF, AC, CE and EH are the ground, input, connector and output links, respectively. Links AC and CE, with virtual links AO and EO, form virtual four-bar linkage ACEO. Links BG and DG constraint the motion of the linkage. Link CG is the diagonal link of the virtual four-bar linkage. It contains a passive prismatic joint, Joint I, to accommodate for the change in length of CG with respect to movement of linkage. The distance between Joints C and I is constant while the distance between Joints I and G changes. The shape and size of output Link EH can be optimised freely to suit specific MIS applications.

The three cable loops are called Loops PL, FB and PU, for the lower, middle and upper loops in Fig. 2, respectively. Loop PL connects Pulleys P1 and P2, which are rigidly attached to Links AF and BG, respectively. Loop FB connects Pulleys P3 to P5. Pulley P3 is rigidly attached to Link AC. Pulley P4 rotates freely at I. Pulley P5 is rigidly attached to Link CE. The cable connecting P4 and
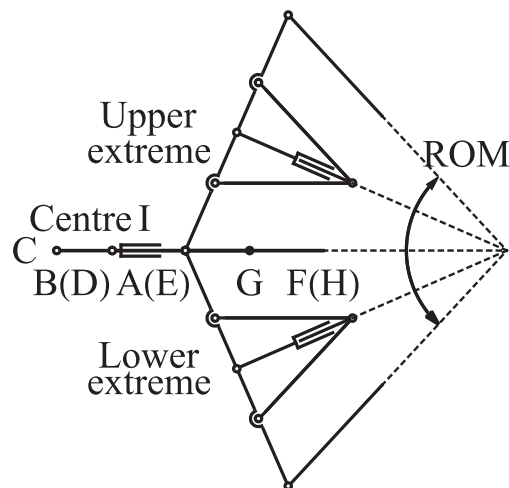
Fig. 3. Configurations at two extremes and centre of ROM.
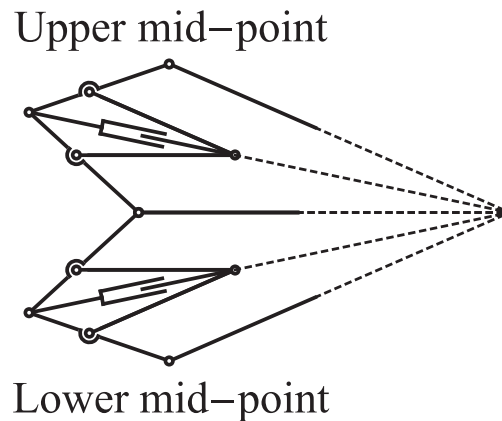
Fig. 4. Configurations at mid-points.

P5 has crossed configuration. Loop PU connects Pulleys P6 and P7, which are rigidly attached to Links DG and EH, respectively. Note that although there exist two forms of cable loop, which are the end-less tendon drive and the open-ended tendon drive, as classified in [25], they are not distinguished in the 2D design of the cable linkage. The reason is that the synchronised rotation of pulleys, which is the essential mechanical constraint of the cable linkage, can be achieved equivalently using two forms of cable loop under the assumptions of zero cable slippage elongation.

Loops PL and PU ensure Links BG and EH are parallel to AF and DG, respectively. Slip of cable on pulleys in Loops PL and PU ruins the parallel constraint, thus cause failure in maintaining the RCM function. Loop FB permits the cable linkage to pass the configuration where all links overlap with the ground, which is the singular configuration of an unconstrained four-bar linkage. Slip of cable in Loop FB does not affect the RCM function. In non-overlapped configurations, Loop FB is redundant. In the overlap configuration, slip of cable in Loop FB can cause the cable linkage to turn into an undesired configuration, where the output link stays coincident with the ground regardless of the input angle. Thus the position of the remote centre is not affected, despite the lost of mobility. More details regarding the singularity are described in the later paragraphs of this section.

The outer shape of the cable linkage, which is virtual four-bar linkage ACEO, is symmetrical to simplify the geometry. Links AC and CE have equal link length. Virtual links AO and CO have another equal link length, which is longer than that of AC and CE. Such structure ensures that the link length of the RCM mechanism is always smaller than the distance between the input joint A and the remote centre O. Hence the RCM mechanism is considered to be relatively faraway from the remote centre.

The geometry of the linkage is fully defined by two parameters, v and r, expressed mathematically as

$$v = \frac{L_{AC}}{L_{AO}} = \frac{L_{CE}}{L_{EO}} \tag{1}$$

and

$$r = \frac{L_{AC}}{L_{AB}} = \frac{L_{CE}}{L_{DE}} \tag{2}$$

To ensure Links AC and CE are shorter than AO and CO, v is smaller than one. With a given length AO, the range of motion (ROM) of the RCM mechanism is fully defined by v. As shown in Fig. 3, the centre (diagonal) line CO is perpendicular to ACE at two ends of ROM. Therefore, the ROM is

$$ROM = 4 \arcsin v \tag{3}$$

Parameter r is greater than one. It defines the geometry of four-bar linkage BCDG, where the length of Links BG and DG is

$$L_{BG} = L_{DG} = \left(1 - \frac{1}{r}\right) L_{AO} \tag{4}$$

Eq. (4) indicates that the larger the r, the longer Links BG and DG are. Four-bar linkage BCDG occupies additional space between Links AC, CE and the RC, thus a smaller r is desired to leave more clearance around the RC.

The configuration where all links overlap with ground is a bifurcation (singularity) configuration of an unconstrained four-bar linkage, where two possible configurations can be achieved upon crossing

$$\angle BCD = \angle BGD = 0 \tag{5}$$

Fig. 5. Cables in tension in upward motion.

and

$$\angle BCD = 2\angle BCG \tag{6}$$

where Eq. (6) can be equivalently expressed as

$$\angle BGD = 2\angle BGC \tag{7}$$

The first configuration shown in Eq. (5) is an undesired configuration where Links BG, DG and EH stay overlapped with ground (AF/AO) regardless of the input angle. In this case the mobility of the linkage is lost. Therefore, Eq. (6) or (7) needs to be enforced to fully constrain the linkage.

The cable linage achieves Eq. (6). In Loop FB, $\angle BCG$ and $\angle DCG$ are related to the relative rotations of Pulleys P3 and P5 with respect to diagonal link CG, respectively. Pulley P4 allows the two angles to be synchronised hence eliminates the chance of turning into Eq. (5). In this design, P3 and P5 are placed at Joint C to maximise the clearance between Links AC, CE and the RC.

The cable on one side of a loop is in tension in one direction of motion of the linkage. The sides of loops that are in tension in the upward and downward motions of the linkage are shown in Figs. 5 and 6, respectively.

2.2. Proof of RCM function

The proof of RCM function of the cable linkage is conducted based on the condition that the cable loops are functioning correctly hence the linkage is in the desired configuration. Such condition is proven in the Section 3. Given that an RCM mechanism requires a link to rotate around the remote centre, the proof is conducted through two steps:

1. Joint E rotates around O with a constant radius.
2. Point H rotates around O with a constant radius.

where E and H form output link EH.
To simplify the expressions, the following link lengths are assigned.

$$
\begin{aligned}
L_1 &= L_{AC} = L_{CE} = vL_{AO} \\
L_2 &= L_{AB} = L_{DE} = \frac{L_{AC}}{r} = \frac{vL_{AO}}{r} \\
L_3 &= L_{AF} = L_{BG} = L_{DG} = L_{EH} = \left(1 - \frac{1}{r}\right)L_{AO}
\end{aligned}
\tag{8}
$$

Fig. 6. Cables in tension in downward motion.
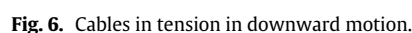
Table 1
List of generalised coordinates.

q	Definition	Reference
θ_1	Angle of Link AC	$\vec{AF}$
θ_2	Angle of Link BG and P2	$\vec{AC}$
θ_4	Angle of P4	$\vec{CG}$
θ_6	Angle of Link DG and P6	$\vec{CE}$
θ_7	Angle of Link EH and P7	$\vec{CE}$
θ_8	Angle of Link CG	$\vec{AC}$
θ_9	Angle of Link CE	$\vec{GC}$
L_{CG}	Distance between CG	n/a
x_H	Horizontal position of H	A
y_H	Vertical position of H	A

2.2.1. Generalised coordinates

To conduct the proof, ten generalised coordinates are assigned to fully describe the linkage. The generalised coordinates q are listed in Table 1.

θ_1 is the actuator input angle thus it is the independent generalised coordinate. All other generalised coordinates are dependent ones. The angles are measured with respect to the "previous" link, as shown in the "Reference", and in counter-clockwise (CCW) direction. There is no θ_3 and θ_5 since Pulleys P3 and P5 are rigidly attached to links and do not have their own independent rotation. The graphical representation of the generalised coordinates is shown in Fig. 7.

2.2.2. Step 1 - position of joint E

The distance between Joint E and O is

$$L_{EO} = \sqrt{(x_E - L_{AO})^2 + y_E^2} \tag{9}$$

where x_E and y_E are the horizontal and vertical positions of Joint E with respect to Joint A, respectively

$$x_E = L_1 \cos\theta_1 + L_1 \cos(\theta_1 + \theta_8 + \pi + \theta_9)$$
$$y_E = L_1 \sin\theta_1 + L_1 \sin(\theta_1 + \theta_8 + \pi + \theta_9) \tag{10}$$

where the π term is added as θ_9 is measured with respect to $\vec{GC}$ instead of $\vec{CG}$. The objective of Step 1 is to prove that L_{EO} is a constant. θ_8 and θ_9 need to be eliminated when Eq. (10) is substituted into Eq. (9).

θ_8 is calculated by subtracting the angle of Links AC with respect to ground from the angle of Link CG with respect to ground, i.e.

$$\theta_8 = \angle\vec{CG} - \angle\vec{AC} \tag{11}$$

Since Loop PL ensures that triangles BCG and ACO are similar triangles, the angle of Link CG with respect to ground is the same as the angle of diagonal line CO with respect to ground

$$\angle\vec{CG} = \angle\vec{CO} = -\arctan\frac{L_1 \sin\theta_1}{L_{AO} - L_1 \cos\theta_1} \tag{12}$$
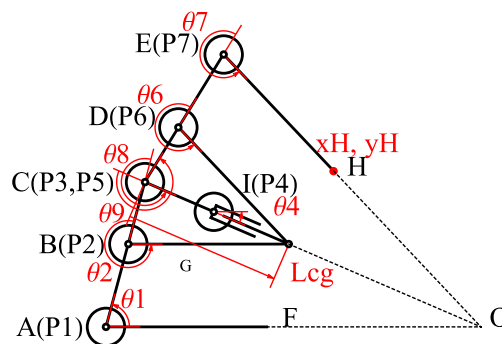
Fig. 7. Generalised coordinates.

The angle of Link AC with respect to ground is simply θ_1, thus

$$\theta_8 = \angle\vec{CG} - \angle\vec{AC} = -\arctan\frac{L_1 \sin\theta_1}{L_{AO} - L_1 \cos\theta_1} - \theta_1 \tag{13}$$

Due to the symmetrical structure of four-bar linkage BCDG

$$\theta_9 = \theta_8 = -\arctan\frac{L_1 \sin\theta_1}{L_{AO} - L_1 \cos\theta_1} - \theta_1 \tag{14}$$

Substituting Eqs. (10), (13) and (14) into Eq. (9) yields

$$L_{EO} = L_{AO} \tag{15}$$

Hence Joint E is proven to rotate around O.

2.2.3. Step 2 - position of point H

The position of Point H is determined through a similar approach as that of Joint E. The distance between Point H and O is

$$L_{HO} = \sqrt{(xH - L_{AO})^2 + y_H^2} \tag{16}$$

where x_H and y_H are

$$x_H = L_1 \cos\theta_1 + L_1 \cos(\theta_1 + \theta_8 + \pi + \theta_9) + L_3 \cos(\theta_1 + \theta_8 + \pi + \theta_9 + \theta_7)$$
$$y_H = L_1 \sin\theta_1 + L_1 \sin(\theta_1 + \theta_8 + \pi + \theta_9) + L_3 \sin(\theta_1 + \theta_8 + \pi + \theta_9 + \theta_7) \tag{17}$$

Given cable loop PU, the angles of Links EH and DG with respect to the ground are equal. Therefore, θ_7 and θ_6 are equal. From Eq. (7), the angle of Link DG with respect to ground is given by

$$\angle\vec{DG} = 2\angle\vec{CG} = -2\arctan\frac{L_1 \sin\theta_1}{L_{AO} - L_1 \cos\theta_1} \tag{18}$$

Hence

$$\theta_7 = \theta_6 = \angle\vec{DG} - \angle\vec{CE} = -2\arctan\frac{L_1 \sin\theta_1}{L_{AO} - L_1 \cos\theta_1} - (\theta_1 + \theta_8 + \pi + \theta_9) = \theta_1 - \pi \tag{19}$$

Substituting Eqs. (12), (13), (17) and (19) into Eq. (16) yields

$$L_{HO} = \frac{L_{AO}}{r} \tag{20}$$

Therefore L_{HO} is a constant. Since both L_{EO} and L_{HO} are constant, Link EH is proven to rotate around the remote centre and the cable linkage is proven to be an RCM mechanism.

3. Cable tension analysis

The RCM function proven in Section 2 is conducted under the condition that the cable loops are functioning. To achieve such condition, the following criteria must be achieved:

1. The cable loops (especially Loop FB) must not obstruct the movement of the links.
2. The two sides of a cable loop must be in tension in each direction of motion of the linkage, respectively.

The functioning of cable linkage is proven through constraint approach analysis. Criterion 1 is proven based on the constraint equations derived from cable loops. Criteria 2 is proven based on the solutions of cable tension. In addition, the cable linkage is also proven to be fully-constrained (singularity-free) based on the number of constraint equations derived. The full proof is presented in this section.

3.1. The constraint approach

Such constraint-based analysis is based on a generalised constraint approach [29], which is briefed below.

The dynamics of a constrained physical system is described as [30]

$$Q_i = Q_c + Q_e \tag{21}$$

where Q_i, Q_c and Q_e are the generalised inertia, constraint and external forces applied on the generalised coordinates q, respectively. The generalised constraint force Q_c applied on q is related to the mechanical constraints of the systems through

$$Q_c = -C_q^T \lambda \tag{22}$$

where λ is the Lagrange multiplier, which represents the generalised constraint force acting along the mechanical constraints. C_q is the derivative of the constraint matrix c_q with respect to the generalised coordinates q, which is

$$C_q = \frac{\partial c_q}{\partial q} \tag{23}$$

c_q represents the mechanical constraints of the system. Assuming that c_q and q have dimensions of m and n respectively, the dimensions of Q_c, C_q and λ are $n \times 1$, $m \times n$, and $m \times 1$, respectively. The cable linkage (one-DOF) is fully constrained when n equals $(m + 1)$. In the cable linkage, the constraints from cable loops are contained in c_q. Hence, c_q can be used to prove Criterion 1.

C_q and c_q also satisfy

$$\frac{\partial c}{\partial q_d} \dot{q}_d + \frac{\partial c}{\partial q_i} \dot{q}_i = C_{qd} \dot{q}_d + C_{qi} \dot{q}_i = 0 \tag{24}$$

where q_i and q_d are the independent and dependent generalised coordinates, respectively. C_{qi} and C_{qd} are the derivative matrices determined using q_i and q_d, respectively.

In static analysis, the generalised inertia force Q_i vanishes. Therefore, combining Eqs. (21) and (22) gives

$$Q_e = C_q^T \lambda \tag{25}$$

or equivalently

$$\begin{aligned} Q_{ei} &= C_{qi}^T \lambda \\ Q_{ed} &= C_{qd}^T \lambda \end{aligned} \tag{26}$$

where Q_{ei} and Q_{ed} are the generalised external forces applied on q_i and q_d, respectively.

Eq. (25) or (26) is used to determine the generalised constraint force λ acting along the mechanical constraints, when external load Q_e is given. Cable tension is contained in λ and thus proves Criterion 2. One constraint equation for each pair of pulleys needs be derived to determine the cable tension, for each direction of motion of the linkage.

The direction of such constraint force is dependent on the way in which the constraint equation c_q is written in. An example is given below. Consider an arbitrary constraint equation that is defined as

$$c_q = p_a - p_b \tag{27}$$

where p_a and p_b are the physical quantities of Bodies A and B, respectively, which are used to construct the constraint equation. In this case the λ determined using such constraint equation is the generalised constraint force acting on Body B by Body A. In the opposite case, if the positions of p_a and p_b are swapped in Eq. (27), λ will give the generalised constraint force acting on Body A by Body B.

3.2. Analysis on cable loops

In this analysis, it is assumed that the cable is inextensible and there is no slip between the cable and pulleys. All the bodies are assumed to be rigid bodies with zero mass.
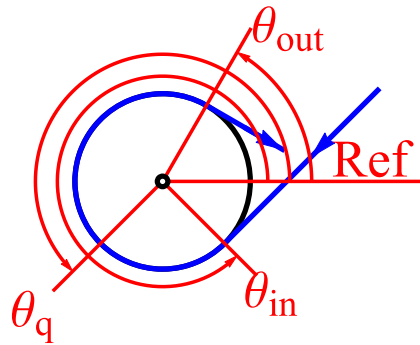
Fig. 8. Clockwise cable wrapping.

3.2.1. Constraint equations from cable loops

Given constant length of cable section connecting two pulleys and constant distance between pulleys, the sum of lengths of cable sections wrapping on two pulleys is also a constant. This is expressed mathematically as

$$L_{PA} + L_{PB} = L_{const.} \tag{28}$$

where L_{PA} and L_{PB} are the lengths of cable sections wrapping on arbitrary driving pulley PA and driven pulley PB. $L_{const.}$ is a constant that contains the overall length of cable section and the distance between two pulleys. Since the lengths of cable wrapping on pulleys are related to the rotation of pulleys and their adjacent links, generalised coordinates are embedded in Eq. (28).

Rearranging Eq. (28) into the form of Eq. (27) yields

$$(L_{const.} - L_{PB}) - L_{PA} = 0 \tag{29}$$

thus according to the definition of Eq. (27), Eq. (29) gives the force applied by the cable section attached to Pulley PB on that attached to PA.

Since the cable can wrap on a pulley in either clockwise or counter-clockwise direction, the expressions for L_{PA} and L_{PB} need to take into account the direction. The cases corresponding to clockwise and counter-clockwise cable wrapping are illustrated in Figs. 8 and 9, respectively.

In Figs. 8 and 9, "Ref" represents an arbitrary reference where the angles are measured with respect to. θ_{in}, θ_q and θ_{out} are the angle where the cable starts to wrap on the pulley, generalised coordinate and angle where cable leaves the pulley, respectively.

In the clockwise case, θ_{in} is the largest angle, followed by θ_q and θ_{out}. The length of cable from θ_{in} to θ_q is

$$L'_{CW} = R(\theta_{in} - \theta_q) \tag{30}$$

and the length of cable from θ_q to θ_{out} is

$$L''_{CW} = R(\theta_q - \theta_{out}) \tag{31}$$

In the counter-clockwise case, θ_{out} is the largest angle, followed by θ_q and θ_{in}. The length of cable from θ_{in} to θ_q is

$$L'_{CCW} = R(\theta_q - \theta_{in}) \tag{32}$$
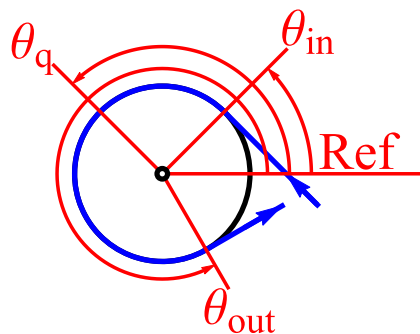
Fig. 9. Counter-clockwise cable wrapping.

Table 2
Cable and pulley angles for upward motion.

Pulley	θ_{in} (rad)	θ_q (rad)	θ_{out} (rad)	Direction	Reference
P1	n/a	0	$\theta_1 + \pi/2$	CW	$\vec{AF}$
P2	$\pi/2$	θ_2	n/a	CW	$\vec{AC}$
P3	n/a	0	$\theta_8 - \pi/2$	CCW	$\vec{AC}$
P4	$-\pi/2$	θ_4	$\pi/2 + \phi$	CCW	$\vec{CG}$
P5	$\pi/2 + \phi$	θ_9	n/a	CW	$\vec{GC}$
P6	n/a	θ_6	$\pi/2$	CW	$\vec{CE}$
P7	$\pi/2$	θ_7	n/a	CW	$\vec{CE}$

Table 3
Cable and pulley angles for downward motion.

Pulley	θ_{in} (rad)	θ_q (rad)	θ_{out} (rad)	Direction	Reference
P1	n/a	0	$\theta_1 - \pi/2$	CCW	$\vec{AF}$
P2	$-\pi/2$	θ_2	n/a	CCW	$\vec{AC}$
P3	n/a	0	$\theta_8 + \pi/2$	CW	$\vec{AC}$
P4	$\pi/2$	θ_4	$-\pi/2 - \phi$	CW	$\vec{CG}$
P5	$-\pi/2 - \phi$	θ_9	n/a	CCW	$\vec{GC}$
P6	n/a	θ_6	$-\pi/2$	CCW	$\vec{CE}$
P7	$-\pi/2$	θ_7	n/a	CCW	$\vec{CE}$

Table 4
Joints for constraint equations.

Joint	Path 1	Path 2
G	AB-BG	AC-CG
G	AB-BG	AC-CD-DG
H	x_H and y_H	AC-CE-EH

and the length of cable from θ_q to θ_{out} is

$$L''_{CCW} = R\left(\theta_{out} - \theta_q\right) \tag{33}$$

The θ_{in}, θ_q and θ_{out} for all the pulleys are summarised in Tables 2 and 3. Tables 2 and 3 correspond to the cable sections for upward and downward motions of the cable linkage, respectively, as illustrated in Figs. 5 and 6, respectively. ϕ is the additional constant angle introduced by crossed cable between P4 and P5. CW and CCW indicate clockwise and counter-clockwise directions, respectively. Substituting the θ terms from Tables 2 and 3 into Eq. (28) yields four constraint equations for each of the upward and downward motions of the cable linkage, respectively, which are between P1 and P2, P3 and P4, P4 and P5, and P6 and P7, respectively.

3.2.2. Constraint equation from joint positions

Apart from the cable loops, there are constraint equations from joint positions. Such constraint equations are derived based on shared joint position of two links. For example, position of Joint G can be derived from two paths: Links AB-BG and Links AC-CG, respectively. The position derived from the two paths must be identical

$$\begin{aligned} x_{G|BG} - x_{G|CG} &= 0 \\ y_{G|BG} - y_{G|CG} &= 0 \end{aligned} \tag{34}$$

where $x_{G|BG}$ and $y_{G|BG}$ are the positions derived from Links AB-BG, and $x_{G|CG}$ and $y_{G|CG}$ are the positions derived from Links AC-CG.

Six constraint equations are obtained, the paths are summarised in Table 4. Note that for Point H, the positions derived from path AC-CE-EH are equated to the generalised coordinates x_H and y_H.

3.3. Proof of Criterion 1

Criterion 1 states that with given cable length, the rotation of pulleys must be consistent with the rotation of the links they are attached to, otherwise it will jam the linkage. It can be readily seen that Criterion 1 is met in Loops PL and PU. The proof for Loop FB based on constraint approach is presented below.

The aim is to prove that the output rotation of the cable loop (θ_9) is consistent with the θ_9 derived from the links, as shown in Eq. (13), when a constant cable length from P3 to P5 is given.

Substituting the θ for P3 to P5 from Table 2 into Eq. (28) yields two constraint equations

$$R\left(\theta_4 - \left(-\frac{\pi}{2}\right)\right) + R\left(\left(\theta_8 - \frac{\pi}{2}\right) - 0\right) = L_{const.34} \tag{35}$$

for P3 and P4, and

$$R\left(\left(\frac{\pi}{2} + \phi\right) - \theta_9\right) + R\left(\left(\frac{\pi}{2} + \phi\right) - \theta_4\right) = L_{const.45} \tag{36}$$

for P4 and P5, where $L_{const.34}$ and $L_{const.45}$ are constant.

Summing Eqs. (35) and (36) gives

$$R\left(\pi + \theta_8 - \theta_9 + 2\phi\right) = L_{const.34} + L_{const.45} \tag{37}$$

Eq. (37) indicates that when given the correct cable length between P3 and P5 to start with, θ_9 equals θ_8 within full ROM of the cable linkage. Such outcome is consistent with Eq. (13), which means that the rotation of P5 is consistent with that of Link CE, thus Loop FB is not obstructing the movement of the linkage.

3.4. Constraint matrix c_q and derivative matrix C_q

Assembling the constraint equations derived from cable loops and joint positions yields the constraint matrices c_q. Individual constraint equations within the matrix are arranged in the following order

1. c_{qP12} for Pulleys P1 and P2 in Loop PL.
2. c_{qP34} for Pulleys P3 and P4 in Loop FB.
3. c_{qP45} for Pulleys P4 and P5 in Loop FB.
4. c_{qP67} for Pulleys P6 and P7 in Loop PU.
5. $c_{qGx|CG}$ for x position of Joint G from paths AB-BG and AC-CG.
6. $c_{qGy|CG}$ for y position of Joint G from paths AB-BG and AC-CG.
7. $c_{qGx|DG}$ for x position of Joint G from paths AB-BG and AC-CD-DG.
8. $c_{qGy|DG}$ for y position of Joint G from paths AB-BG and AC-CD-DG.
9. $c_{qHx|EH}$ for x position of Point H from generalised coordinate x_H and path AC-CE-EH.
10. $c_{qHy|EH}$ for y position of Point H from generalised coordinate y_H and path AC-CE-EH.

The constraint matrices are

$$c_{q1} = \begin{bmatrix} -R\left(\theta_1 + \theta_2\right) \\ R\left(\theta_4 + \theta_8\right) \\ R\left(\pi - \theta_4 - \theta_9 + 2\phi\right) \\ R\left(\theta_6 - \theta_7\right) \\ (L_1 - L_2)\cos\theta_1 - L_3\cos\left(\theta_1 + \theta_2\right) + L_{CG}\cos\left(\theta_1 + \theta_8\right) \\ (L_1 - L_2)\sin\theta_1 - L_3\sin\left(\theta_1 + \theta_2\right) + L_{CG}\sin\left(\theta_1 + \theta_8\right) \\ (L_1 - L_2)\left(\cos\theta_1 - \cos\left(\theta_1 + \theta_8 + \theta_9\right)\right) - L_3\left(\cos\left(\theta_1 + \theta_2\right) + \cos\left(\theta_1 + \theta_8 + \theta_9 + \theta_6\right)\right) \\ (L_1 - L_2)\left(\sin\theta_1 - \sin\left(\theta_1 + \theta_8 + \theta_9\right)\right) - L_3\left(\sin\left(\theta_1 + \theta_2\right) + \sin\left(\theta_1 + \theta_8 + \theta_9 + \theta_6\right)\right) \\ x_H - L_1\cos\theta_1 + L_1\cos\left(\theta_1 + \theta_8 + \theta_0\right) + L_3\cos\left(\theta_1 + \theta_8 + \theta_9 + \theta_7\right) \\ y_H - L_1\sin\theta_1 + L_1\sin\left(\theta_1 + \theta_8 + \theta_0\right) + L_3\sin\left(\theta_1 + \theta_8 + \theta_9 + \theta_7\right) \end{bmatrix} \tag{38}$$

for the upward motion of cable linkage. Note that for the constraint equations derived from cable loops, the constants associated with cable lengths are not included, as they do not appear in the derivative matrix C_q. For downward motion of the cable linkage, the joint constraint equations (last six) are the same. The cable constraint equations (first four) have negative signs to those in Eq. (38).

The derivative matrix C_q is given by

$$C_q = \begin{bmatrix} \frac{\partial c_q}{\partial \theta_1} & \frac{\partial c_q}{\partial \theta_2} & \cdots & \frac{\partial c_q}{\partial \theta_6} & \frac{\partial c_q}{\partial \theta_7} & \frac{\partial c_q}{\partial L_{CG}} & \frac{\partial c_q}{\partial x_H} & \frac{\partial c_q}{\partial y_H} \end{bmatrix} \tag{39}$$

where each column in the matrix contains the derivative of constraint matrix c_q with respect to one of the generalised coordinates. The derivative matrices C_{qi} and C_{qd} for independent and dependent generalised coordinates, respectively, are

$$C_{qi} = \left[\frac{\partial c_q}{\partial \theta_1}\right] \tag{40}$$

and

$$C_{qd} = \left[\begin{array}{cccccccc} \frac{\partial c_q}{\partial \theta_2} & \cdots & \frac{\partial c_q}{\partial \theta_6} & \frac{\partial c_q}{\partial \theta_7} & \frac{\partial c_q}{\partial L_{CG}} & \frac{\partial c_q}{\partial x_H} & \frac{\partial c_q}{\partial y_H} \end{array} \right] \tag{41}$$

which the two matrices are used for Eq. (26).

3.5. Constraint status of cable linkage

With ten generalised coordinates and ten constraint equations, the cable linkage seems to be over-constrained. However, certain retain constraint equations are redundant or vanish, resulting in fully-constrained one-DOF RCM mechanism. The cases where the links in non-overlapped and overlapped configurations are analysed separately.

In non-overlapped configurations, Loop FB is redundant. Loop FB introduces one generalised coordinate θ_4 and two constraint equations c_{qP34} and c_{qP45}. By excluding the generalised coordinate and constraint equations, the cable system is described by nine generalised coordinates with eight constraint equations. The cable linkage is fully constrained and has one DOF.

The overlapped configuration is the singular configuration of a four-bar linkage, thus $c_{qGx|DG}$ from four-bar linkage BCDG vanishes, resulting in fully-constrained cable linkage. According to the constraint approach, the elimination of $c_{qGx|DG}$ can be proven mathematically by observing zeros for its corresponding terms in C_q.

Writing θ_6 to θ_9, and L_{CG} in terms of θ_1, and substitute into C_q yields

$$\frac{\partial}{\partial q} c_{qGx|DG} = \left[\begin{array}{ccccccccc} 0 & 0 & 0 & 0 & 0 & 0 & 0 & 0 & 0 \end{array} \right] \tag{42}$$

where θ_6 to θ_9 are given by Eqs. (13), (14)and (19), respectively, and

$$L_{CG} = \left(1 - \frac{1}{r} \right) \sqrt{(L_{AO} - L_1 \cos \theta_1)^2 + (L_1 \sin \theta_1)^2} \tag{43}$$

Thus the cable linkage is described by ten generalised coordinates with night constraint equations. The cable linkage is fully constrained and has one DOF.

3.6. Calculation of cable tension

In the analysis, no external load is applied on Pulleys P2 to P6 and the passive prismatic joint I. Further, the upward and downward are simulated by applying vertical force F_{Hy} at point H. The torque on Joint E (τ_7) and horizontal force on Point H (F_{Hx}) are zero. The generalised external force Q_e applied on the generalised coordinates is given by

$$\begin{aligned} Q_e &= \left[\begin{array}{ccccccccc} \tau_1 & \tau_2 & \cdots & \tau_6 & \tau_7 & F_{CG} & F_{Hx} & F_{Hy} \end{array} \right] \\ &= \left[\begin{array}{ccccccc} \tau_1 & 0 & \cdots & 0 & 0 & 0 & F_{Hy} \end{array} \right] \end{aligned} \tag{44}$$

where τ_1 is the actuator input torque.

Since the actuator input torque τ_1 is unknown, Eq. (26) is used instead of Eq. (25), such that the constraint force can be calculated based on given τ_7, F_{Hx} and F_{Hy}, and then determine τ_1 using the constraint force λ. The corresponding Q_{ei} and Q_{ed} are

$$Q_{ei} = \tau_1 \tag{45}$$

and

$$Q_{ed} = \left[\begin{array}{cccccc} 0 & \cdots & 0 & 0 & 0 & 0 & \mp F_{Hy} \end{array} \right] \tag{46}$$

According to Eq. (26), the constraint force under given generalised external force is

$$\lambda = C_{qd}^{-T} Q_{ed} \tag{47}$$

Following Section 3.5, Eq. (47) at the overlapped and non-overlapped configurations is solved separately, which yields analytical and numerical solutions, respectively.

3.6.1. Analytical solution of λ at overlapped configuration

At the overlapped configuration, Eq. (47) which is solved with $c_{qGx|DG}$ is excluded from C_{qd}. The dimension of C_{qd} is 9×9 hence can be inversed directly. The analytical solution of cable tension, which are the first four elements in the constraint force λ, is given by

$$\lambda_1 = \begin{bmatrix} -\frac{F_{Hy}L_{AO}(-1+r+v+rv)}{rR(1+v)} \\ -\frac{F_{Hy}vL_{AO}}{rR} \\ -\frac{F_{Hy}vL_{AO}}{rR} \\ -\frac{F_{Hy}L_{AO}(-1+r)}{rR} \end{bmatrix} \tag{48}$$

for the upward direction of motion, and

$$\lambda_2 = -\lambda_1 \tag{49}$$

for the downward direction of motion. In both λ, the first to fourth rows correspond to cable tension between P1 and P2, P3 and P4, P4 and P5, and P6 and P7, respectively.

In Eq. (48), since F_{Hy} is negative, r is greater than 1, and R and v are positive, all the elements are positive. As such, the cable forces within Loops PL, FB and PU are all tension. Similarly, in Eq. (49), since F_{Hy} is positive, the cable forces are all positive. Hence, the cable loops are in tension at the overlapped configuration in both directions of motion of the cable linkage.

3.6.2. Numerical solution of λ at non-overlapped configuration

At the non-overlapped configurations, the redundant constraints cannot be removed, as cable tension needs to be solved. The dimension of C_{qd} is 10×9 and cannot be inversed directly. QR decomposition is applied to obtain the numerical solution

$$C_{qd} = \begin{bmatrix} Q_1 & Q_2 \end{bmatrix} \begin{bmatrix} R_1 \\ 0 \end{bmatrix} \tag{50}$$

where θ_6 to θ_9, and L_{CG} in C_{qd} are represented in terms of θ_1 before QR decomposition is applied. Eq. (47) is written with Q_1 and R_1 as

$$\lambda = Q_1 R_1^{-T} Q_{ed} \tag{51}$$

The numerical solution of constraint force is plotted in Fig. 10, for full ROM of a sample cable linkage whose dimensions are listed in Table 5. The numerical solutions are identical for the upward and downward motions of the cable linkage.

In Fig. 10, P12, P34, P45 and P67 represent the cable tension in between Pulleys P1 and P2, P3 and P4, P4 and P5, and P6 and P7, respectively. The maximum cable tension is observed at the overlapped configuration. The magnitudes in Loops PL (P12), FB (P34 and P45) and PU (P67) are 119.1 N, 52.48 N, and 38.4 N, respectively, which agree with the analytical solutions. The cable tension P34 and P45 are identical, which also agrees with the analytical solution. The minimum tension are observed at both ends of ROM. The numerical solution indicates that the cable tension in all loops is positive within the full ROM.

3.6.3. Verification of cable tension and proof of Criterion 2

The numerical solution obtained from the constraint approach is verified with static rigid body simulation conducted using ANSYS Rigid Dynamics package, with a 2D model of the same sample cable linkage. The model used is shown in Fig. 11.
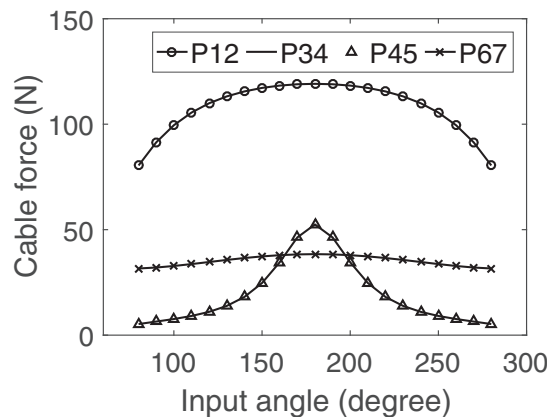
Fig. 10. Numerical solution of λ for sample cable linkage.

Table 5
Dimensions of sample cable linkage.

Parameters	Magnitude
L_{AO} (mm)	400
v	0.3
r	1.220
L_1 (mm)	120
L_2 (mm)	98.4
L_3 (mm)	72
R (mm)	15
F_{Hy} (N)	∓ 8

In the 2D model, links are used to mimic cable sections. The links are connected to pulleys with revolute joints, such that only tension and compression are allowed.

The cable tension in one side of the cable loop is obtained by summing the magnitudes of tensile and compressive of the two links which are connected to the same pulley. To justify the direction of cable force, the joint force at the link corresponding to the cable that is expected to be in tension must be tension as well. The external force F_{Hy} is simulated by a remote force applied at the tip of Link EH.

The cable tension obtained through simulation is compared with the calculated results in Figs. 12 and 13. The legends with "S" correspond to the simulation results.

The comparison indicates that the cable tension in Loops PL and PU, as well as the actuator input torque τ_1 obtained through the constraint approach is accurate. In Loop FB, exact solution is obtained at the overlapped configuration. The errors are relatively large towards two ends of the ROM, but the trend in the change in cable tension with respect to input angle is well captured. Therefore, the cable tension calculated from the constraint approach is verified, and it can be concluded that Criterion 2 for functioning of cable loops is proven.
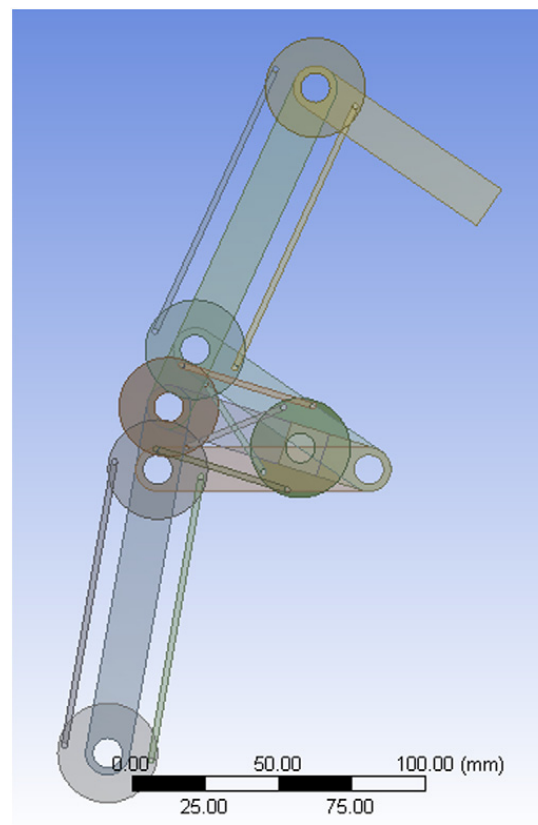
Fig. 11. 2D model in ANSYS.
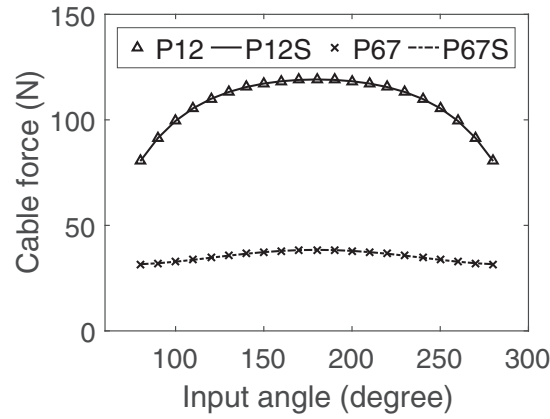
Fig. 12. Comparison of cable tension in Loops PL and PU.

4. Calculation on cable stiffness

The stiffness of the cable linkage is defined as the deformation of Point H under external load

$$k = \frac{F_{Hy}}{dy_H} = \frac{8\text{N}}{5\text{mm}} = 1.6\text{N/mm} \tag{52}$$

The stiffness of the cable must be sufficient to achieve the overall stiffness. Since cable tension and elongation change with respect to the movement of the linkage, the maximum value is determined as the minimum required cable stiffness

$$k = \max\left(\frac{\lambda_i}{dL_i}\right) \tag{53}$$

where k is the minimum required cable stiffness in the cable loop. λ_i and dL_i are the cable tension at different actuator input angle and its corresponding elongation, respectively.

Due to the assumption of inextensible cable, conventional definition of elongation, which is defined as deformation of cable, cannot be applied in the analysis. Here, the elongation is defined as the infinitesimal travel distance of cable with respect to infinitesimal displacement at Point H dy_H. The derivation of cable elongation is presented as follows.

The travel distance of cable is related length of cable wrapping on pulley and hence can be written in terms of generalised coordinates

$$dL = \text{function}\,(R, \quad \theta_{in}, \quad \theta_q, \quad \theta_{out}) \tag{54}$$

Fig. 13. Comparison of cable tension in Loop FB.

where the function is the suitable equation among Eqs. (30) to (33). θ angles are listed in Table 2 or 3. The mathematical expressions are (use P1, P3 and P6 for upward motion as examples)

$$dL_{PL} = Rd\theta_1$$
$$dL_{FB} = Rd\theta_8$$
$$dL_{PU} = Rd\theta_6 \tag{55}$$

where dL_{PL}, dL_{FB} and dL_{PU} are the infinitesimal cable travel in Loops PL, FB and PU, respectively. $d\theta_1$, $d\theta_8$ and $d\theta_6$ are the infinitesimal change in generalised coordinates.
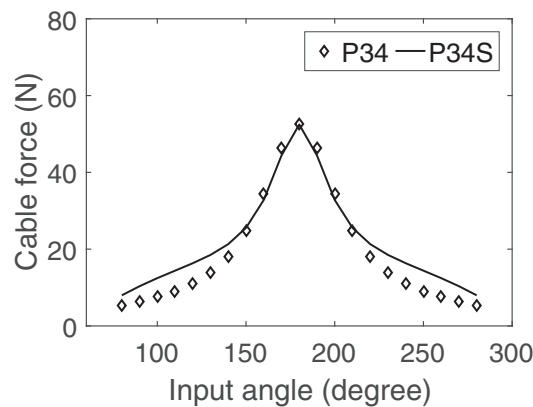
Eq. (55) needs to be further related to dy_H using Eq. (24). Rearranging yields

$$dq_d = -C_{qd}^{-1}C_{qi}dq_i \tag{56}$$

where dq_d and dq_i are the infinitesimal change in dependent and independent generalised coordinates, respectively. dy_H, $d\theta_8$, and θ_6 are contained in dq_d, while $d\theta_1$ is dq_i. Eq. (56) writes $d\theta_1$ in terms of dy_H. All other dependent generalised coordinates are written in terms of $d\theta_1$ and hence related to dy_H.

Eq. (56) is solved numerically using QR decomposition as

$$dq_d = -R_1^{-1}Q_1^T C_{qi}dq_i \tag{57}$$

where Q_1 and R_1 are obtained from Eq. (50). Substituting Eq. (57) into Eq. (55) yields the infinitesimal travel distance of cable in the cable loops. Further substituting such infinitesimal travel distance of cable into Eq. (53) gives the minimum required cable stiffness corresponding to the overall system stiffness. The results are illustrated in Fig. 14.

The minimum required cable stiffness are 240.5 N/mm, 137.7 N/mm and 77.51 N/mm for Loops PL, FB and PU, respectively. In all three cable loops, the largest k are observed at the overlapped configuration. The pattern of change in k with respect to input angle in Fig. 14 is very similar to the pattern of change in tension with respect to input angle in Fig. 10, which means the cable tension is the dominating factor in stiffness.

5. Comparison on device footprint

For a 2-DOF RCM mechanism based on the cable linkage, the footprint is described through three approaches

1. The sweeping volume of linkage.
2. The space behind the input joint to permit the rotation of input link.
3. The volume of links.

In this section, the footprint of cable-linkage is compared to that of a PB-linkage through the above-mentioned approaches.

The comparison of footprint is conducted mathematically under a simplified surgical scenario, as shown in Figs. 15 and 16, for the cable linkage and PB-linkage, respectively. Five configurations of both RCM mechanisms are shown, which are the two extremes in ROM, centre and two mid-point configurations as presented in Figs. 3 and 4.

In the simplified surgical scenario, the incision port is Point O. The ROM to be achieved is symmetric around the ground axis. R_C is a coefficient less than one. It gives the radius of the circular region in terms of distance L_{AO}, where the links (except for the
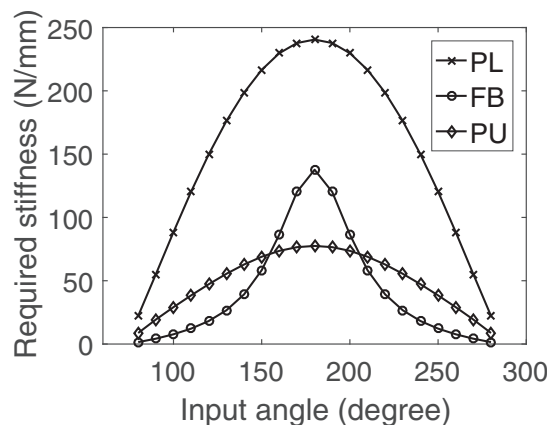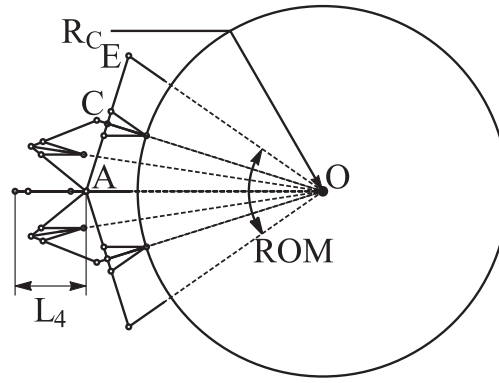

Fig. 14. Cable stiffness.

Fig. 15. Cable linkage in surgical scenario.

output link) of the RCM mechanisms are not allowed to enter such region. The region with R_C is set, such that more clearance near the incision port is left for the output links of multiple surgical arms and human surgeons to occupy.

L_{AO} is the same for both RCM mechanism. The ROM is changed from 30 to 120°. R_C is changed from 0.5 to 0.825. The dimensions and hence the footprints of the RCM mechanisms are calculated based on the given set of ROM and R_C.

For the cable linkage, the lengths of input and connector links (AC and CE) are determined from the ROM using Eq. (3). The lengths of BG and DG are calculated from Eq. (4), where r is assumed to be 1.22 and not changed in the simulation. For the PB-linkage, the length of input link AC is the same as the radius defined by R_C and L_{AO}, such that the output joint C is just on the edge of the circle. The length of connector link BC equals L_{AO}.

The results of the comparison are presented as the percentage difference of the footprint of cable linkage, over that of the PB-linkage, expressed as

$$\delta = \frac{f_{CL} - f_{PB}}{f_{PB}} \times 100\% \tag{58}$$

where f_{CL} and f_{PB} are the footprints of the cable linkage and PB-linkage, respectively.

5.1. Approach 1

In MIS applications, a planar RCM mechanism with smaller enclosed area is desired, such that the sweeping volume and the chance of collision between surgical arms are reduced.

In Approach 1, the footprint is described as the characteristic enclosed area. Such characteristic enclosed area is calculated by summing the four out of five configurations in Figs. 15 and 16, such that the change in enclosed area with respect to movement of linkage is taken into account. The overlapped configuration is not considered, as the enclosed area is zero. The mathematical expression is

$$f_1 = f_{top} + f_{mid-top} + f_{mid-bottom} + f_{bottom} \tag{59}$$

where f_1 is the characteristic enclosed area and the four remaining f terms are the enclosed area at four configurations, respectively. The enclosed area of the cable linkage and PB-linkage is defined by four-bar linkage ACEO and parallelogram ABCO in Figs. 15 and 16, respectively. The results are illustrated as a contour plot in Fig. 17.
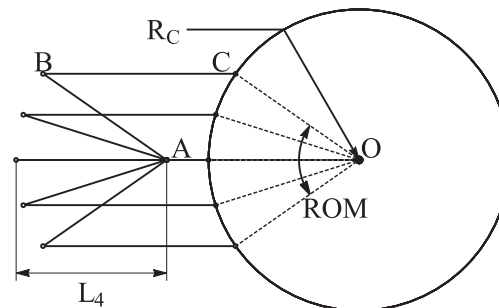

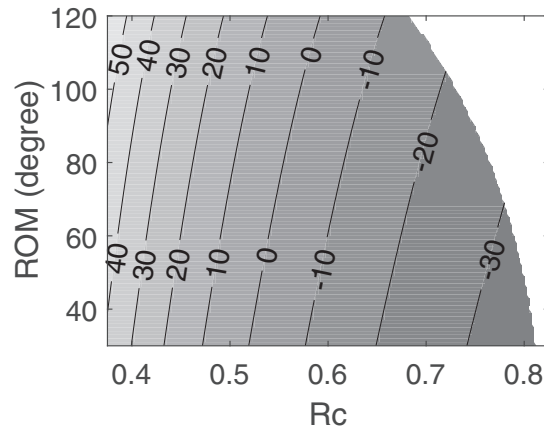**Fig. 16.** PB-linkage in surgical scenario.

Fig. 17. Percentage difference in footprint - Approach 1.

The blank region at the top right corner of Fig. 17 is where the cable link fails to stay outside the radius with given R_C. The edge of such region corresponds to the configuration of the cable linkage, where Joint G is on the edge of the circle, as illustrated in Fig. 15.

The result reveals that the enclosed area of the cable linkage is smaller than that of the PB-linkage in about half of the design points (sets of ROM and R_C). The cable linkage has smaller enclosed area at large R_C (>0.5). The smallest enclosed area is achieved at the maximum R_C of 0.81, and the corresponding percentage difference is -35 %. Cable linkage has a relatively smaller enclosed area because its geometry is fully defined by the ROM (when r is given). In the contrast, the length of Links AB and CO and hence the footprint of the PB-linkage increase with R_C.

5.2. Approach 2

Both RCM linkage require additional clearance behind input joint A to allow the movement of linkage. As such, the region needs to be kept clear during the operation. A large region will increase the space needed to maneuver the linkage. In addition, a large region requires a larger base to hold the RCM mechanism, thus increases the overall dimension of the robotic manipulator.

The footprint in terms of the aforementioned region is represented by the sweeping L_4 in Figs. 18 and 19 around Joint A and behind Joint A. For cable linkage, L_4 equals L_{AC}. Link AC is behind Joint A when actuator input angle is within $\pi/2$ to $3\pi/2$. For PB-linkage, L_4 equals the length Link AB and thus the radius of circle. Link AB sweeps behind Joint A in the full ROM. The mathematical expressions are

$$f_{CL2} = \frac{1}{2}\pi L_4^2$$
$$f_{PB2} = \frac{ROM}{2\pi}\pi L_4^2 \tag{60}$$

The results are illustrated as a contour plot in Fig. 20.

The result shows that the footprint (Approach 2) of the cable linkage is smaller than that of the PB-linkage in more than half of the design points. The maximum reduction in footprint is 83% at ROM of 30° and R_C equals 0.8. The footprint of the cable linkage is smaller in the cases where ROM is small and/or R_C is large. On the other hand, since the dimension of the cable linkage is defined by the ROM, the footprint is large at large ROM and/or small R_C.
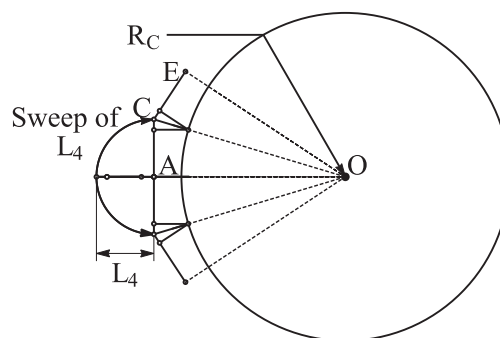
Fig. 18. Cable linkage in surgical scenario.
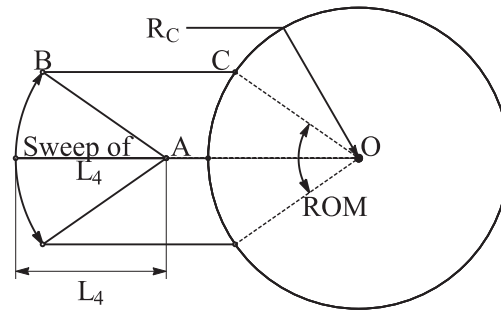
Fig. 19. PB-linkage in surgical scenario.
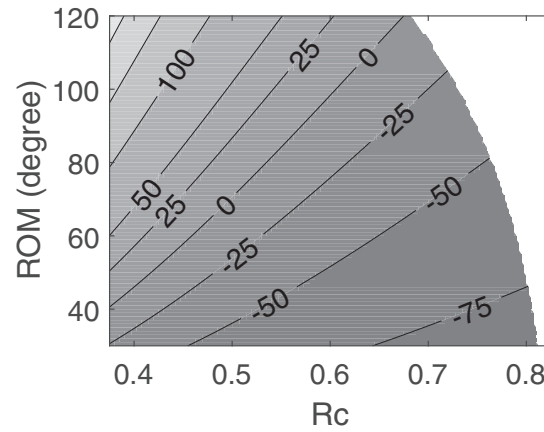
Fig. 20. Percentage difference in footprint - Approach 2.

5.3. Approach 3

There are cases in MIS applications where a surgical manipulator stays stationary while the other robotic arms or human surgeons are conducting manipulations. Therefore, the footprint in terms of the volume taken by the stationary links themselves must be taken into account.

Since the volume of the links is proportional to the length of links, the sum of lengths of links is used as the measurement of footprint in Approach 3. For cable linkage, the links involved are Links AC, CE, BG and DG. Diagonal link CG is not considered as it is enclosed by BG and DG. For PB-linkage, the links involved are Links AB and BC. The mathematical expressions are

$$f_{CL3} = L_{AC} + L_{BG} + L_{DG} + L_{CE} \tag{61}$$
$$f_{PB3} = L_{AB} + L_{BC}$$

The results are illustrated as a contour plot in Fig. 21.
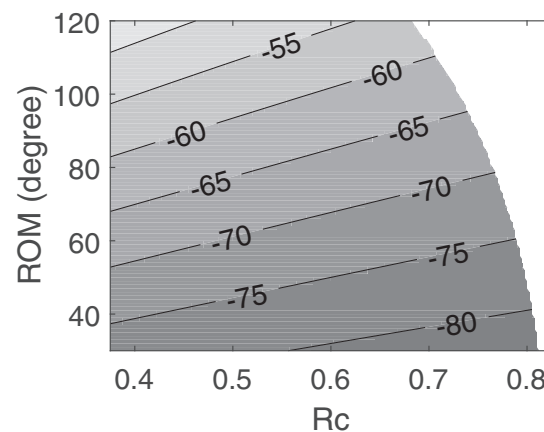
Fig. 21. Percentage difference in footprint - Approach 3.

The figure shows that the footprint (Approach 3) is smaller than that of the PB-linkage in all the achievable design points. The percentage reduction in footprint varies between −50% and −80 %, which is significant. Again, the cause of the difference is the fact that the footprints of two RCM mechanisms are dependent on ROM and R_C, respectively, while irrelevant to the other.

The comparison in footprint through three approach shows that the cable linkage has a smaller sweeping volume and requires less space behind the input joint in more than half of the design points. In addition, the overall lengths of the links are shorter in all design points, resulting in smaller and lighter linkage. Therefore it can be concluded that the cable linkage has advantages over the PB-linkage in terms of footprint in MIS applications. The scenario that suits the cable link best is where the required ROM is relatively small while the RCM mechanism has to be kept faraway from the incision port.

6. Prototype of cable linkage

A passive concept-proving prototype of the cable linkage is built. The dimensions of the linkage are given in Table 5. The ROM is 69°, which satisfies the requirement of 60° ROM in most of the abdominal MIS applications [16]. The additional 9° are added such that v is 0.3 and L_1 is an integer. r is selected to be 1.22 to minimise rounding of L_2 and L_3. The selection of v and r helps reducing machining error and thus the potential positioning error of the remote centre. Note that due to the limit on the available cable, the minimum required stiffness presented in Fig. 14 is not applied on the cable in Loop FB.

The mechanical constraint of a cable loop can be achieve identically through end-less tendon drive or open-ended tendon drive, as classified in [25]. End-less tendon drive is literally closed-loop cable. It is structurally simpler and can theoretically be fully controlled by less actuators comparing to the open-ended tendon. On the other hand, open-ended tendon drive, which actively controls a pulley with two antagonistic tendons that are connected to their own actuators, respectively, yields zero or small backlash in the expanse of complexity. As the prototype is built for proof of concept, closed-loop cable is implemented in the prototype. To minimise the backlash, timing belt is used and the pre-tension is applied.

The CAD model of the cable linkage, showing two limits and the centre of the ROM, is illustrated in Fig. 22. The centre and lower limit configurations are combined in the figure by photoshop hence are semi-transparent. The sphere at the bottom right corner of the figure indicates the RC. The design of output link is arbitrary and yet to be optimised for specific MIS applications. The output ROM is 105 to 175° from the positive x-direction. The belts and cable sections are not shown.

A side view of the prototype is illustrated in Fig. 23. In the prototype, the widths of Links AC and CE are 16 mm. The radius of pulleys in Loops PL and PU is reduced to 12 mm due to the available pulley size. It can be observed from the figure that the area enclosed by Loops PL and PU is not significantly larger than the sizes of Links AC and CE, despite the outstanding tensioners located in the middle of the links. In addition, the pulleys in Loop FB are mostly enclosed by Links BG and DG in the side view, thus do not cause significant increase in the size of mechanism.

Top views of the prototype are illustrated in Figs. 24 and 25. Fig. 24 annotates the links and Loops PL and PU. In both loops, timing belts are used to minimise backlash. It also eliminates the chance of slip of cable on pulleys in Loops PL and PU, where the consequence of such cable slip is the lost of RCM function. To increase the rigidity of the mechanism, a duplicated pair of Links AC and AF is introduced. Both links are located above Links CE, P6 and P7 in Fig. 24.
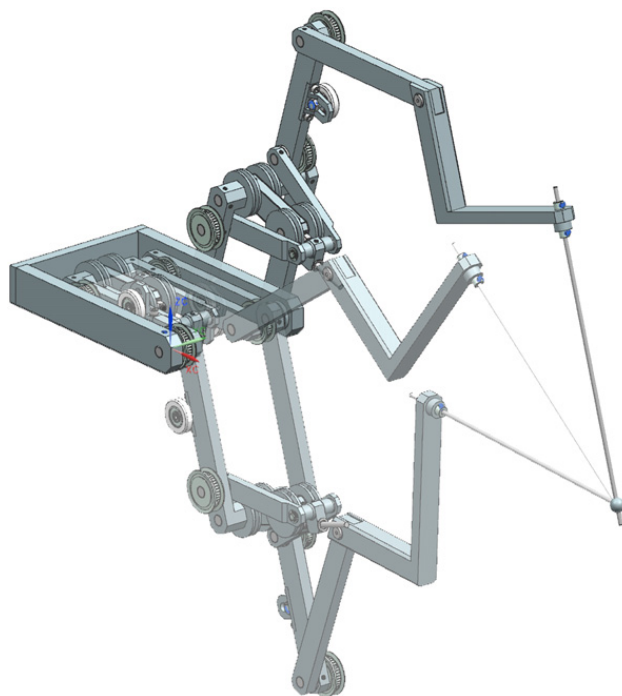
Fig. 22. CAD model of cable linkage.
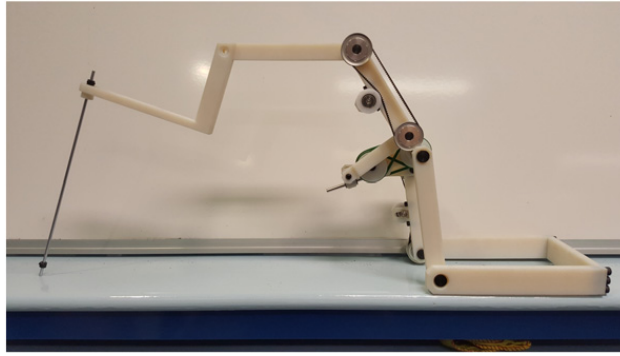
Fig. 23. Right side view of prototype.
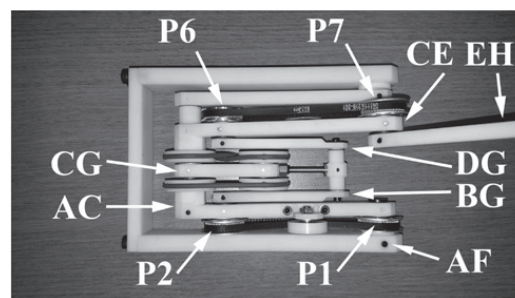
Fig. 24. Top view of prototype 1.
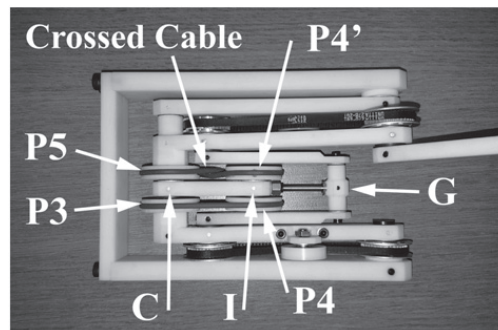
Fig. 25. Top view of prototype 2.

Fig. 25 annotates Loop FB. In this prototype, Loop FB is achieved by using two cable loops, one between P3 and P4 and the other between P4 and P5. Two pulleys, P4 and P4′ are rigidly connected to each other and mounted at Joint I. P4 is connected to P3, and P4′ is connected to P5 with crossed cable. Pulleys P3 and P5 are rigidly connected to Links AC and CE, respectively, by 3D-printing the pulley and the link as one part. To enable the crossed configuration of cable between P4′ and P5, a round belt is used.

The presence of tension in the correct sides of cable loops is vital for verifying the design concept. On the other hand, the exact magnitude of tension is of less importance, as it is primarily used as a prototyping guideline. The sign of cable tension can be readily observed through higher transverse cable stiffness on the driving side of a cable loop than that on the driven side. By manually applying force at the output link and comparing the cable stiffness, it is found that the presence of tension within the full range of motion is consistent with Figs. 5 and 6, as well as the outcomes in Section 3 . Apart from that, the prototype is manipulated to the centre configuration, where loads are applied manually in the attempt to force the prototype into the undesired configuration. Jamming of linkage is observed, thus verifies that the linkage can only turn into the desired configuration.

7. Conclusion

This paper introduces a cable linkage with RCM. The design of the cable linkage is presented, and proof on RCM function is conducted mathematically.

The tension in all cable sections is determined by means of a constraint approach. The analytical solution at the overlapped configuration is derived. The numerical solution at non-overlapped configurations are obtained through QR decomposition. The tensions are positive within the full working range, validating the function of the linkage.

The cable tension calculated is verified through finite element simulation. The constraint approach yields exact solution of cable tension in Loops PL and PU within full ROM, and in Loop FB at overlapped configuration. The error in Loop FB at non-overlapped configurations is small.

The constraint approach is further used to determine the minimum required cable stiffness, corresponding to a given overall system stiffness at the output link. Both the tension and infinitesimal displacement of cable are derived from the constraint approach and solved with QR decomposition.

Quantitative comparison between the footprints of the cable linkage and PB-linkage is conducted in a simplified surgical scenario. The footprint is described in three approaches. In two of the approaches, the cable linkage yields smaller footprint in half of the design points. In the last one the cable linkage achieves 50% to 80% reduction in footprint.

A prototype is constructed for proof of concept. Closed-loop cable is used to simplify the architecture. Timing belts are used in Loops PL and PU to prevent slip of cable on pulley. Loop FB is further divided into two loops, in between P3 and P4, and P4′ and P5, respectively. Round belt is implemented between P4′ and P5 to enable crossed cable configuration. The correct presence of tension within full range of motion, as calculated in Section 3, is validated. The prototype is also proved to be prevented from turning into the undesired configuration.

Appendix A. Supplementary data

Supplementary data to this article can be found online at http://dx.doi.org/10.1016/j.mechmachtheory.2016.07.023.

References

[1] C.-H. Kuo, J.S. Dai, P. Dasgupta, Kinematic design considerations for minimally invasive surgical robots: an overview, Int. J. Med. Rob. Comput. Assisted Surg. 8 (2) (2012) 127–145.
[2] R.H. Taylor, D. Stoianovici, Medical robotics in computer-integrated surgery, IEEE Trans. Robot. Autom. 19 (2003) 765–781.
[3] C.H. Kuo, J.S. Dai, Robotics for minimally invasive surgery: a historical review from the perspective of kinematics, Proc. History of Machines and Mechanisms, Tainan, Taiwan, 2008, pp. 337–354.
[4] G. Zong, X. Pei, Classification and type synthesis of 1-DOF remote center of motion mechanisms, Mech. Mach. Theory 43 (2008) 1585–1595.
[5] C. Chen, M. Pamieta, Novel linkage with remote center of motion, Proc. 3rd IFToMM International Symposium on Robotics and Mechatronics, Vol. 2,Singapore, 2013, pp. 139–147.
[6] M. Ghodoussi, S.E. Butner, Y. Wang, Robotic surgery - the transatlantic case, Proc. IEEE International Conference on Robotics and Automation (ICRA), vol. 2, 2002, pp. 1882–1888.
[7] A. Guerrouad, P. Vidal, SMOS: stereotaxical microtelemanipulator for ocular surgery, Proc. Annual International Conference of the IEEE Engineering in Medicine and Biology Society, Vol. 3,Seattle, USA, 1989, pp. 879–880.
[8] E. Hempel, H. Fischer, L. Gumb, T. Höhn, H. Krause, U. Voges, H. Breitwieser, B. Gutmann, J. Durke, M. Bock, A. Melzer, An MRI-compatible surgical robot for precise radiological interventions, Comput. Aided Surg. 8 (2003) 180–191.
[9] A.J. Madhani, G. Niemeyer, J.K. Salisbury, The black falcon: a teleoperated surgical instrument for minimally invasive surgery, Proc. IEEE/RSJ International Conference on Intelligent Robots and Systems, vol. 2,Victoria, British Columbia, 1998, pp. 936–944.
[10] R.H. Taylor, J. Funda, D.D. Crossman, J.K. Karidis, D.A. LaRose, Remote Center-of-Motion Robot for Surgery, 1995.
[11] S.J. Blumenkranz, D.J. Rosa, Manipulator for Positioning Linkage for Robotics Surgery, 1995.
[12] M. Feng, Y. Fu, B. Pan, C. Liu, Development of a medical robot system for minimally invasive surgery, Int. J. Med. Rob. Comput. Assisted Surg. 8 (2012) 85–96.
[13] K. Kim, H. Song, S. Park, J. Lee, Y. Yoon, Design and evaluation of a teleoperated surgical manipulator with an additional degree of freedom for laparoscopic surgery, Adv. Robot. 24 (2010) 1697–1718.
[14] W.H. Zhu, S.E. Salcudean, S. Bachmann, P. Abolmaesumi, Motion/Force/Image control of a diagnostic ultrasound robot, Proc. IEEE International Conference on Robotics and Automation (ICRA), vol.2, San Francisco, USA, 2000, pp. 1580–1585.
[15] D. Stoianovici, L.L. Whitcomb, D. Mazilu, R.H. Taylor, R.L. Kavoussi, Remote Center of Motion Robotic System and Method, 2004.
[16] M.J.H. Lum, D.C.W. Friedman, G.S.H. King, K. Fodero, R. Leuschke, B. Kannaford, J. Rosen, M.N. Sinanan, The REVAN: design and validation of a telesurgery system, Int. J. Robot. Res. 28 (2009) 1183–1197.
[17] G. Bai, D. Li, S. Wei, Q. Liao, Kinematics and synthesis of a type of mechanisms with multiple remote centers of motion, Proc. IME. C. J. Mech. Eng. Sci. 228 (18) (2014) 3430–3440.
[18] R.R. Solomon, T. Cooper, Multi-ply Strap Driver Trains for Robotic Arms, 2007.
[19] G. Haber, M.A. White, R. Autorino, R.F. Escobar, M.D. Kroh, S. Chalikonda, R. Khanna, S. Forest, B. Yang, F. Altunrenda, R.J. Stein, J.H. Kaouk, Novel robotic da Vinci instruments for laparoendoscopic single-site surgery, Urology 76 (2010) 1279–1282.
[20] H. Long, Y. Yang, X. Jingjing, S. Peng, Type synthesis of 1R1T remote center of motion mechanisms based on pantograph mechanisms, J. Mech. Des. 138 (1) (2016) 014501.
[21] J. Li, Y. Xing, K. Liang, S. Wang, Kinematic design of a novel spatial remote center-of-motion mechanism for minimally invasive surgical robot, J. Med. Devices 9 (1) (2015) 011003.
[22] M. Hadavand, A. Mirbagheri, S. Behzadipour, F. Farahmand, A novel remote center of motion mechanism for the force-reflective master robot of haptic tele-surgery systems, Int. J. Med. Rob. Comput. Assisted Surg. 10 (2) (2014) 129–139.
[23] R.H. Taylor, D. Stoianovici, Is smaller workspace a limitation for robot performance in laparoscopy? J. Urol. 179 (2008) 1138–1143.
[24] D.W. Hong, R.J. Cipra, A method for representing the configuration and analyzing the motion of complex cable-pulley systems, J. Mech. Des. 125 (2) (2003) 332–341.

[25] L.-W. Tsai, Design of tendon-driven manipulators, J. Vib. Acoust. 117 (B) (1995) 80–86.
[26] X. Tang, An overview of the development for cable-driven parallel manipulator, Adv. Mech. Eng. 6 (2014) 823028.
[27] L.-W. Tsai, J.-J. Lee, Kinematic analysis of tendon-driven robotic mechanisms using graph theory, J. Mech. Transm. Autom. Des. 111 (1) (1989) 59–65.
[28] D. Lau, D. Oetomo, S.K. Halgamuge, Generalized modeling of multilink cable-driven manipulators with arbitrary routing using the cable-routing matrix, IEEE Trans. Robot. 29 (5) (2013) 1102–1113.
[29] C. Chen, Power analysis of epicyclic transmissions based on constraints, J. Mech. Robot. 4 (2012)
[30] A.A. Shabana, Computational Dynamics, Wiley, Chichester, UK, 2010.

Chapter 5

Framework of Modelling Concentric Tube Robot

The RCM mechanisms discussed in the previous chapters offer two out of the four DOFs required in the MIS applications. To achieve the translation along and rotation around the incision axis, as well as materialising a robotic wrist to manipulate the surgical end effectors inside the patient's body, the concentric tube robots (CTRs) are investigated. Regardless of whether the CTRs were to be used as standalone surgical robots or to be combined with the RCM robot, kinetostatic models of the CTRs is essential for the applications.

The computational efficiencies of the kinetostatic models of the CTRs play vital roles in the applications of the CTRs, as they affect the performance of the design optimisation and inverse kinematics algorithms. While achieving sufficient modelling precision, less attention was paid to the computational efficiencies in the derivation of existing models. Furthermore, the efficiencies of the modelling approaches could be different under various external loading conditions, which are corresponding to the cannula and non-cannula types of robotic instruments. In fact, to the extend of the author's knowledge, there is no existing research that quantifies the computational efficiencies of the CTR models.

Given the aforementioned research gaps, the specific objectives of the work presented in

this chapter were:

1. To derive computationally efficient kinetostatic models of the CTRs.

2. To identify the effects of all assumptions used in the derivations.

3. To evaluate the computational efficiencies of the models under various loading conditions

The work presented is published in [115], and the full manuscripts is attached below. The major research outcomes are:

1. Four robot dependent mappings were derived, and combined with a robot independent mapping to form the complete kinetostatic models.

2. Seven key assumptions were identified, and their detailed effects on the derivation of models were discussed.

3. The models were tested through mathematical simulations, where three sets of CTRs were subjected to concentrated and distributed external loads, to simulate the applications for non-cannula and cannula instruments, respectively.

4. Approach B demonstrated up to 25% higher computational efficiency for use on non-cannula instruments.

5. Approach A showed relatively high computational efficiency for use on both types of robotic instruments.

All simulations were conducted in Matlab. A list of abbreviation, along with supplementary information on the setup and derivation of CTR models are provided in Section 5.1.

CrossMark

Framework of modelling concentric tube robot and comparison on computational efficiency

Shao T. Liu · Chao Chen

Abstract The continuum concentric tube robots (CCTRs) are infinite degree-of-freedom robots with elastic structure. The CCTRs have no distinct links/ dedicated backbones and joints as the rigid-link robots and conventional continuum robots do. Their simple and flexible structure, along with the capability to be navigated actively, can benefit minimally-invasive surgical applications. However, modelling of the CCTRs is challenging due to the compliance of structure, and a significant number of frames involved. A framework is developed in this work, linking two modelling approaches. Furthermore, two variations of modelling approaches are derived by treating the key equations in different ways. The computational efficiencies of four modelling approaches are compared, in terms of the overall iteration time, number of iterations and the time for single iteration. The effect of iteration accuracy and step size on computational efficiency are investigated as well.

Keywords Concentric tube robot · Kinetostatic modelling · Computational efficiency · Continuum robot · Minimally invasive surgery

S. T. Liu · C. Chen (✉)
Laboratory of Motion Generation and Automation,
Department of Mechanical and Aerospace Engineering,
Monash University, Melbourne, VIC 3800, Australia
e-mail: chao.chen@monash.edu

S. T. Liu
e-mail: shao.liu@monash.edu

1 Introduction

The continuum concentric tube robots (CCTRs) are constantly bending, infinite degree-of-freedom (DOF) robots with elastic structure [26]. They are formed by inserting super-elastic tubes concentrically into each other. Each of the super-elastic tubes, having its own local elasticities and pre-defined curvatures at different cross-sections, interacts with each other as well as the externally applied loads to define the final shape of the robot. The local elasticities and pre-defined curvatures of the super-elastic tubes at each cross-section of a CCTR can be changed by relative rotation and translation of the super-elastic tubes, hence altered the final shape of the CCTR.

The CCTRs have advantages that benefit minimally invasive surgeries (MIS). Firstly, they are capable in steering around body cavities [24]. When combined with the follow-the-leader capability [24], the CCTRs can be used as active cannulae that do not rely on off-axis forces from the surrounding tissue [24] to navigate through body channels, hence increasing the dexterity while reducing potential damages along the paths. Secondly, comparing to the conventional rigid and straight MIS tools, the CCTRs provide turn-corner ability while maintaining the dexterity at the distal ends [29]. Therefore the CCTRs do not have to follow the straight line defined by the incision port and the target, which permits optimum incision path planning to avoid sensitive anatomy features [24] or reduce the numbers of incision ports needed [3].

Thirdly, the mechanical structures of the CCTRs are simple. In addition, the lumen of the CCTRs can house tubes and wires for control of tip-mounted tools [9–11], resulting in compact surgical tools to further reduce the level of invasion. Lastly, when unintended contacts with tissues occur, the CCTRs deform rather than damage the tissues [27], hence are potentially safer than the rigid MIS tools.

Despite having outstanding advantages, the modelling of CCTRs is different and complex as compared to the rigid-link manipulators. The CCTRs rely on equilibrium of force and moment to define their final shapes, including the structural compliance and the externally applied loads.

The modelling of CCTRs is divided into two different mappings [26] since the early works. The robot-dependent (RD) mapping relates the actuator inputs, which are the rotation and translation of the super-elastic tubes, to the shape of the robot. The robot-independent (RI) mapping then relates the shape of the robot to the positions and orientations of nodes on the robot.

The robot-dependent mapping of CCTR is based on the combination of two key equations: the equilibrium of force and moment, and the constitutive law. The equilibrium of force and moment computes the distribution of loads along the CCTR, which is further related to the deformation (hence the shape) of the CCTR through the constitutive law. The ultimate aim is to compute the shape, i.e. local curvatures at cross-sections of the CCTR, such that they can be feed to the robot-independent mapping to determine the nodal positions and orientations.

The early CCTR robot-dependent models [24, 27–29] consider the bending of super-elastic tubes under no external load. The twist of super-elastic tubes are not included [24] or included only in the straight section of the CCTR [27–29]. The bending curvature is determined through the combination of the equilibrium of moment and minimum strain energy approach. Then such twist is modelled over the entire body of the CCTRs [21–23]. The models based on special Cosserat rod theory [2] with equilibrium of force and moment were introduced firstly for the case without external loads [9, 11], which paves the way to consider the external loads. Models considering external loads are finally developed based on the same approach [3, 11, 15, 18, 19, 30, 31], enabling the use of CCTRs in MIS applications. The

precision of CCTR models under global frame concentrated tip loads [15, 18] and distributed loads along body [18] is experimentally verified. Usage of CCTRs in cardiac [4, 8], neurosurgical [1, 6, 25], nasal [5, 7] and urethral procedures [13] have been explored.

The assumptions play vital roles in the derivation of the models. Apart from that, various frames are involved in the modelling while not being explicitly specified, resulting in difficulties in following the derivation procedures, as well as inconvenience in applying CCTR models. Most importantly, the models are based on Cosserat rod theory [17], which yield no closed-form solutions. The models require numerical integration to obtain both the local curvatures (with RD mapping) and positions/orientations (with RI mapping) of tube cross-sections. Furthermore, the known boundary conditions, which are the actuator inputs and the external loads, are separated at two ends of the tubes. Therefore, numerical iteration utilising shooting method is required to solve for the shapes of the CCTRs. As such, final expressions in different forms have great impact on the computational efficiency.

The presence of two key equations in the RD mapping enables two formulation approaches, which have different computational efficiencies. The first one is a straightforward approach where the key equations are used separately. The local forces and moments at cross-sections of CCTR is firstly computed, followed by the local curvatures. In this approach, the final expression is for propagating the concentrated force and moment at the cross-sections of CCTR. The second approach manipulates and combines the two equations, resulting in a united final expression that propagates directly the local curvature.

Furthermore, as external loads are involved, different approaches in modelling the loads also affect the form of final expressions and impact the computational efficiency. In various approaches, the external force applied at the distal end of the CCTR is either integrated into the model directly or modelled as part of the distributed load that is applied along the body of the CCTR. The differences in the usage of key equations and modelling of external loads in combined yield four modelling approaches with their own computational efficiencies, which are discussed and compared in Sects. 3 and 4.

This paper describes framework on the CCTR models based on the Cosserat rod theory. The frames

and hence the evolution of the physical quantities are explicitly specified. The effects of assumptions in the derivation are analysed. The final expressions in four different forms are presented. Two of which are equivalent to the well-known modelling approaches [11, 18] while the other two are newly derived. The computational efficiencies of all modelling approaches are compared through simulations, in terms of the overall iteration time and number of iterations required to reach a solution, as well as the time taken to complete single iteration cycle. Simulations are conducted to investigate the effects of accuracy and step size.

Section 2 briefs the two mappings in the modelling. Section 3 derives the modelling approaches with the final expressions given in four forms and discuss the iteration scheme. Section 4 presents a comparison on the computational efficiencies of the modelling approaches, as well as the effect of accuracy and step size.

2 Robot-independent and robot-dependent mappings

2.1 Robot-independent mapping

It is trivial that continuum robots that have identical shapes, regardless of their mechanical structures, should have identical positions and orientations at all nodes on the robots. Therefore, the mapping from the shape of a continuum robot to the nodal position and orientation is robot-independent (i.e. irrelevant to mechanical structure).

In the RI mapping, a CCTR is described as the collection of coordinate frames that are attached to the different tubes and locations on the CCTR. As an analogy to rigid body motion, a CCTR can be regarded as the trajectories of moving frames, which travel from the proximal end of the CCTR to the distal end [16]. The frames are described using 4×4 transformation matrices. From the moving frame point of view, the frames attached to the cross-sections are instantaneous configurations of the moving frames, and are related to each other through linear and angular velocities. Such velocities are time derivatives in rigid body motion, while being spatial derivatives (with respect to arc length, i.e. distance to the proximal end of CCTR) in RI mapping of continuum robots. The linear velocity

represents the elongation and shear strain, while the angular velocity represents the curvature. The relation between the frames is represented mathematically as [16, 18]

$$
{}^{s+h}_{s}T \frac{d}{ds}\left({}^{s}_{s+h}T\right) = \begin{bmatrix} {}^{s}u_s \times & {}^{s}v_s \\ 0 & 0 \end{bmatrix} \tag{1}
$$

where T is the transformation matrix, the superscripts and subscripts on the left-hand side are the frames transfer to and from, respectively. s and $s + h$ are the current and next tube cross-sections, respectively, where s is the distance from a cross-section to the proximal end of the CCTR, measured along the body of the tubes. h is the distance between the cross-sections. d/ds represents the spatial derivative. u and v are the curvature and strain, respectively. The $\times$ represents the cross-product matrix. The subscripts on the right-hand side indicate the locations of physical quantities. For example, ${}^{s}u_s$ refers to the curvature of cross-section s, and represented in its attached frame F_s.

Since the CCTR models are solved through numerical integration, Eq. (1) is written in the discretised form as [16]

$$
{}^{s}_{s+h}T = \begin{bmatrix} e^{u_n \times h_n} & (I^3 - e^{u_n \times h_n})u_n \times v_n + u_n u_n^T v_n h_n \\ 0 & 1 \end{bmatrix} \tag{2}
$$

where

$$
e^{u_n \times h_n} = I^3 + u_n \times \sin h_n + u_n \times u_n \times (1 - \cos h_n) \tag{3}
$$

where u_n, v_n and h_n are the normalised curvature, strain and step size, respectively, given by

$$
\begin{aligned}
u_n &= \frac{{}^{s}u_s}{||{}^{s}u_s||} \\
v_n &= \frac{{}^{s}v_s}{||{}^{s}u_s||} \\
h_n &= h||{}^{s}u_s||
\end{aligned} \tag{4}
$$

2.2 Frame assignments in robot-dependent mapping

On a CCTR, all the super-elastic tubes share the same bending shape, while twisting differently. The frame

assignment and the curvature reflect such phenomenon. To describe the common bending shape, dedicated Frame F_{0s} is attached to the cross-section s. The z-axis of F_{0s} is perpendicular to cross-section s, i.e. tangent to the local curve. The corresponding bending curvature is $^{0s}u_{0s}$. From the moving frame point of view, F_{0s} can be considered a frame that slides along the body of the CCTR without rotating around its z-axis. As a result of zero twist, the z-component of $^{0s}u_{0s}$ is zero. The twist of individual super-elastic tube is described by frame F_{is} and curvature $^{is}u_{is}$, where i is the tube index starting from 1 (1 is outermost). Due to the common bending shape, all the frames at cross-section s share the same z-axis, while the x- and y-axes are different. The curvatures follow the relation below

$$^{is}u_{is} = {}^{is}_{0s}R\,^{0s}u_{0s} + {}^{is}u_{isz} = R_z^T(\theta_{is})^{0s}u_{0s} + {}^{is}u_{isz} \qquad (5)$$

where R is the 3x3 rotation matrix, $R_z(\theta_{is})$ is the standard z-axis rotation matrix of twist angle θ_{is}. All the curvatures are written as 3x1 matrix form, and $^{is}u_{isz}$ is the torsional curvature whose x- and y-components are zero. The twist angle θ_{is} is measured as the difference between the x-axes of Frames F_{0s} and F_{is}. The torsional curvature, written in local frame F_{is} as $^{is}u_{isz}$, is also the spatial rate of change of the twist angle θ_{is}

$$\frac{d}{ds}\theta_{is} = {}^{is}u_{is|z} \qquad (6)$$

where $^{is}u_{is|z}$ is the z-component of the vector $^{is}u_{isz}$.

Referring to Fig. 1, a two-tube CCTR example is considered. Frames F_{00}, F_{10} and F_{20} (shown as x- and z-axes) are attached to the proximal ends of the CCTR, super-elastic tubes 1 (grey, outer) and 2 (red, inner), respectively. The initial twist angles, θ_{10} and θ_{20} are the actuator input angles of the two super-elastic tubes, respectively. Similarly, Frames F_{0L}, F_{1L} and F_{2L} are

the frames attached to the distal ends, and θ_{1L} and θ_{2L} are the twist angles at the distal ends. Note that the Frames F_{1L} and F_{2L} attached to the non-combined super-elastic tubes are for demonstrating the pre-defined bending shape and the non-twisted conditions of the super-elastic tubes. The ones attached to the super-elastic tubes in the combined CCTR are the interest in the modelling. Note that the actuator input translation d_i for the super-elastic tubes is not shown in Fig. 1 and not considered in the derivation of models, as it only affects the location of the cross-section of super-elastic tube that is corresponding to cross-section s on the CCTR, i.e. it merely changes the local pre-defined curvature and elasticity of the super-elastic tube at cross-section s.

2.3 External loads in robot-dependent mapping

To enable easy integration of loads in the MIS applications, the loads are classified based on the combination of two approaches. The first one is the conventional approach of concentrated and distributed loads. The second one distinguishes the external loads based on the frames they are described in, i.e. the global reference frame F_G or the local frames F_{0s} and F_{is}. The second one is introduced as different loads are better described in different frames. For example, the weights of the super-elastic tubes and the surgical end effector are given in the global frame. On the other hand, the surgical contact loads at the distal end or over the body of the CCTR are measured in the local frames.

Referring to Fig. 1, six types of external loads are considered in the derivation of models. At the proximal and distal ends, there are concentrated forces negative $^{00}n_{00}$ and positive $^{0L}n_{0L}$, respectively, and concentrated moments negative $^{00}m_{00}$ and positive $^{0L}m_{0L}$, respectively. The negative sign comes from the sign convention in the derivation, which states that all the loads at proximal end of a tube section are negative. For easy derivation of models, only local frames concentrated loads are presented. All global frame concentrated loads are transformed into the local frame and considered as part of the overall local frame concentrated load when solving the models. Along the body of the CCTR, there are distributed forces $^{0s}f_{0s}$ and $^G q_{0s}$, and distributed moments $^{0s}\tau_{0s}$ and $^G\lambda_{0s}$. Note that for distributed loads, two symbols are
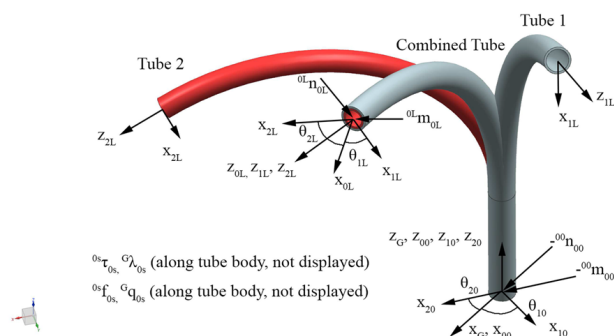

Fig. 1 Concentric tube setup

used for each of the force and moment for better distinguish of frames. All external loads on the CCTR are the sum of loads (of the same type) on the super-elastic tubes. As assumed in existing modelling approaches, all the external loads are assumed to be known. It is also noteworthy that force sensing based on uncertain measurement of the shape of CCTR [20] and the fibre Bragg grating (FBG) sensors [32] has been explored, which provides information on tip force on the CCTR. As such, it partially avoids using the assumption and potentially increases the modelling accuracy.

2.4 Assumptions in robot-dependent mapping

All current CCTR models to date assume no shear or elongation condition. Such assumption simplifies the strain term v. v under assumption is given by

$$^s v_s = \begin{bmatrix} \epsilon_{xx} & \epsilon_{yy} & 1 + \epsilon_{zz} \end{bmatrix}^T = \begin{bmatrix} 0 & 0 & 1 \end{bmatrix}^T \qquad (7)$$

where the ϵ terms are the strains in different axes. Since the strain for all the frames are identical, v is written instead of $^s v_s$ to simplify the notation. Such assumption plays a vital role in the simplification of the expression for propagating the torsional curvature, which is explained in Sect. 3.6.

Another assumption assumes linear elasticity, i.e. linear relation between the tube deformation and the generated moment.

$$^{is} m_{is} = K_{is} (^{is} u_{is} - ^{is} u_{pis}) \qquad (8)$$

where m is the 3×1 concentrated moment, K is the 3×3 elasticity which is a constant within one step of numerical integration, u and u_p are the 3×1 curvatures of tube after and before deformation. u_p is also called the pre-defined curvature of super-elastic tube. Note that the m, u and u_p must be written in the same local frame, as indicated by the superscript. The elasticity K is defined as

$$K_{is} = \begin{bmatrix} E_x I_{xx} & 0 & 0 \\ 0 & E_y I_{yy} & 0 \\ 0 & 0 & G_z I_{zz} \end{bmatrix} \qquad (9)$$

where E and G are the Young's modulus and shear modulus of the super-elastic tube, respectively. I is the second moment of area. This assumption reduces the amount of calculations hence increases the computational efficiency.

The last assumption states that there is no gap in between the super-elastic tubes, while the surfaces of the super-elastic tubes are frictionless. The no-gap assumption avoid the troublesome of finding the contact points between the super-elastic tubes as well as the modelling of the magnitudes and locations of the interaction loads when deriving the expressions for super-elastic tubes. The frictionless assumption simplifies the loading condition of the super-elastic tubes and hence the expression for propagating the expression for propagating the torsional curvature, which is explained in Sect. 3.6. Note that while there exist model in which friction is taken into account [14], it is not used in the succeeding prototyping of CCTR, hence the no-friction assumption is still considered in this paper.

Apart from the aforementioned key assumptions, there are four more assumptions that come from the practical applications. Firstly, the elasticities of the super-elastic tubes are assumed constant, as the entire tubes are often made from one material and same cross-sectional shape. The assumption is expressed mathematically as

$$K_{is} = K_i \qquad (10)$$

Secondly, such elasticities are assumed identical in both x- and y-direction, due to the homogeneous material property of the super-elastic material. Thus

$$E_x = E_y = E \qquad (11)$$

Thirdly, the pre-defined curvatures of the super-elastic tubes are limited to bending, i.e. no pre-defined twist, i.e.

$$^{is} u_{pis} = \begin{bmatrix} ^{is} u_{pis|x} & ^{is} u_{pis|y} & 0 \end{bmatrix}^T \qquad (12)$$

where the subscripts $|x$ and $|y$ indicate the x- and y-components in scalar form, respectively. Lastly, distributed moments in the global reference frame $^G \lambda_{0s}$ is not considered in the modelling, as such type of external load hardly exists in the MIS scenario. As a result, there is no $^G \lambda_{is}$ on individual super-elastic tubes, and the distributed moments on individual super-elastic tubes are in their local frame.

3 Kinetostatic expressions in RD-mapping

In RD-mapping, the combination of equilibrium of force and moment and the constitutive law yields the

key equations to solve for both the common bending curvature $^{0s}u_{0s}$ of the combined CCTR and the torsional curvature $^{is}u_{is}$ of the super-elastic tubes. The modelling approaches are distinguished by the ways in which the key equations for $^{0s}u_{0s}$ are manipulated. Such differences lead to the variations in computational efficiencies. In this section, the derivation of key equations based on the equilibrium of loads and constitutive law is presented firstly, followed by the variation of such key equations in different approaches.

3.1 Equilibrium of force and moment and constitutive law

Equilibrium of force and moment provides information on the concentrated force and moment at each cross-section of a CCTR. The constitutive law relates the shape, i.e. the local curvatures, to the concentrated moment, hence completes the RD-mapping of the CCTRs.

3.1.1 Equilibrium of force and moment

Consider a finite tube section on a CCTR, from arbitrary cross-sections $s = a$ to $s = b$, where the distance in between the cross-sections is h. The equilibrium of force and moment of this tube section is written by summing all the external loads applied by the environment and its adjacent tube sections. Given that the interaction loads between the super-elastic tubes, i.e. the distributed loads, cancel out with each other in the summation, the equilibrium of force and moment contains only the external distributed loads.

Since there is evolution in frames involved, it is essential to distinguish the objective evolution of a physical quantity from the change in the representation of such physical quantity due to the change in frame. To separate the objective evolution from the overall change, which the later contains the change of a physical quantity due to change in frame, the equilibrium of force and moment is written in the global frame F_G. The reason being that the stationary F_G yields zero change in physical quantity due to change in frame, thus the objective evolution is

equivalent to the overall change. In the derivation, the rate of objective evolution and the overall rate of change are represented by d'/ds and d/ds, respectively [12].

The equilibrium of force and moment around the origin of F_G and written in F_G, is given by

$$
\sum_{i=1}^{i=i_{max}} \left(-\,{}^G_{ia}R^{ia}n_{ia} + {}^G_{ib}R^{ib}n_{ib} \right)
$$
$$
+ \int_a^b {}^G_{0s}R^{0s}f_{0s} + {}^G q_{0s}\,ds = 0
\tag{13}
$$

and

$$
\sum_{i=1}^{i=i_{max}} \left(-{}^G P_{GA} \times {}^G_{ia}R^{ia}n_{ia} + {}^G P_{GB} \times {}^G_{ib}R^{ib}n_{ib} \right)
$$
$$
+ \int_a^b {}^G P_{GS} \times ({}^G_{is}R^{0s}f_{0s} + {}^G q_{0s})\,ds
$$
$$
+ \sum_{i=1}^{i=i_{max}} \left(-{}^G_{ia}R^{ia}m_{ia} + {}^G_{ib}R^{ib}m_{ib} \right)
$$
$$
+ \int_a^b {}^G_{0s}R^{0s}\tau_{0s} + {}^G\lambda_{0s}\,ds = 0
\tag{14}
$$

where the P terms are the 3x1 position vectors, representing the positions of the origins of Frames F_{is} measured with respect to F_G. i_{max} is the number of super-elastic tube in the CCTR. Note that all current modelling approaches can suit arbitrary number of super-elastic tubes. However, due to the limits of the diameters of tubes which can be used, typically, only two or three tubes are used in practice. Experimental verifications of current models summarised in the introduction section are conducted with CCTRs containing two or three super-elastic tubes. For clinical applications, three-tube-CCTRs are used in [4, 5, 7]

As the concentrated loads of super-elastic tubes sum to those of the combined CCTR, the concentrated loads in Eqs. (13) and (14) can be written as

$$
{}^{0s}n_{0s} = \sum_{i=1}^{i=i_{max}} {}^{0s}_{is}R^{is}n_{is}
$$
$$
{}^{0s}m_{0s} = \sum_{i=1}^{i=i_{max}} {}^{0s}_{is}R^{is}m_{is}
\tag{15}
$$

Manipulating the $^{0s}n_{0s}$ and $^{0s}m_{0s}$ terms rather than the corresponding terms of individual super-elastic tubes reduces amount of calculations and increases the computational efficiency in the iteration. Thus in the following derivation, $^{0s}n_{0s}$ and $^{0s}m_{0s}$ are used instead of $^{is}n_{is}$ and $^{is}m_{is}$ wherever possible.

Equations (13) and (14) can be combined into a neater and coupled form through 6x6 transformation matrix X [12] as

$$- {}_{0a}^{G}X \begin{bmatrix} {}^{0a}n_{0a} \\ {}^{0a}m_{0a} \end{bmatrix} + {}_{0b}^{G}X \begin{bmatrix} {}^{0b}n_{0b} \\ {}^{0b}m_{0b} \end{bmatrix} + \int_{a}^{b} {}_{0s}^{G}X \begin{bmatrix} {}^{0s}f_{0s} \\ {}^{0s}\tau_{0s} \end{bmatrix} ds$$
$$+ \int_{a}^{b} \begin{bmatrix} {}^{G}q_{0s} \\ {}^{G}P_{GS} \times {}^{G}q_{0s} + {}^{G}\lambda_{0s} \end{bmatrix} ds = 0 \qquad (16)$$

where X is defined as

$$
{}_{is}^{G}X = \begin{bmatrix} {}_{is}^{G}R & 0 \\ {}_{is}^{G}R^{is}P_{GS} \times & {}_{is}^{G}R \end{bmatrix} = \begin{bmatrix} {}_{is}^{G}R & 0 \\ {}^{G}P_{GS} \times {}_{is}^{G}R & {}_{is}^{G}R \end{bmatrix}
$$
$$
{}_{G}^{is}X = \begin{bmatrix} {}_{G}^{is}R & 0 \\ {}_{G}^{is}R^{G}P_{SG} \times & {}_{G}^{is}R \end{bmatrix} = \begin{bmatrix} {}_{G}^{is}R & 0 \\ {}^{is}P_{SG} \times {}_{G}^{is}R & {}_{G}^{is}R \end{bmatrix}
$$
$$\qquad (17)$$

The first two terms in Eq. (16) can be rearranged into one integration. Further, the ground frame external loads in the last integral can be rearranged to have the same format as X

$$\int_{a}^{b} \frac{d}{ds} \left({}_{0s}^{G}X \begin{bmatrix} {}^{0s}n_{0s} \\ {}^{0s}m_{0s} \end{bmatrix} \right) ds + \int_{a}^{b} {}_{0s}^{G}X \begin{bmatrix} {}^{0s}f_{0s} \\ {}^{0s}\tau_{0s} \end{bmatrix} ds$$
$$+ \int_{a}^{b} \begin{bmatrix} 1 & 0 \\ {}^{G}P_{GS} \times & 1 \end{bmatrix} \begin{bmatrix} {}^{G}q_{0s} \\ {}^{G}\lambda_{0s} \end{bmatrix} ds = 0 \qquad (18)$$

The rates of objective evolution of the concentrated force and moment are obtained by taking the derivative of Eq. (18), i.e.

$$\frac{d}{ds} \left({}_{0a}^{G}X \begin{bmatrix} {}^{0a}n_{0a} \\ {}^{0a}m_{0a} \end{bmatrix} \right) + {}_{0a}^{G}X \begin{bmatrix} {}^{0a}f_{0a} \\ {}^{0a}\tau_{0a} \end{bmatrix}$$
$$+ \begin{bmatrix} 1 & 0 \\ {}^{G}P_{GA} \times & 1 \end{bmatrix} \begin{bmatrix} {}^{G}q_{0a} \\ {}^{G}\lambda_{0a} \end{bmatrix} = 0 \qquad (19)$$

Since the derivative is taken in the stationary F_{G}, where the d'/ds terms are equivalent to d/ds, all the d/ds terms in Eq. (19) can be replaced by d'/ds. Premultiplying Eq. (19) with the inverse transformation matrix ${}_{G}^{0a}X$ yields

$$\frac{d'}{ds} \begin{bmatrix} {}^{0a}n_{0a} \\ {}^{0a}m_{0a} \end{bmatrix} = - \begin{bmatrix} {}^{0a}u_{0a} \times & 0 \\ v \times & {}^{0a}u_{0a} \times \end{bmatrix} \begin{bmatrix} {}^{0a}n_{0a} \\ {}^{0a}m_{0a} \end{bmatrix}$$
$$- \begin{bmatrix} {}^{0a}f_{0a} \\ {}^{0a}\tau_{0a} \end{bmatrix} - \begin{bmatrix} {}_{G}^{0a}R & 0 \\ 0 & {}_{G}^{0a}R \end{bmatrix} \begin{bmatrix} {}^{G}q_{0a} \\ {}^{G}\lambda_{0a} \end{bmatrix}$$
$$\qquad (20)$$

Equation (20) is used to propagate for the local frame concentrated force and moment on the cross-sections of CCTR, which are later related to the common bending curvature. Note that it does not provide information on the z-direction loads on the individual super-elastic tube, thus additional equations are required.

3.1.2 The constitutive law

The constitutive law relates the concentrated moment at a cross-section of a CCTR to the deformation, which is represented as the change in curvature. The constitutive law of a single super-elastic tube is written by substituting Eq.(5) into (8)

$$^{is}m_{is} = K_{is} \left({}_{0s}^{is}R^{0s}u_{0s} - {}^{is}u_{pis} + {}^{is}u_{isz} \right) \qquad (21)$$

The constitutive law of the CCTR is obtained by substituting Eq. (21) into (15), which yields

$$^{0s}m_{0s} = \sum_{i=1}^{i_{max}} {}_{is}^{0s}RK_{is} \left({}_{0s}^{is}R^{0s}u_{0s} - {}^{is}u_{pis} + {}^{is}u_{isz} \right) \qquad (22)$$

Equations (20) and (22) are the key expressions for the common bending curvature $^{0s}u_{0s}$. Different approaches in treating these equations are presented in Sects. 3.2 to 3.5. Furthermore, the expressions for propagating torsional curvature $^{is}u_{isz}$ is derived by applying the single-tube version of Eqs. (20) and (22), which is described in Sect. 3.6.

3.2 Approach in Dupont's model [11] (Approach A)

In order to obtain an expression of $^{0s}u_{0s}$ in terms of the concentrated moment $^{0s}m_{0s}$, Dupont [11] rearranged Eq. (22) into the form below:

$$^{0s}u_{0s} = \left(\sum_{i=1}^{i_{max}} {}_{is}^{0s}RK_{is}{}_{0s}^{is}R \right)^{-1}$$
$$\left({}^{0s}m_{0s} - \sum_{i=1}^{i_{max}} {}_{is}^{0s}RK_{is} \left(-{}^{is}u_{pis} + {}^{is}u_{isz} \right) \right) \Big|_{xy}$$
$$\qquad (23)$$

where the subscripts $|xy$ refer to the x and y components. The z-component of $^{0s}u_{0s}$ is by definition zero. By assuming identical Young's modulus in x- and y-directions, the product of $^{0s}_{is}RK_{is}{}^{is}_{0s}R$ is identical to K_{is} (further reduced to K_i based on the assumption of constant elasticity), which reduces the amount of calculations. Note that $^{is}u_{isz}$ is identical to $^{0s}u_{isz}$, as F_{0s} and F_{is} share the same z-axis.

In summary, Approach A utilises Eq. (23) and both components of Eq. (20) to obtain the $^{0s}u_{0s}$ in each step in iterations. Equation (20) explicitly provides the information on both the concentrated force and moment at each cross-section of the CCTR.

3.3 Approach B

To reduce the number of equations for iterations, we can modify Eq. (20) in the following way that the propagation of its concentrated force component is eliminated.

Consider the CCTR described in Fig. 1. Summing the forces on the CCTR from cross-section $s = a$ to the distal end then transform into F_{0a} yields

$$^{0a}n_{0a} = {}^{0a}_{0L}R{}^{0L}n_{0L} + {}^{0a}_{G}R\int_{a}^{L}({}^{G}_{0s}R{}^{0s}f_{0s} + {}^{G}q_{0s})ds \quad (24)$$

where the distributed forces $^{0s}f_{0s}$, $^{G}q_{0s}$ and the distal end concentrated force $^{0L}n_{0L}$ are assumed known according to Sect. 2.3. Substituting Eq. (24) into the moment component of Eq. (20) gives

$$\frac{d'}{ds}{}^{0a}m_{0a} = -{}^{0a}u_{0a} \times {}^{0a}m_{0a} - {}^{0a}\tau_{0a} - {}^{0a}_{G}R{}^{G}\lambda_{0a}$$
$$- v \times \left({}^{0a}_{0L}R{}^{0L}n_{0L} + {}^{0a}_{G}R\int_{a}^{L}({}^{G}_{0s}R{}^{0s}f_{0s} + {}^{G}q_{0s})ds\right) \quad (25)$$

Equation (25) is equivalent to Eq. (20) with reduced number of expressions. However, since the rotation matrices $^{0a}_{0L}R$ and $^{0a}_{0s}R$ are unknown at current step of iteration, further manipulation must be taken or the $^{0L}n_{0L}$ and $^{0s}f_{0s}$ terms must be excluded from the model.

The global frame component of $^{0L}n_{0L}$ (see Sect. 2.3, concentrated tip loads are modelled as overall $^{0L}n_{0L}$ regardless of the frame they are originally described in) can be written as part of the global frame distributed loads through Dirac Delta function [18] as

$$^{G}q_{0s} = \begin{cases} {}^{G}q_{0s} + {}^{G}n_{0L} & L - h \le s < L \\ {}^{G}q_{0s} & 0 \le s < L - h \end{cases} \quad (26)$$

Note that as $^{0s}f_{0s}$ cannot be included in Eq. (25) due to the unknown $^{G}_{0s}R$, the local frame component of the overall $^{0L}n_{0L}$ cannot be included through the same method as demonstrated in Eq. (26). Therefore, the reduction in the number of expressions is achieved at the cost, that the local frame component of the concentrated tip load $^{0L}n_{0L}$ and local frame distributed load $^{0s}f_{0s}$ cannot be included in the model. The simplified version of Eq. (25) is

$$\frac{d'}{ds}{}^{0a}m_{0a} = -{}^{0a}u_{0a} \times {}^{0a}m_{0a} - {}^{0a}\tau_{0a} - {}^{0a}_{G}R{}^{G}\lambda_{0a}$$
$$- v \times {}^{0a}_{G}R\int_{a}^{L}{}^{G}q_{0s}ds \quad (27)$$

In summary, Approach B utilises Eq. (23) and Eq. (27) to obtain the $^{0s}u_{0s}$ in each step in iterations. As such, the number of equations in each step in iterations is reduced to two.

3.4 Approach C

An alternative approach to reduce the number of expressions is to retain the force component of Eq. (20) but manipulate its moment component. Such approach achieves the reduction in the number of expressions while providing the concentrated force at each cross-section of CCTR. In addition, it does not have the limitation on including local frame forces, as described previously in Sect. 3.3.

Substituting Eq. (22) into the moment component of Eq. (20) and simplifying (utilising the assumptions, as described in Sect. 3.2) yields

$$\frac{d'}{ds}{}^{0a}u_{0a} = -\left(\sum_{i=1}^{i_{max}}K_i\right)^{-1}$$
$$\times \left(\sum_{i=1}^{i_{max}}{}^{0a}_{ia}R({}^{ia}u_{ia} \times K_i)({}^{ia}_{0a}R{}^{0a}u_{0a} - {}^{ia}u_{pia} + {}^{ia}u_{iaz})\right.$$
$$+ \sum_{i=1}^{i_{max}}(-K_i{}^{0a}u_{iaz} \times {}^{0a}u_{0a} - {}^{0a}_{ia}RK_i\frac{d'}{ds}{}^{ia}u_{pia}$$
$$+ {}^{0a}_{ia}RK_i\frac{d'}{ds}{}^{ia}u_{iaz}) + v \times {}^{0a}n_{0a}$$
$$\left.+ {}^{0a}\tau_{0a} + {}^{0a}_{G}R{}^{G}\lambda_{0a}\right)\bigg|_{xy} \quad (28)$$

Note that Eq. (28) contains the derivative of $^{is}u_{pia}$. Therefore the equation requires the pre-defined curvature to be continuous. The consequence being that the combined CCTR needs to be divided into sections in which the pre-defined curvatures of all super-elastic tubes are continuous, and Eq. (28) can only be applied within those sections. Additional measures, explained in Sect. 3.7, must be taken to recover and match the boundary conditions at the boundaries of each section.

In summary, Approach C utilises Eq. (28) and the force component of Eq. (20) to obtain the $^{0s}u_{0s}$ in each step in iterations. The advantages of Approach C are 1) the number of expressions in each step in iteration is reduced to two; and 2) it explicitly provides the information on concentrated force at each cross-section of CCTR.

3.5 Approach in Rucker's Model [18] (Approach D)

The number of expressions for $^{0s}u_{0s}$ can be further reduced to one, by simultaneously eliminating the force component of Eq. (20) and manipulating its moment component. Substituting Eq. (22) into Eq. (27) and simplifying (utilising the assumptions, as described in Sect. 3.2) gives

$$
\begin{aligned}
\frac{d'}{ds}{}^{0a}u_{0a} = {} & -\Big(\sum_{i=1}^{i_{max}} K_i\Big)^{-1} \\
& \times \Big(\sum_{i=1}^{i_{max}} {}^{0a}_{ia}R\big({}^{ia}u_{ia} \times K_i\big)\big({}^{ia}_{0a}R{}^{0a}u_{0a} - {}^{ia}u_{pia} + {}^{ia}u_{iaz}\big) \\
& + \sum_{i=1}^{i_{max}} \big(-K_i{}^{0a}u_{iaz} \times {}^{0a}u_{0a} - {}^{0a}_{ia}RK_i\frac{d'}{ds}{}^{ia}u_{pia} \\
& + {}^{0a}_{ia}RK_i\frac{d'}{ds}{}^{ia}u_{iaz}\big) + v \times \big({}^{0a}_{0L}R{}^{0L}n_{0L} \\
& + \int_a^L {}^{0a}_{0s}R{}^{0s}f_{0s} + {}^{0a}_G R^G q_{0s}\big) + {}^{0a}\tau_{0a} + {}^{0a}_G R^G\lambda_{0a}\Big)\Big|_{xy}
\end{aligned}
$$
(29)

Equation (29) is the only equation used to obtain the $^{0s}u_{0s}$ in each step in iteration. Since it is based on Eq. (27), it also has limitation on applying local frame forces.

3.6 Torsional curvature

The torsional curvature $^{is}u_{isz}$ is derived though a similar approach to that of the common bending curvature $^{0s}u_{0s}$. The difference being that the Eqs. (13) and (14) are written for single super-elastic tube, and that the loads on individual super-elastic tube are unknown while cannot be cancelled out in the expressions. Following the process from Eqs. (13) and (14) to (20), the rate of objective evolution of concentrated moment $^{is}m_{is}$ is derived as

$$
\frac{d'}{ds}{}^{is}m_{is} = -v \times {}^{is}n_{is} - {}^{is}u_{is} \times {}^{is}m_{is} - {}^{is}\tau_{is} - {}^{is}_G R^G\lambda_{is}
$$
(30)

While the $^{is}m_{is}$ term in Eq. (30) can be eliminated by applying Eq. (21), the $^{is}n_{is}$, $^{is}\tau_{is}$ and $^G\lambda_{is}$ are unknown. However, since only the z-component of Eq. (30) is the focus, the presence of in z-component $^{is}n_{is}$, $^{is}\tau_{is}$ and $^G\lambda_{is}$ can be eliminated, such that a solvable expression for z-component can be obtained without considering the x- and y-components. Such elimination is the results of assumptions, which is explained below.

The z-component of Eq. (30) is given by

$$
\begin{aligned}
\frac{d'}{ds}{}^{is}m_{is}\big|_z = {} & -E_{ixy}I_{ixy}\big(-{}^{is}u_{is|x}{}^{is}u_{pis|y} + {}^{is}u_{is|y}{}^{is}u_{pis|x}\big) \\
& - {}^{is}\tau_{is|z} - \big({}^{is}_G R^G\lambda_{is}\big)\big|_z
\end{aligned}
$$
(31)

where E_{ixy} and I_{ixy} are the elasticity and second moment of area in x and y directions, which are assumed equal.

In Eq. (31), the $^{is}n_{is}$ term vanishes, as the x- and y-components of v are both assumed zero. In addition, $^G\lambda_{is}$ is zero by assumption. Furthermore, the $^{is}\tau_{is|z}$ is zero, since the only source of z-axis local frame distributed moment is the friction corresponding to the rotation of super-elastic tubes, which again is zero by assumption. Thus, Eq. (31) contains merely the elasticity, the bending curvature and the pre-defined curvature, which are all known. Without such assumptions, additional expressions need to be introduced to fully describe the concentrated and distributed loads over each of the super-elastic tubes, which greatly increases the consumption of computational power.

Although Eq.(31) can be used to propagate for the torsional moment at each cross-section of the

combined CCTR and in turn solve for the torsional curvature, which is similar to the combining Eq. (23) with Eq. (20) or (27) for $^{0s}u_{0s}$, such approach is not used as it require more computational power than propagating the torsional curvature itself. Instead, the approach used by Eq. (28) or (29) is applied. The expression for propagating the torsional curvature is derived simply by substituting the z-component of Eq. (21) into (31), which gives

$$\frac{d'}{ds}\,{}^{is}u_{is|z} = -\frac{E_{ixy}I_{ixy}}{G_{iz}I_{izz}}\left(-{}^{is}u_{is|x}\,{}^{is}u_{pis|y} + {}^{is}u_{is|y}\,{}^{is}u_{pis|x}\right)$$
$$-\frac{1}{G_{iz}I_{izz}}\frac{d'}{ds}(G_{iz}I_{izz})\,{}^{is}u_{is|z} \qquad (32)$$

where the derivative of $G_{iz}I_{izz}$ is zero due to the constant elasticity assumption.

3.7 Iteration scheme

The known boundary conditions on a combined CCTR include actuator input rotation θ_{i0} and translation d_i for each of the super-elastic tubes at the proximal end, and the concentrated loads (both in global and local frames) at the distal end. The input loads at the proximal end and the twist angles at distal end are unknown. Thus it is a boundary value problem (BVP) with split boundary conditions. One approach to solve for such BVP is the shooting method, which is used in [15, 18]. Following shooting method, initial guesses are made to fix up all the boundary conditions at one end to initialised the iteration, such that the BVP is converted to an initial value problem (IVP). The presence of ${}_{G}^{0a}R$ in Eqs. (20) and (27) requires the iteration to start from the proximal end of the CCTR.

The common initial guesses for all the approaches include the concentrated bending moment of the combined CCTR ${}^{00}m_{00|xy}$, the torsional moment of individual super-elastic tube ${}^{i0}m_{i0|z}$. In the cases where Eq. (20) or (29) is involved, the concentrated force ${}^{00}n_{00}$ must be guessed as well. Unlike the moment, the z-component of concentrated force is the one on the combined CCTR, instead of the one on each super-elastic tube.

The boundary conditions at the distal end of the CCTR are used to verify and make correction on the initial guesses, which is expressed as

$$\begin{aligned}
{}^{0L}n_{0L} &= {}^{0L}n_{0Litr}\\
{}^{0L}m_{0L|xy} &= {}^{0L}m_{0Litr|xy}\\
{}^{0L}m_{0L|z} &= (K_{i_{max}}{}^{i_{max}L}u_{i_{max}Lz})|_z\\
0 &= (K_i{}^{iL}u_{iLz})|_z \quad (i < i_{max})
\end{aligned} \qquad (33)$$

where L represents the distal end and itr indicates the results obtained from the iteration. The concentrated loads at the distal end, regardless of the frames they are originally described in, are converted into the local frame F_{0L} to form the overall ${}^{0L}n_{0L}$ and ${}^{0L}m_{0L}$ terms in Eqs. (33), such that they can be compared to the iterated results. The transformation matrix ${}_{G}^{0L}T$ used in the conversion is the one obtained iteratively using current initial guesses. The last two equations in Eqs. (33) state that the external torsional moment is applied only at the distal end of the innermost super-elastic tube. While this is true in most of the applications of the CCTR, where the innermost tube extrudes further than the rest of the super-elastic tubes, such condition is used as an assumption in the cases where the distal ends of multiple super-elastic tubes are flush. Such assumption is the result of having insufficient information to determine the torsional moment applied on each super-elastic tube.

The use of Eq. (28) and (29) (Approaches C and D) requires the combined CCTR to be divided into sections within which the pre-defined curvatures of all super-elastic tubes are continuous. These two equations require an initial ${}^{0s}u_{0s}$ to start with, at the beginning cross-sections of each of the sections with continuous pre-defined curvatures. The initial bending curvature is obtained by applying Eq. (23). Such approach in turn requires Eq. (22) to be used at the distal end of each section with continuous pre-defined curvature, in order to recover ${}^{0s}m_{0s}$ at the boundary.

Although the derivative of K, which comes from taking the derivative of Eq. (22) or (21), is eliminated from Eqs. (28), (29) and (32) (after simplification) by the assumption of constant elasticity, an implicit condition it applies is that the elasticities of all super-elastic tubes must be continuous. Such condition cannot be satisfied at the distal end of a super-elastic tube, where the elasticity becomes zero. Therefore, in Approaches C and D, the combined CCTR needs to be divided at the cross-sections where one of the super-elastic tubes ends. The method used is similar to that used to treat non-continuous pre-defined curvature.

4 Comparison of computational efficiency

Simulations are conducted in Matlab to compare the computational efficiencies of the four modelling approa-ches. Three sets of CCTRs are tested. All the CCTRs contain two super-elastic tubes, whose dimensions are similar to those reported in [15, 18] and [3], respectively. Each super-elastic tube has one straight section at the proximal end, followed by a pre-curved section. The dimensions of the super-elastic tubes are summarised in Tables 1, 2 and 3, respectively. The pre-defined curvatures are assumed constant within the pre-curved sections of the super-elastic tubes. The Young's modulus and shear modulus are 65 GPa and 23 GPa, respectively. The weight of the super-elastic tubes are neglected due to the small tube dimensions. All the pre-defined curvatures are in the x-direction in the local frames of the super-elastic tubes, i.e. the y- and z-components of $^{is}u_{pis}$ are zero. The "direction of curvature" in the tables indicate the initial directions (zero actuator input rotation) of the pre-defined curvature in the global frame.

Six sets of simulations are conducted, where the actuator input rotation and translation, as well as the loading conditions of the combined CCTRs are changed, to obtain a comprehensive measurement of the computational efficiencies of the modelling

Table 1 Super-elastic tube dimensions of CCTR A [15]

	Tube 1	Tube 2
Outer diameter (mm)	2.77	2.41
Inner diameter (mm)	2.55	1.97
Length straight section (mm)	0	18
Length curved section (mm)	150	150
Radius of pre-curvature (mm)	233	248
Direction of curvature	+x	+x

Table 2 Super-elastic tube dimensions of CCTR B [18]

	Tube 1	Tube 2
Outer diameter (mm)	2.37	1.75
Inner diameter (mm)	2.00	1.25
Length straight section (mm)	30.7	122.7
Length curved section (mm)	102.5	206.9
Radius of pre-curvature (mm)	125	200
Direction of curvature	−x	−x

Table 3 Super-elastic tube dimensions of CCTR C [3]

	Tube 1	Tube 2
Outer diameter (mm)	2.29	1.60
Inner diameter (mm)	2.00	1.20
Length straight section (mm)	40	100
Length curved section (mm)	80	100
Radius of pre-curvature (mm)	236	293
Direction of curvature	−x	−x

approaches. The simulations can be divided into two categories, where the CCTRs are subjected different external loads. Simulations 1 to 3, and Simulations 4 to 6, apply concentrated and distributed forces on the CCTRs, respectively. Each CCTR is used in one simulation from each of the categories, respectively. The two simulations conducted with the same CCTR share the same actuator inputs, while having their own loading categories. The exception is CCTR B, where its actuator input translation is removed in the simulation with distributed force. The actuator input rotation in this simulation is retained and the same as that in the simulation with concentrated force.

In all the simulations, the tubes are positioned in such a way that their local z-axes at the proximal ends are coincident with the z-axis of F_G. The outer super-elastic tubes (Tube 1) on all CCTRs are assumed to be fixed, i.e. no actuator input rotation and translation. Due to the limit associated with Eq. (27), local frame concentrated and distributed forces are not considered. The step size h is 1 mm. The iteration accuracy is ±1e-5 (N or Nm) in the magnitudes of all x, y and z components of concentrated tip force and moment. The integration scheme is Runge-Kutta 4.

Since the iterative results at the distal end has the same trend as the initial guesses at the proximal end, i.e. excess / insufficient actuator inputs (comparing to the true solution) yield excess / insufficient outputs (comparing to boundary conditions), the correction on the initial guesses is defined as follows:

$$IG_{j+1} = IG_j - 0.5(P_{itr} - P) \tag{34}$$

where IG are the initial guesses, j and $j+1$ are the current and next iteration cycles, respectively. P_{itr} and P are the iterative results and known boundary conditions at the distal end, respectively. The correction approach is anticipated to yield slower correction and more iteration cycles than the systematic

approaches, thus can assist reducing the error on the time taken for single iteration cycle. On the other hand, comparing to a fixed increment / decrement in the initial guesses, the correction approach ensures that the true solution is not missed and avoids overly-lengthened overall iteration time.

Simulations 1 and 4 are conducted with CCTR A, whose tube dimensions are listed in Table 1. The proximal end of the combined CCTR is the proximal end of Tube 1. Tube 2 is positioned 18 mm behind the proximal end of Tube 1, such that the distal ends of both super-elastic tubes are flush. Thus the effective length of the combined CCTR is 150 mm. The variables in the simulations are summarised in Table 4. The actuator input of Tube 2 is limited to rotation (θ_{20}) only, no translation (d_2) is applied. In Simulation 1, concentrated force ${}^G n_{0L}$ is applied at the distal end of the CCTR in positive y direction of F_G. The direction ${}^G n_{0L}$ is constant while the magnitude is varied. In Simulation 4, distributed force ${}^G q_{0s}$ is applied over the body of the CCTR along positive x direction of F_G. The direction of ${}^G q_{0s}$ is constant while its magnitude is changed. All other external loads, which are not used as the variable in the simulations, are assumed zero.

Simulation 2 and 5 are conducted with CCTR B, whose tube dimensions are listed in Table 2. The proximal end of Tube 1 is 30.7 mm behind the proximal end of the combined CCTR, hence only the pre-curved section of Tube 1 is involved in the effective length of the CCTR. The proximal end of Tube 2 is initially 223.7 mm behind the proximal end of the CCTR. The variables in this simulation are summarised in Table 5. In both simulations, Tube 2 can rotate (θ_{20}). The translation of Tube 2 (d_2) is varied in Simulation 2 and fixed to 101 mm in Simulation 5. In Simulation 2, concentrated force ${}^G n_{0L}$

is applied at the distal end of the CCTR, whose x, y and z-components are identical. The direction ${}^G n_{0L}$ is fixed while the magnitude is varied. In Simulation 5, distributed force ${}^G q_{0s}$ is applied over the body of the CCTR along positive x direction of F_G. The direction of ${}^G q_{0s}$ is constant. All other external loads, which are not used as the variable in the simulations, are assumed zero.

Simulations 4 and 6 are conducted with CCTR C, whose tube dimensions are listed in Table 3. The effective length of the combined CCTR starts from the proximal end of Tube 1. The proximal end of Tube 2 is initially 80 mm behind the proximal end of Tube 1. The variables in this simulation are summarised in Table 6. Tube 2 can rotate (θ_{20}) and translate (d_2). In Simulation 2, concentrated force ${}^G n_{0L}$ is applied at the distal end of the CCTR, whose x, y and z-components are identical. The direction ${}^G n_{0L}$ is fixed while the magnitude is varied. In Simulation 5, distributed force ${}^G q_{0s}$ is applied over the body of the CCTR along positive x direction of F_G. The direction of ${}^G q_{0s}$ is constant while its magnitude is changed. All other

Table 5 Variables in Simulations 2 and 5—CCTR B

Parameters	Magnitude
θ_{20} range (degree)	0–315
θ_{20} interval (degree)	45
d_2 range (mm)	0–92
d_2 interval (mm)	23
${}^G n_{0L}$ range (N)	0 to 2
${}^G n_{0L}$ interval (N)	0.2
${}^G q_{0s}$ range (N/m)	0–2.9
${}^G q_{0s}$ interval (N/m)	0.48

Table 6 Variables in Simulations 3 and 6—CCTR C

Parameters	Magnitude
θ_{20} range (degree)	0–315
θ_{20} interval (degree)	45
d_2 range (mm)	0–80
d_2 interval (mm)	40
${}^G n_{0L}$ range (N)	0–1
${}^G n_{0L}$ interval (N)	0.2
${}^G q_{0s}$ range (N/m)	0–3
${}^G q_{0s}$ interval (N/m)	0.5

Table 4 Variables in Simulations 1 and 4—CCTR A

Parameters	Magnitude
θ_{20} range (degree)	0–315
θ_{20} interval (degree)	45
${}^G n_{0L}$ range (N)	0–2
${}^G n_{0L}$ interval (N)	0.2
${}^G q_{0s}$ range (N/m)	0–4
${}^G q_{0s}$ interval (N/m)	0.67

external loads, which are not used as the variable in the simulations, are assumed zero.

For each simulation, the average time and number of iterations taken to solve for a CCTR under one set of given conditions are recorded. The average time to compete one iteration cycle is calculated as an indication of numbers of arithmetic operations in each approach. The overall simulation time for two categories of simulations are illustrated in Figs. 2 and 3, respectively. The full results are presented in Tables 7, 8, 9, 10, 11 and 12, respectively.

In the tables, "time" is the average time taken to complete iteration of a CCTR under one set of given actuator inputs and external loads. "iter. num" indicates the corresponding number of iteration cycles taken. "single time" represents the time taken to complete one iteration cycle, which is calculated from the overall time and number of iteration. The percentage differences use the results of Approach A as the references.

When the CCTRs are subject to concentrated forces (Simulations 1 to 3), the approaches based on Eq. (27) (Approaches B and D), require less iterations comparing to the approaches based on Eq. (20) (Approaches A and C). The percentage difference ranges from -26 % to -20 %, except for Approach B in Simulation 2, which achieves only 15.6 % reduction. On the other hand, once the selection between Eqs. (20) and (27) has been made, the comparisons between B and D, and between A and C, respectively,
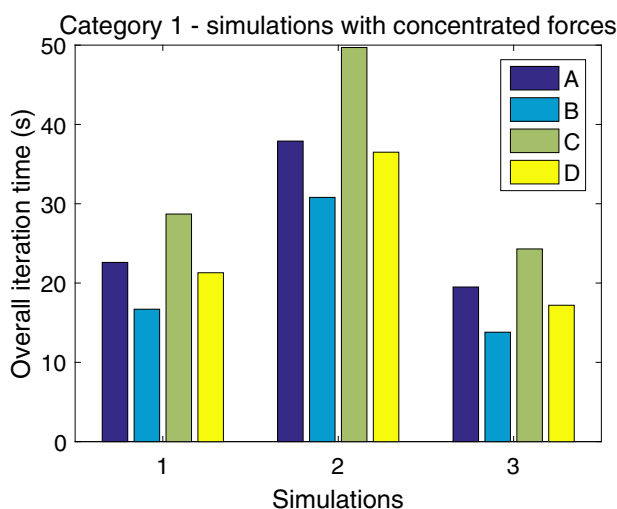
show that the difference between propagating bending curvature and propagating concentrated loads is minimal. In addition there is no clear indication on the approaches that yield higher efficiency.

When the CCTRs are subject to distributed forces (Simulations 4 to 6), Eqs. (27) and (20) have opposite effects to those in Simulations 1 to 3. In Simulations 4 and 6, the use of Eq. (27) (Approaches B and D) requires about 40 % more iterations, comparing to Eq. (20) (Approaches A and C). In Simulation 5, the difference is even larger. The effects of propagating concentrated loads and propagating bending curvature are not clear in the Approaches B and D, where Eq. (27) is used both approaches. However, propagating concentrated loads (Approach A) does show advantage over propagating bending curvature (Approach C), where Eq. (20) is used both approaches.

The trend of single iteration time is consistent in all simulations. Approaches A and B, and Approaches C and D, have similar amount of arithmetic operations,
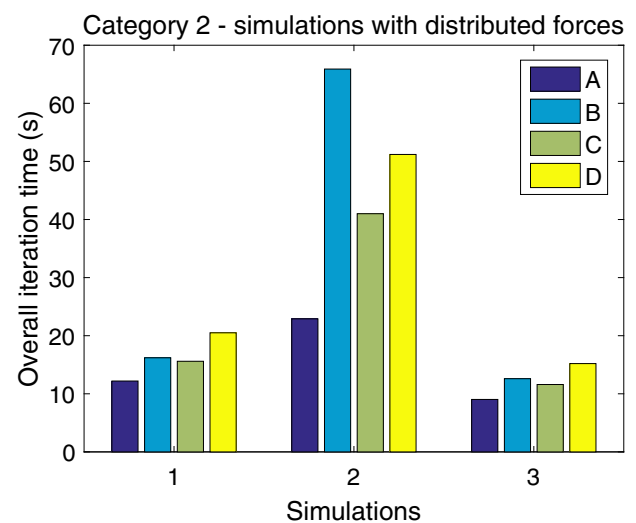
Fig. 3 Overall iteration time for simulations with distributed forces

Table 7 Results of Simulation 1—CCTR A

Approaches	A	B	C	D
Time (s)	22.6	16.7	28.7	21.3
Time diff (%)	n/a	−26.1	26.7	−5.85
Iter. num	21.1	16.3	21.1	16.3
Iter. num diff (%)	n/a	−22.8	−0.16	−22.7
Single time (s)	1.07	1.03	1.36	1.31
Single time diff (%)	n/a	−4.20	26.9	21.9

Fig. 2 Overall iteration time for simulations with concentrated forces

Table 8 Results of Simulation 2—CCTR B

Approaches	A	B	C	D
Time (s)	37.9	30.8	49.7	36.5
Time diff (%)	n/a	−18.7	31.0	−3.59
Iter. num	29.0	24.5	30.2	23.3
Iter. num diff (%)	n/a	−15.6	4.22	−19.8
Single time (s)	1.31	1.26	1.64	1.57
Single time diff (%)	n/a	−3.71	25.7	20.2

Table 9 Results of Simulation 3—CCTR C

Approaches	A	B	C	D
Time (s)	19.5	13.8	24.3	17.2
Time diff (%)	n/a	−29.2	24.8	−12.1
Iter. num	18.3	13.7	18.2	13.5
Iter. num diff (%)	n/a	−25.1	-0.15	−25.9
Single time (s)	1.07	1.00	1.33	1.26
Single time diff (%)	n/a	−5.56	25.0	18.5

Table 10 Results Simulation 4—CCTR A

Approaches	A	B	C	D
Time (s)	12.2	16.2	15.6	20.5
Time diff (%)	n/a	33.0	28.4	68.5
Iter. num	11.6	16.1	11.9	16.2
Iter. num diff (%)	n/a	38.2	2.15	40
Single time (s)	1.04	1.00	1.31	1.27
Single time diff (%)	n/a	−3.73	25.7	21.2

Table 11 Results Simulation 5—CCTR B

Approaches	A	B	C	D
Time (s)	22.9	65.9	41.0	51.2
Time diff (%)	n/a	188	78.9	123
Iter. num	20	60.9	28.9	37.7
Iter. num diff (%)	n/a	204	44.2	87.9
Single time (s)	1.14	1.08	1.42	1.36
Single time diff (%)	n/a	−5.22	24.1	18.9

respectively. The single iteration time of A and B is about 20 % to 25 % shorter than that of C and D. Thus propagating concentrated loads save computational

Table 12 Results Simulation 6—CCTR C

Approaches	A	B	C	D
Time (s)	9.03	12.6	11.6	15.2
Time diff (%)	n/a	39.4	28.2	68.6
Iter. num	9.33	13.4	9.52	12.9
Iter. num diff (%)	n/a	43.3	1.97	38.7
Single time (s)	0.97	0.94	1.22	1.18
Single time diff (%)	n/a	-2.70	25.7	21.6

power over propagating bending curvatures. The comparison between A and B, and between C and D, respectively reveals that the use of Eq. (27) yields about 5 % reduction in amount of arithmetic operations over Eq. (20), when the same physical quantities are propagated.

In Simulations 1 to 3, Approach B has the highest computational efficiency due to the combination of fastest single iteration time and less number of iteration. Approaches D and A, benefiting from smaller number of iterations and less arithmetic operations, have similar computational efficiencies. Approach C is the slowest as the performance is low in both number of iterations and single iteration time.

On the other hand, in Simulations 4 to 6, Approach A is the fastest as it requires the least number of iterations when subjected to distributed forces. Approach C also benefit from the reduced number of iterations. The overall iteration time of Approach B is compromised by the increased number of iterations taken, especially in Simulation 5. Approach D yields low efficiency in general due to disadvantages in both number of iterations and single iteration time.

Preliminary simulations are also conducted to investigate the effects of accuracy and step size on the modelling approaches. Simulation 1 is repeated with various accuracies and step sizes. The parameters are listed in Table 13. In Simulation 7, the accuracy is varied with a constant step size of 1 mm. In Simulation 8, the step size is varied (halved or doubled) with a constant accuracy of $1e^{-5}$. To reduce the overall time taken, the interval of the magnitude of concentrated force is increased to 0.4 N.

The results of Simulations 7 and 8 are presented in Figs. 4, 5, 6, 7, 8 and 9. In Figs. 4 and 6, the x-axes are the logarithm ($\log_{10}$) of accuracy. In Figs. 7 and 9, the x-axes are the logarithm ($\log_2$) of step size.

Table 13 Variables in Simulations 7 and 8—CCTR A

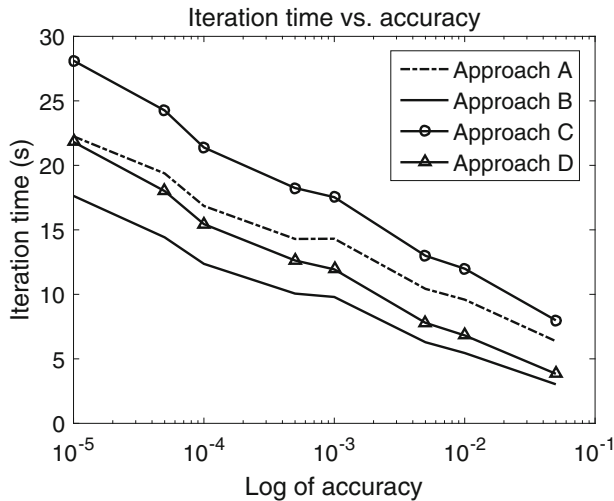| Parameters	Magnitude
Accuracy	$1e^{-5}, 5e^{-5}, 1e^{-4}, \ldots, 5e^{-2}$
Step size (mm)	$2^0, 2^1, \ldots, 2^5$

Fig. 4 Overall time versus accuracy
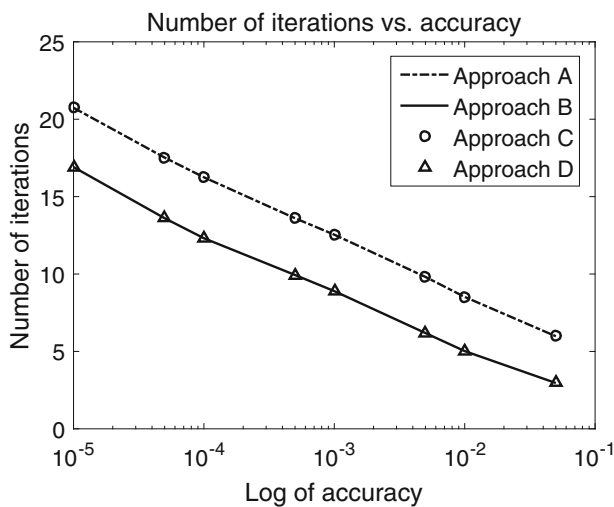
Fig. 5 Iteration number versus accuracy

Figure 5 shows that the number of iterations are inversely proportional to the order ot accuracy. Since the step size is not changed, the time taken to complete one iteration cycle roughly stays constant, as illustrated in Fig. 6. Therefore, the overall iteration time shown in Fig. 4 is roughly linear.

Figure 7 indicates that the time decreases with increasing step size. The rate of such decreasing also

Fig. 6 Single iteration time versus accuracy

Fig. 7 Overall time versus step size

Fig. 8 Iteration number versus step size

Fig. 9 Single iteration time versus accuracy

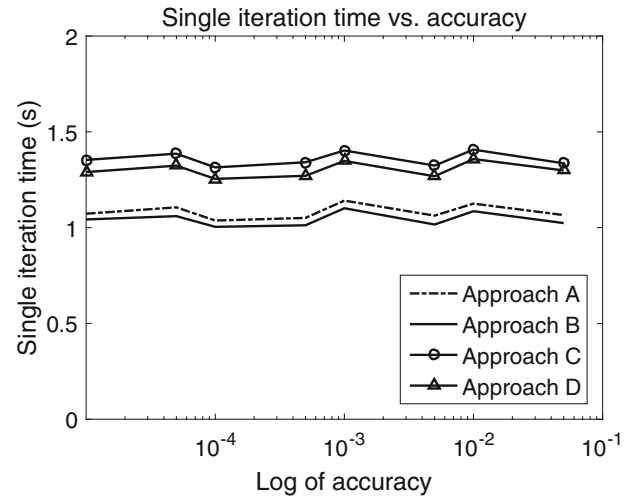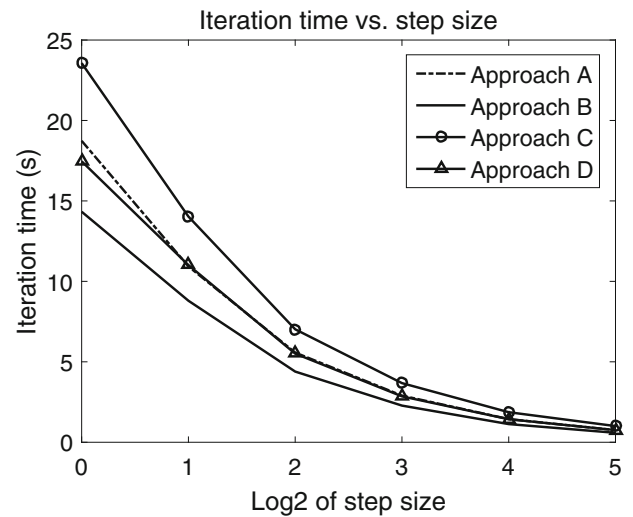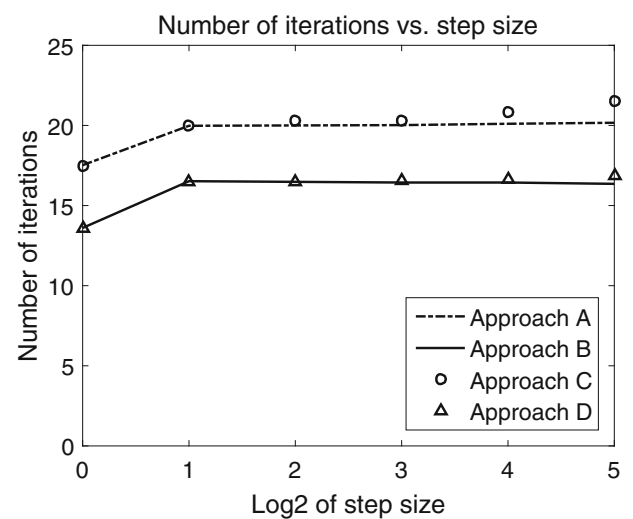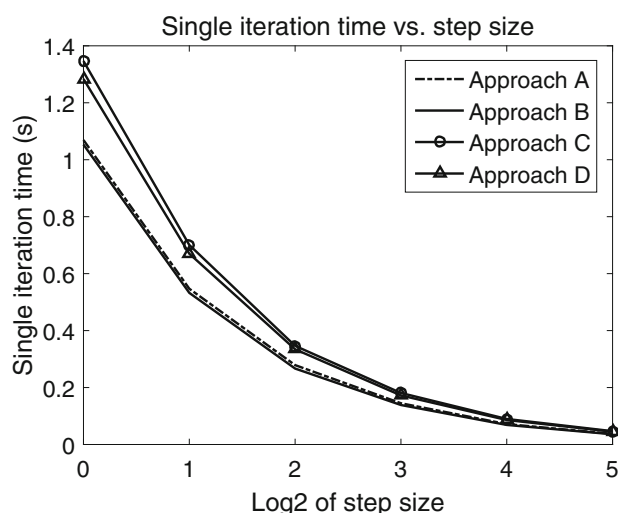decreases as the step size increases. On the other hand, Fig. 8 reveals that the number of iterations is constant, except for when step size is 1 mm. The time taken to complete one iteration cycle and its rate of change decreases with increasing step size. Apart from that, the difference between Approaches A and B and Approaches C and D also decreases with increasing step size.

5 Conclusion

This work studies framework on the kinetostatic modelling of CCTR and the computational efficiencies associated with different modelling approaches. Two existing approaches are considered and two additional modelling approaches are derived. The computational efficiencies of all four approaches are compared through simulations on three CCTRs under varies combination of actuator inputs and loading conditions.

The dominating factor that affects the number of iteration is the form in which the equilibrium of concentrated loads is represented in. The uses of Eqs. (20) and (27) have opposite impacts in two categories of loads. Equations (27) and (20) require less iterations under concentrated and distributed loads, respectively.

The difference between propagating concentrated loads and propagating bending curvature mainly lies on the amount of arithmetic operations. Propagating concentrated loads leads to less arithmetic operations

than propagating bending curvature in both categories of simulations.

The existing approach, Approach A, shows capability in the integration of local frame loads, while being relatively fast under all loading conditions. Thus it is considered suitable for most MIS applications. The newly derived Approach B is found to offer higher computational efficiency in the cases where global frame concentrated forces are the dominating external loads. However such performance cannot be achieved in the applications where distributed forces are the major external loads. Approach D has similar computational efficiency comparing to Approach A when concentrated forces are applied, while being slow in the cases with distributed forces. Approach C is the least efficient approach in the cases where concentrated forces are applied, but offers intermediate efficiency in the cases with distributed forces.

Simulations are conducted to investigate the effect of accuracy and step size. All modelling approaches show inverse linear relations between the accuracy and the time and number of iterations required. The step size does not have significant impact on the number of iterations. Increasing step size leads to decrease in overall and single iteration time, as well as their rates of change with respect to the step size.

Compliance with ethical standards

Conflicts of interest The authors declare that they have no conflict of interest.

References

1. Anor T, Madsen JR, Dupont P (2011) Algorithms for design of continuum robots using the concentric tubes approach: a neurosurgical example. In: 2011 IEEE international conference on robotics and automation (ICRA), pp 667–673. IEEE
2. Antman SS (2005) Nonlinear problems of elasticity. Springer Science+Business Media, New York, USA
3. Bai S, Xing C (2012) Shape modeling of a concentric-tube continuum robot. In: 2012 IEEE international conference on robotics and biomimetics (ROBIO), pp 116–121. IEEE
4. Bedell C, Lock J, Gosline A, Dupont PE (2011) Design optimization of concentric tube robots based on task and anatomical constraints. In: 2011 IEEE international conference on robotics and automation (ICRA), pp 398–403. IEEE

5. Burgner J, Rucker DC, Gilbert HB, Swaney PJ, Russell PT, Weaver KD, Webster RJ (2014) A telerobotic system for transnasal surgery. IEEE/ASME Trans Mechatron 19(3):996–1006

6. Burgner J, Swaney PJ, Lathrop RA, Weaver KD, Webster RJ (2013) Robot-assisted intracerebral hemorrhage evacuation: an experimental evaluation. In: SPIE medical imaging, pp 86,710H–86,710H. International Society for Optics and Photonics

7. Burgner J, Swaney PJ, Rucker DC, Gilbert HB, Nill ST, Russell III, PT, Weaver, KD, Webster III RJ (2011) A bimanual teleoperated system for endonasal skull base surgery. In: 2011 IEEE/RSJ international conference on intelligent robots and systems (IROS), pp 2517–2523. IEEE

8. Butler EJ, Folk C, Cohen A, Vasilyev NV, Chen R, del Nido PJ, Dupont PE (2011) Metal MEMS tools for beating-heart tissue approximation. In: 2011 IEEE international conference on robotics and automation (ICRA), pp 411–416. IEEE

9. Dupont PE, Lock J, Butler E (2009) Torsional kinematic model for concentric tube robots. In: IEEE international conference on robotics and automation, 2009. ICRA'09, pp 3851–3858. IEEE

10. Dupont PE, Lock J, Itkowitz B (2010) Real-time position control of concentric tube robots. In: 2010 IEEE international conference on robotics and automation (ICRA), pp 562–568. IEEE

11. Dupont PE, Lock J, Itkowitz B, Butler E (2010) Design and control of concentric-tube robots. IEEE Trans Robot 26(2):209–225

12. Featherstone R (1987) Robot dynamics algorithms. Springer Science+Business Media, New York, USA

13. Hendrick RJ, Herrell SD, Webster RJ (2014) A multi-arm hand-held robotic system for transurethral laser prostate surgery. In: 2014 IEEE international conference on robotics and automation (ICRA), pp 2850–2855. IEEE

14. Lock J, Dupont PE (2011) Friction modeling in concentric tube robots. In: 2011 IEEE international conference on robotics and automation (ICRA), pp 1139–1146. IEEE

15. Lock J, Laing G, Mahvash M, Dupont PE (2010) Quasistatic modeling of concentric tube robots with external loads. In: 2010 IEEE/RSJ international conference on intelligent robots and systems (IROS), pp 2325–2332. IEEE

16. Pai DK (2002) Strands: interactive simulation of thin solids using cosserat models. In: Computer graphics forum, vol 21, pp 347–352. Wiley Online Library

17. Rubin MB (2013) Cosserat theories: shells, rods and points, vol 79. Springer Science & Business Media, New York

18. Rucker DC, Jones B, Webster RJ III et al (2010) A geometrically exact model for externally loaded concentric-tube continuum robots. IEEE Trans Robot 26(5):769–780

19. Rucker DC, Jones B, Webster III RJ, et al (2010) A model for concentric tube continuum robots under applied wrenches. In: 2010 IEEE international conference on robotics and automation (ICRA), pp 1047–1052. IEEE

20. Rucker DC, Webster RJ (2011) Deflection-based force sensing for continuum robots: a probabilistic approach. In: 2011 IEEE/RSJ international conference on intelligent robots and systems, pp 3764–3769. IEEE

21. Rucker DC, Webster III RJ (2008) Mechanics-based modeling of bending and torsion in active cannulas. In: 2nd IEEE RAS & EMBS international conference on biomedical robotics and biomechatronics, 2008. BioRob 2008, pp 704–709. IEEE

22. Rucker DC, Webster RJ III (2009) Parsimonious evaluation of concentric-tube continuum robot equilibrium conformation. IEEE Trans Biomed Eng 56(9):2308–2311

23. Rucker DC, Webster RJ III, Chirikjian GS, Cowan NJ (2010) Equilibrium conformations of concentric-tube continuum robots. Int J Robot Res 29(10):1263–1280

24. Sears P, Dupont P (2006) A steerable needle technology using curved concentric tubes. In: 2006 IEEE/RSJ international conference on intelligent robots and systems, pp 2850–2856. IEEE

25. Swaney PJ, Burgner J, Lathrop R, Gilbert HB, Weaver KD, Webster RJ, et al (2013) Minimally-invasive intracerebral hemorrhage removal using an active cannula. In: 2013 IEEE international conference on robotics and automation (ICRA), pp 219–224. IEEE

26. Webster RJ, Jones BA (2010) Design and kinematic modeling of constant curvature continuum robots: a review. Int J Robot Res. doi:10.1177/0278364910368147

27. Webster III RJ, Okamura AM, Cowan NJ (2006) Toward active cannulas: miniature snake-like surgical robots. In: 2006 IEEE/RSJ international conference on intelligent robots and systems, pp 2857–2863. IEEE

28. Webster III RJ, Romano JM, Cowan NJ (2008) Kinematics and calibration of active cannulas. In: IEEE international conference on robotics and automation, 2008. ICRA 2008, pp 3888–3895. IEEE

29. Webster RJ III, Romano JM, Cowan NJ (2009) Mechanics of precurved-tube continuum robots. IEEE Trans Robot 25(1):67–78

30. Xu R, Asadian A, Naidu AS, Patel RV (2013) Position control of concentric-tube continuum robots using a modified Jacobian-based approach. In: 2013 IEEE international conference on robotics and automation (ICRA), pp 5813–5818. IEEE

31. Xu R, Patel RV (2012) A fast torsionally compliant kinematic model of concentric-tube robots. In: Engineering in Medicine and Biology Society (EMBC), 2012 annual international conference of the IEEE, pp 904–907. IEEE

32. Xu R, Yurkewich A, Patel RV (2016) Curvature, torsion, and force sensing in continuum robots using helically wrapped FBG sensors. IEEE Robot Autom Lett 1(2):1052–1059

5.1 Supplementary Information on the CTR

5.1.1 Abbreviations in the CTR Paper

Table 5.1: List of Abbreviation in the Paper

E	Young's modulus of material
F	Frame
f	Force (distributed, local frame)
G	Shear modulus of material
h	Step size in numerical integration
L	Length of CTR
I	Second moment of area of the cross-section
K	Elasticity/stiffness
m	Moment (concentrated)
n	Force (concentrated)
P	Position
q	Force (distributed, global frame)
R	Standard 3×3 transformation matrix
T	Standard 4×4 transformation matrix
u	Angular strain, curvature
v	Linear strain
X	6×6 transformation matrix

Table 5.2: List of Abbreviation in the Paper (Continued)

ϵ	Strain
θ	Twist angle
λ	Moment (distributed, global frame)
τ	Moment (distributed, local frame)

Table 5.3: List of Subscripts/Superscripts in the Paper

a	Cross-section a of CTR (used in derivation)
A	Origins of frames attached to cross-section a
b	Cross-section b of CTR (used in derivation)
B	Origins of frames attached to cross-section b
G	Global frame (superscript), origin of global frame (subscript)
0	Local frame attached to cross-section of combined CTR
i	Local frame attached to cross-section of ith individual tube
n	Normalised
p	Pre-defined
s	Cross-section s of CTR
S	Origins of frames attached to cross-section s
itr	Iteration

5.1.2 Supplementary Graphical Illustrations for CTR Model

Figure 5.1 is the graphical illustration of frame assignment of the CTR model, which is described in Section 2.2 of the manuscript. Frames at three CTR cross-sections are shown: the proximal end $s = 0$, an arbitrary middle cross-section s and the distal end $s = L$. The sample CTR consists of two super-elastic tubes. The physical quantities
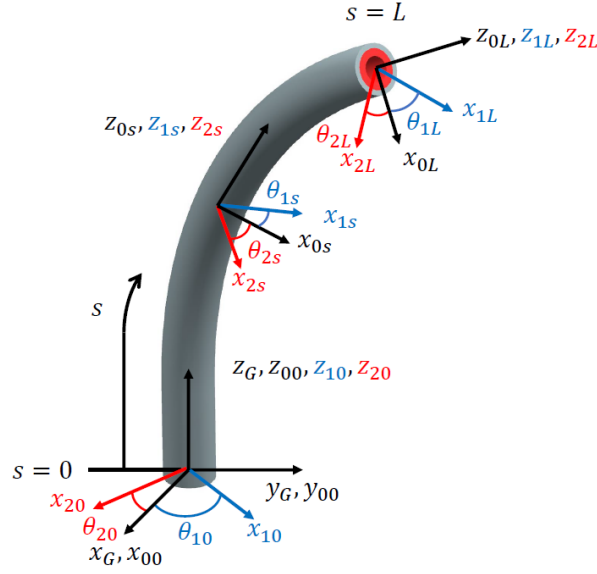
Figure 5.1: Frame Assignment of CTR.

for combined tube, tube 1, and tube 2 are labelled black, blue and red, respectively. It can be observed that the z-axes of frames at the same cross-section are coincident. The x-axes of the super-elastic tubes are angularly displaced by θ, from the x_0 axis.
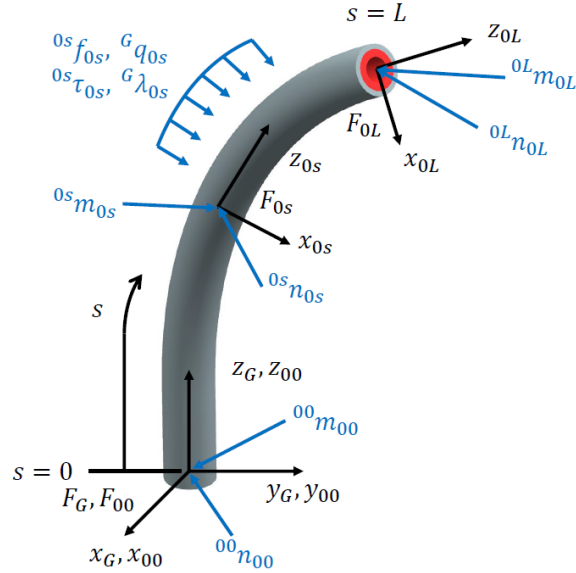
Figure 5.2: External loads on CTR.

Figure 5.2 shows the six types of external loads on a sample CTR. Although the physical effects of the external loads on the CTR (e.g. the shape) do not change with respect to the frame in which they are described, artificially classify the loads based on the frames

can benefit the applications. In the applications, the weights of tubes and the additional equipment mounted on the CTR are readily available in the global reference frame F_G. On the other hand, if sensors were to be mounted on the body and at the tip of a CTR to sense the contact loads, the sensor readings are apparently in the local frames that are attached to the cross-sections of the CTR. Since the models inherently account for the external loads measured in various frames, these weights and sensor readings can be fed directly and intuitively into the CTR models.

Despite the aforementioned convenience in the application, artificially dividing the external loads can potentially cause problems in some modelling approaches, as detailed in Sections 3.3 and 3.5 of the paper. The $^{G}_{0s}R$ rotation matrix presented in Eqs. (24) and (25) correspond to the cross-sections beyond current integration step (further away from the proximal). As such, the associated local frame distributed force $^{0s}f_{0s}$ cannot be readily substituted into the equations.

5.1.3   Supplementary Information on Derivation of CTR Model

In the robot-independent mapping (Section 2.1 of the manuscript), the following statement is made "it is trivial that $\cdots$ regardless of their mechanical structures $\cdots$ identical positions and orientation". The term "mechanical structures" refers to the mechanical structures of the continuum robots, e.g. the CTRs with continuous bodies and no dedicated actuation mechanism along the bodies, and the cable driven robots who have discretised backbones and separated actuation tendons.

Section 2.1 of the manuscript states that the angular velocity is the time derivative of angular position in rigid body motion. Note that the statement is "concept-wise" and is not referring to the formulation. The correct angular velocity is defined by $\vec{\omega}\times = \Omega = \dot{Q}Q^T$ where Q is the rotation matrix.

Equations (2) and (3) are the discretised form of the robot-independent mapping, which is utilised in the numerical integration. The local curvatures u and twist angles θ solved by

the robot-dependent models are fed to these two equations, such that the completed cross-sectional positions and orientations of the entire CTR can be computed. In this paper, since the major focus is the robot-dependent mapping, this standard robot-independent mapping is adopted for all four approaches.
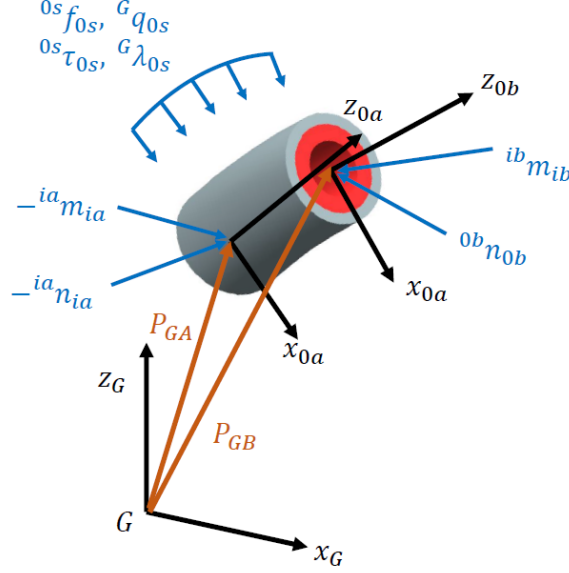
Figure 5.3: Equilibrium of Loads on a finite CTR Section.

Equations (13) and (14) in the paper are essentially equilibrium of force and moment, respectively, on a finite section of the CTR (as shown in Fig. 5.3). In Eq. (13), the first line sums all the external forces applied at the cross-sections a and b. Rotation matrices R are used to map the local frame loads into the global reference frame. The second line of the equation integrates the distributed forces on the finite tube section. Again, a rotation matrix R is used to map the local frame force f into the global frame.

The first line of Eq. (14) sums the moments generated by the concentrated forces around the origin of the global frame, G. The P terms are the lever arms. The second line deals with the moments generated by the distributed forces. The third line sums the concentrated moments, and the last line integrates the distributed moments. Similar to that in Eq. (13), rotation matrices R are included to convert the local frame terms into the global reference frame.

Chapter 6

Conclusions and Future Work

6.1 Conclusions

In this research, two robots have been investigated for use in minimally invasive surgeries: the dual-triangular remote centre of motion (RCM) mechanism and the continuum concentric tube robot (CTR). The objective of this research was to enhance the performance and capability of the two surgical robots, when used individually or combined as one united surgical robot, to reduce the level of invasion and promote further development of robotic minimally invasive surgeries.

A novel cable constrained dual-triangular RCM mechanism was proposed to minimise the footprint and position the mechanism distant from the remote centre, hence reducing the chance of collision between cooperating robotic surgical arms. The reduced footprint enables the development of single-site or trans-natural-orifices MIS, where the robotic arms need to be positioned very close to each other and manipulated within confined workspace.

The reduction in the footprint was achieved through three approaches. Firstly, the area enclosed by the outer boundary of the RCM mechanism was reduced, by the conversion from the parallelogram to the four-bar linkage with small vertex angle. Secondly, the

ROM was doubled from that of the original DT mechanism without expansion in the dimensions of the mechanism by the removal of singularities, and thereby reduced the device footprint while achieving the same output range of motion (ROM). Thirdly, the cable loops were introduced to eliminate the bulky parallelograms in the linkage-based designs. Therefore, the additional space taken by the links between the input joint and the RC was reduced.

To achieve the doubling of the ROM without expansion in the device footprint, the singularities of the linkages were fully investigated. Geometrical constraint equations were derived, leading to the linkage-based and cable-based auxiliary mechanisms to fully constrain the mechanism. To materialise the cable-based design, constraint analysis was used to prove presence of tension in the cable loops. The outcomes showed tension in all cable loops within the full ROM of the mechanism. Such predicted cable tension was further validated through FE analysis and a passive prototype.

The reduction in the footprint was quantified through mathematical simulations in simplified surgical scenarios, where the footprints were described through four approaches. The results showed up to 35%-80% improvement over the footprint of the schematic parallelogram-based design, with the same distance from the input joint to the RC and the same output ROM. In addition, the effectiveness of the cable-based design over the linkage-based version was proven by observing much slimmer "members" (links with associated cable loops) and significantly enlarged clearance/distance between the base joint and the RC in the prototype.

The framework of kinetostatic modelling of the CTRs was explored to increase the computational efficiency. It is anticipated that the improved kinetostatic models will lead to design optimisation and real-time control with lower computational cost, or enabling existing controller hardware to solve for more precise but computationally expansive models. The outcomes will yield broadened application of the CTRs, to serve as non-cannula and cannula robotic instruments with enhanced dexterity and reduced level of invasion.

Four robot dependent mapping approaches were derived based on the Newtonian strat-

egy, and combined with a standard robot independent mapping to form the full kinematic models. The approaches were derived based on the combination of differential equations (written in different forms) and the constitutive law. The improvement in computational efficiency was made by reducing the number of expressions used to compute the local bending curvature in each step of numerical integration, where the four approaches have three, two, two and one expression(s), respectively. In addition, the effects of each assumption on the derivation of equations were identified and evaluated, to pave the way for potential improvement in modelling precision in the future work.

The computational efficiencies of the modelling approaches were compared, in order to investigate the effects of variations in the key equations based on the number of expressions and arithmetic operations, as well as to identify suitable MIS applications for the models. Two out of the four approaches were highlighted. One approach (Approach B [115]), where the differential equations for force and moment are united while the constitutive law is used separately with the differential equations, showed up to 25% improvement under concentrated external loads. However, its performance was not as good under distributed loads. As such, it is suitable for cases where the CTRs replace conventional non-cannula robotic manipulators and concentrated surgical loads at the tips dominate. The other approach (Approach A [115] or [118]), where the force and moment are described in distinct differential equations and the constitutive law is used separately, had relatively high and balanced performance under both loading cases. Hence this approach is a universal one that is suitable for use on CTR-based robotic manipulators of both non-cannula and cannula types.

6.2 Future Work

Beyond the scope of this thesis, further work is needed to maximise the advantages of the proposed RCM mechanism and the kinetostatic model of the CTRs in the MIS applications. The future work can be categorised into three branches, which are regarding the further improvement on the capability and dexterity of the two individual robots and

their optimal combination, respectively.

Although the functioning of the cable system was proven for the RCM mechanism, the analysis was conducted under the assumptions of mass-less mechanical components, zero cable pre-tension and quasi-static conditions. A dynamics model of the cable-constrained RCM mechanism should be derived before investigating the MIS applications, such that the use of assumptions is avoided. For prototyping, even-slimmer designs could be proposed to further reduce the dimensions of the mechanisms that achieve the required mathematical constraints. Further, the open-loop cable configuration may be worth investigating for the optimal cable tension and system stiffness. Apart from those, the application of the RCM mechanisms in specific robotic MIS, such as laparoscopic and urological procedures, should be explored.

Additional fundamental studies should be conducted on the CTRs prior to the applications. To fully utilise the improved kinetostatic model, it should be implemented in the inverse kinematics, design optimisation and control algorithms. In addition, improving the precision of the kinetostatic model itself could be another focus, where gaps and frictions between individual elastic tubes will be integrated into the model. Elastic materials other than the super-elastic Nitinol, as well as the modifications of the tubes (e.g. surface patterns and non-circular cross-sectional shapes) could be explored to increase the achievable curvatures and the stability of the CTRs. Apart from those, the CTR models can be considered as Lie group formulation of the Cosserat kinematics. As such, it is worthy to study the current state of art formulation approach and seek for implementation in the CTR models, for improving computational efficiencies or precision.

Another usage of the kinetostatic model, which will potentially lead to great advances in the MIS applications of CTRs, is the intrinsic shape and load sensing, which will enable the CTR to detect external loads applied at an arbitrary location on the body of the robot without modification (and the expansion in size) on the parts inserted into the patient's body. Such a sensing algorithm is crucial to ensure the safe deployment of CTRs in delicate, complex and confined body anatomies. The kinetostatic model of the CTRs couples the shape and external load information, and thereby is inherently suitable

to serve as the foundation of the intrinsic sensing algorithm.

The combination of the RCM mechanism and the CTR will primarily involve inverse kinematics model and prototyping. The objective of the inverse kinematic model is to minimise the footprint of the RCM mechanism, while ensuring safe and precise control of shape and tip position/orientation of the CTR. An optimisation function will be developed as the core of the model, which determines the optimal manoeuvres of individual components. For prototyping, a slim and light-weight CTR design will be needed, such that it does not compromise the function of the RCM mechanism and increase the overall device footprint.

Bibliography

[1] A. Alikhani, S. Behzadipour, A. Alasty, and S. A. S. Vanini. Design of a large-scale cable-driven robot with translational motion. *Robotics and Computer-Integrated Manufacturing*, 27(2):357–366, 2011.

[2] R. Alterovitz, S. Patil, and A. Derbakova. Rapidly-exploring roadmaps: Weighing exploration vs. refinement in optimal motion planning. In *Robotics and Automation (ICRA), 2011 IEEE International Conference on*, pages 3706–3712. IEEE, 2011.

[3] W. T. Ang, P. K. Khosla, and C. N. Riviere. An intelligent hand-held microsurgical instrument for improved accuracy. In *Engineering in Medicine and Biology Society, 2001. Proceedings of the 23rd Annual International Conference of the IEEE*, volume 4, pages 3450–3453. IEEE, 2001.

[4] T. Anor, J. R. Madsen, and P. Dupont. Algorithms for design of continuum robots using the concentric tubes approach: A neurosurgical example. In *Robotics and Automation (ICRA), 2011 IEEE International Conference on*, pages 667–673. IEEE, 2011.

[5] S. S. Antman. Problems in nonlinear elasticity. *Nonlinear Problems of Elasticity*, pages 513–584, 2005.

[6] R. Autorino, R. J. Stein, E. Lima, R. Damiano, R. Khanna, G.-P. Haber, M. A. White, and J. H. Kaouk. Current status and future perspectives in laparoendoscopic single-site and natural orifice transluminal endoscopic urological surgery. *International journal of urology*, 17(5):410–431, 2010.

[7] H. Azimian, P. Francis, T. Looi, and J. Drake. Structurally-redesigned concentric-tube manipulators with improved stability. In *Intelligent Robots and Systems (IROS 2014), 2014 IEEE/RSJ International Conference on*, pages 2030–2035. IEEE, 2014.

[8] G. Bai, D. Li, S. Wei, and Q. Liao. Kinematics and synthesis of a type of mechanisms with multiple remote centers of motion. *Proceedings of the Institution of Mechanical Engineers, Part C: Journal of Mechanical Engineering Science*, 228(18):3430–3440, 2014.

[9] G. Bai, P. Qi, K. Althoefer, D. Li, X. Kong, and J. S. Dai. Kinematic analysis of a mechanism with dual remote centre of motion and its potential application. In *ASME 2015 International Design Engineering Technical Conferences and Computers and Information in Engineering Conference*, pages V05BT08A011–V05BT08A011. American Society of Mechanical Engineers, 2015.

[10] S. Bai and C. Xing. Shape modeling of a concentric-tube continuum robot. In *Robotics and Biomimetics (ROBIO), 2012 IEEE International Conference on*, pages 116–121. IEEE, 2012.

[11] A. Bajo and N. Simaan. Finding lost wrenches: Using continuum robots for contact detection and estimation of contact location. In *Robotics and Automation (ICRA), 2010 IEEE International Conference on*, pages 3666–3673. IEEE, 2010.

[12] R. Baumann, W. Maeder, D. Glauser, and R. Clavel. The pantoscope: A spherical remote-center-of-motion parallel manipulator for force reflection. In *Robotics and Automation, 1997. Proceedings., 1997 IEEE International Conference on*, volume 1, pages 718–723. IEEE, 1997.

[13] C. Bedell, J. Lock, A. Gosline, and P. E. Dupont. Design optimization of concentric tube robots based on task and anatomical constraints. In *Robotics and Automation (ICRA), 2011 IEEE International Conference on*, pages 398–403. IEEE, 2011.

[14] C. Bergeles and P. E. Dupont. Planning stable paths for concentric tube robots. In *Intelligent Robots and Systems (IROS), 2013 IEEE/RSJ International Conference*

on, pages 3077–3082. IEEE, 2013.

[15] C. Bergeles, A. H. Gosline, N. V. Vasilyev, P. J. Codd, J. Pedro, and P. E. Dupont. Concentric tube robot design and optimization based on task and anatomical constraints. *IEEE Transactions on Robotics*, 31(1):67–84, 2015.

[16] P. Berkelman, E. Boidard, P. Cinquin, and J. Troccaz. Ler: The light endoscope robot. In *Intelligent Robots and Systems, 2003.(IROS 2003). Proceedings. 2003 IEEE/RSJ International Conference on*, volume 3, pages 2835–2840. IEEE, 2003.

[17] P. Berkelman and S. Okamoto. Compact modular system design for teleoperated laparoendoscopic single site surgery. In *Biomedical Robotics and Biomechatronics (BioRob), 2012 4th IEEE RAS & EMBS International Conference on*, pages 905–906. IEEE, 2012.

[18] H. Bian, Y. Liu, Z. Liang, and T. Zhao. A novel 2-rrr/uprr robot mechanism for ankle rehabilitation and its kinematics. *Robot*, 32(1):6–12, 2010.

[19] E. M. Boctor, R. J. Webster III, H. Mathieu, A. M. Okamura, and G. Fichtinger. Virtual remote center of motion control for needle placement robots. *Computer Aided Surgery*, 9(5):175–183, 2004.

[20] P. H. Borgstrom, N. P. Borgstrom, M. J. Stealey, B. Jordan, G. S. Sukhatme, M. A. Batalin, and W. J. Kaiser. Design and implementation of nims3d, a 3-d cabled robot for actuated sensing applications. *IEEE Transactions on Robotics*, 25(2):325–339, 2009.

[21] A. E. Bryson. *Applied optimal control: optimization, estimation and control*. CRC Press, 1975.

[22] G. Buess, A. Arezzo, M. Schurr, F. Ulmer, H. Fisher, L. Gumb, T. Testa, and C. Nobman. A new remote-controlled endoscope positioning system for endoscopic solo surgery. *Surgical Endoscopy*, 14(4):395–399, 2000.

[23] E. C. Burdette, D. C. Rucker, P. Prakash, C. J. Diederich, J. M. Croom, C. Clarke,

P. Stolka, T. Juang, E. M. Boctor, and R. J. Webster III. The acusitt ultrasonic ablator: the first steerable needle with an integrated interventional tool. In *SPIE Medical Imaging*, pages 76290V–76290V. International Society for Optics and Photonics, 2010.

[24] J. Burgner, D. C. Rucker, H. B. Gilbert, P. J. Swaney, P. T. Russell, K. D. Weaver, and R. J. Webster. A telerobotic system for transnasal surgery. *IEEE/ASME Transactions on Mechatronics*, 19(3):996–1006, 2014.

[25] J. Burgner, P. J. Swaney, T. L. Bruns, M. S. Clark, D. C. Rucker, E. C. Burdette, and R. J. Webster. An autoclavable steerable cannula manual deployment device: Design and accuracy analysis. *Journal of medical devices*, 6(4):041007, 2012.

[26] J. Burgner, P. J. Swaney, R. A. Lathrop, K. D. Weaver, and R. J. Webster. Debulking from within: a robotic steerable cannula for intracerebral hemorrhage evacuation. *IEEE Transactions on Biomedical Engineering*, 60(9):2567–2575, 2013.

[27] J. Burgner, P. J. Swaney, D. C. Rucker, H. B. Gilbert, S. T. Nill, P. T. Russell, K. D. Weaver, and R. J. Webster. A bimanual teleoperated system for endonasal skull base surgery. In *Intelligent Robots and Systems (IROS), 2011 IEEE/RSJ International Conference on*, pages 2517–2523. IEEE, 2011.

[28] E. J. Butler, C. Folk, A. Cohen, N. V. Vasilyev, R. Chen, J. Pedro, and P. E. Dupont. Metal mems tools for beating-heart tissue approximation. In *Robotics and Automation (ICRA), 2011 IEEE International Conference on*, pages 411–416. IEEE, 2011.

[29] D. B. Camarillo, C. F. Milne, C. R. Carlson, M. R. Zinn, and J. K. Salisbury. Mechanics modeling of tendon-driven continuum manipulators. *IEEE Transactions on Robotics*, 24(6):1262–1273, 2008.

[30] M. C. Cavusoglu, F. Tendick, M. Cohn, and S. S. Sastry. A laparoscopic telesurgical workstation. *IEEE Transactions on Robotics and automation*, 15(4):728–739, 1999.

[31] S. Charles, H. Das, T. Ohm, C. Boswell, G. Rodriguez, R. Steele, and D. Istrate. Dexterity-enhanced telerobotic microsurgery. In *Advanced Robotics, 1997. ICAR'97. Proceedings., 8th International Conference on*, pages 5–10. IEEE, 1997.

[32] C. Chen. Power analysis of epicyclic transmissions based on constraints. *Journal of Mechanisms and Robotics*, 4(4):041004, 2012.

[33] C. Chen and S. Liu. Improved remote centre of motion mechanism, Oct 2016. Australian patent application number 201650360.

[34] C. Chen and M. Pamieta. Novel linkage with remote center of motion. In *3rd IFToMM International Symposium on Robotics and Mechatronics Singapore, Oct*, pages 2–4, 2013.

[35] G. S. Chirikjian and J. W. Burdick. A modal approach to hyper-redundant manipulator kinematics. *IEEE Transactions on Robotics and Automation*, 10(3):343–354, 1994.

[36] H. M. Choset. *Principles of robot motion: theory, algorithms, and implementation.* MIT press, 2005.

[37] J. Chung, H.-J. Cha, B.-J. Yi, and W. K. Kim. Implementation of a 4-dof parallel mechanism as a needle insertion device. In *Robotics and Automation (ICRA), 2010 IEEE International Conference on*, pages 662–668. IEEE, 2010.

[38] R. J. Cipra. A method for representing the configuration and analyzing the motion of complex cable-pulley systems. 2003.

[39] D. B. Comber, E. J. Barth, and R. J. Webster. Design and control of an magnetic resonance compatible precision pneumatic active cannula robot. *Journal of Medical Devices*, 8(1):011003, 2014.

[40] D. B. Comber, D. Cardona, R. Webster III, and E. J. Barth. Precision pneumatic robot for mri-guided neurosurgery. *ASME J. Med. Dev*, 6(1):017587, 2012.

[41] T. G. Cooper and T. R. Solomon. Offset remote center manipulator for robotic surgery, Sept. 29 2009. US Patent 7,594,912.

[42] M. M. Dalvand and B. Shirinzadeh. Remote centre-of-motion control algorithms of 6-rrcrr parallel robot assisted surgery system (pramiss). In *Robotics and Automation (ICRA), 2012 IEEE International Conference on*, pages 3401–3406. IEEE, 2012.

[43] B. Davies. A review of robotics in surgery. *Proceedings of the Institution of Mechanical Engineers, Part H: Journal of Engineering in Medicine*, 214(1):129–140, 2000.

[44] B. Davies, R. Hibberd, W. Ng, A. Timoney, and J. Wickham. The development of a surgeon robot for prostatectomies. *Proceedings of the Institution of Mechanical Engineers, Part H: Journal of Engineering in Medicine*, 205(1):35–38, 1991.

[45] B. Davies, S. Starkie, S. J. Harris, E. Agterhuis, V. Paul, and L. M. Auer. Neurobot: A special-purpose robot for neurosurgery. In *Robotics and Automation, 2000. Proceedings. ICRA'00. IEEE International Conference on*, volume 4, pages 4103–4108. IEEE, 2000.

[46] A. Degani, H. Choset, A. Wolf, and M. A. Zenati. Highly articulated robotic probe for minimally invasive surgery. In *Robotics and Automation, 2006. ICRA 2006. Proceedings 2006 IEEE International Conference on*, pages 4167–4172. IEEE, 2006.

[47] C. Delgorge, F. Courrèges, L. A. Bassit, C. Novales, C. Rosenberger, N. Smith-Guerin, C. Brù, R. Gilabert, M. Vannoni, G. Poisson, et al. A tele-operated mobile ultrasound scanner using a light-weight robot. *IEEE Transactions on Information Technology in Biomedicine*, 9(1):50–58, 2005.

[48] E. Della Flora, T. G. Wilson, I. J. Martin, N. A. O'rourke, and G. J. Maddern. A review of natural orifice translumenal endoscopic surgery (notes) for intra-abdominal surgery: experimental models, techniques, and applicability to the clinical setting. *Annals of surgery*, 247(4):583–602, 2008.

[49] E. Dombre, M. Michelin, F. Pierrot, P. Poignet, P. Bidaud, G. Morel, T. Ort-maier, D. Sallé, N. Zemiti, P. Gravez, et al. Marge project: design, modeling and control of assistive devices for minimally invasive surgery. In *International Conference on Medical Image Computing and Computer-Assisted Intervention*, pages 1–8. Springer, 2004.

[50] P. E. Dupont, J. Lock, and E. Butler. Torsional kinematic model for concentric tube robots. In *Robotics and Automation, 2009. ICRA'09. IEEE International Conference on*, pages 3851–3858. IEEE, 2009.

[51] P. E. Dupont, J. Lock, and B. Itkowitz. Real-time position control of concentric tube robots. In *Robotics and Automation (ICRA), 2010 IEEE International Conference on*, pages 562–568. IEEE, 2010.

[52] P. E. Dupont, J. Lock, B. Itkowitz, and E. Butler. Design and control of concentric-tube robots. *IEEE Transactions on Robotics*, 26(2):209–225, 2010.

[53] B. Eldridge, K. Gruben, D. LaRose, J. Funda, S. Gomory, J. Karidis, G. McVicker, R. Taylor, and J. Anderson. A remote center of motion robotic arm for computer assisted surgery. *Robotica*, 14(01):103–109, 1996.

[54] R. Featherstone. *Robot dynamics algorithms*. PhD thesis, University of Edinburgh Scotland, 1984.

[55] M. Feng, Y. Fu, B. Pan, and C. Liu. Development of a medical robot system for minimally invasive surgery. *The International Journal of Medical Robotics and Computer Assisted Surgery*, 8(1):85–96, 2012.

[56] K. Fuchs. Minimally invasive surgery. *Endoscopy*, 34(02):154–159, 2002.

[57] J. Furusho. Curved multi-tube systems for fetal blood sampling and treatments of organs like brain and breast. *International Journal of Computer Assisted Radiology and Surgery*, 1(1):223–226, 2006.

[58] A. Ghasemi, M. Eghtesad, and M. Farid. Workspace analysis for planar and spatial

redundant cable robots. *Journal of Mechanisms and Robotics*, 1(4):044502, 2009.

[59] M. Ghodoussi, S. E. Butner, and Y. Wang. Robotic surgery-the transatlantic case. In *Robotics and Automation, 2002. Proceedings. ICRA'02. IEEE International Conference on*, volume 2, pages 1882–1888. IEEE, 2002.

[60] H. B. Gilbert, R. J. Hendrick, and R. J. Webster III. Elastic stability of concentric tube robots: a stability measure and design test. *IEEE Transactions on Robotics*, 32(1):20–35, 2016.

[61] H. B. Gilbert, J. Neimat, and R. J. Webster. Concentric tube robots as steerable needles: Achieving follow-the-leader deployment. *IEEE Transactions on Robotics*, 31(2):246–258, 2015.

[62] H. B. Gilbert, D. C. Rucker, and R. J. Webster III. Concentric tube robots: The state of the art and future directions. In *Robotics Research*, pages 253–269. Springer, 2016.

[63] H. B. Gilbert and R. J. Webster. Can concentric tube robots follow the leader? In *Robotics and Automation (ICRA), 2013 IEEE International Conference on*, pages 4881–4887. IEEE, 2013.

[64] I. S. Godage, A. A. Remirez, R. Wirz, K. D. Weaver, J. Burgner-Kahrs, and R. J. Webster. Robotic intracerebral hemorrhage evacuation: An in-scanner approach with concentric tube robots. In *Intelligent Robots and Systems (IROS), 2015 IEEE/RSJ International Conference on*, pages 1447–1452. IEEE, 2015.

[65] A. H. Gosline, N. V. Vasilyev, E. J. Butler, C. Folk, A. Cohen, R. Chen, N. Lang, P. J. Del Nido, and P. E. Dupont. Percutaneous intracardiac beating-heart surgery using metal mems tissue approximation tools. *The International journal of robotics research*, 31(9):1081–1093, 2012.

[66] A. H. Gosline, N. V. Vasilyev, A. Veeramani, M. Wu, G. Schmitz, R. Chen, V. Arabagi, J. Pedro, and P. E. Dupont. Metal mems tools for beating-heart

tissue removal. In *Robotics and Automation (ICRA), 2012 IEEE International Conference on*, pages 1921–1926. IEEE, 2012.

[67] M. Gouttefarde and C. M. Gosselin. Analysis of the wrench-closure workspace of planar parallel cable-driven mechanisms. *IEEE Transactions on Robotics*, 22(3):434–445, 2006.

[68] G. S. Guthart and J. K. Salisbury. The intuitive/sup tm/telesurgery system: overview and application. In *Robotics and Automation, 2000. Proceedings. ICRA'00. IEEE International Conference on*, volume 1, pages 618–621. IEEE, 2000.

[69] J. Ha, F. C. Park, and P. E. Dupont. Elastic stability of concentric tube robots subject to external loads. *IEEE Transactions on Biomedical Engineering*, 63(6):1116–1128, 2016.

[70] J. Ha, F. C. Park, and P. E. Dupont. Optimizing tube precurvature to enhance the elastic stability of concentric tube robots. *IEEE Transactions on Robotics*, 2016.

[71] G.-P. Haber, M. A. White, R. Autorino, P. F. Escobar, M. D. Kroh, S. Chalikonda, R. Khanna, S. Forest, B. Yang, F. Altunrende, et al. Novel robotic da vinci instruments for laparoendoscopic single-site surgery. *Urology*, 76(6):1279–1282, 2010.

[72] M. Hadavand, A. Mirbagheri, S. Behzadipour, and F. Farahmand. A novel remote center of motion mechanism for the force-reflective master robot of haptic telesurgery systems. *The International Journal of Medical Robotics and Computer Assisted Surgery*, 10(2):129–139, 2014.

[73] M. W. Hannan and I. D. Walker. Kinematics and the implementation of an elephant's trunk manipulator and other continuum style robots. *Journal of Field Robotics*, 20(2):45–63, 2003.

[74] M. Hassan and A. Khajepour. Optimization of actuator forces in cable-based parallel manipulators using convex analysis. *IEEE Transactions on Robotics*, 24(3):736–740, 2008.

[75] M. Hassan and A. Khajepour. Analysis of bounded cable tensions in cable-actuated parallel manipulators. *IEEE Transactions on Robotics*, 27(5):891–900, 2011.

[76] N. Hata, J. Tokuda, S. Hurwitz, and S. Morikawa. Mri-compatible manipulator with remote-center-of-motion control. *Journal of Magnetic Resonance Imaging*, 27(5):1130–1138, 2008.

[77] E. Hempel, H. Fischer, L. Gumb, T. Höhn, H. Krause, U. Voges, H. Breitwieser, B. Gutmann, J. Durke, M. Bock, et al. An mri-compatible surgical robot for precise radiological interventions. *Computer Aided Surgery*, 8(4):180–191, 2003.

[78] R. J. Hendrick, H. B. Gilbert, and R. J. Webster. Designing snap-free concentric tube robots: A local bifurcation approach. In *Robotics and Automation (ICRA), 2015 IEEE International Conference on*, pages 2256–2263. IEEE, 2015.

[79] R. J. Hendrick, S. D. Herrell, and R. J. Webster. A multi-arm hand-held robotic system for transurethral laser prostate surgery. In *Robotics and Automation (ICRA), 2014 IEEE International Conference on*, pages 2850–2855. IEEE, 2014.

[80] R. J. Hendrick, C. R. Mitchell, S. D. Herrell, and R. J. Webster. Hand-held transendoscopic robotic manipulators: A transurethral laser prostate surgery case study. *The International journal of robotics research*, page 0278364915585397, 2015.

[81] J. Hong, T. Dohi, M. Hashizume, K. Konishi, and N. Hata. An ultrasound-driven needle-insertion robot for percutaneous cholecystostomy. *Physics in Medicine and Biology*, 49(3):441, 2004.

[82] L. Huang, C. He, Y. Yang, and C. Guang. Equilibrium conformation of concentric-tube robots under loads based on the minimum energy principle. In *Mechanism and Machine Science: Proceedings of ASIAN MMS 2016 & CCMMS 2016*, pages 209–221. Springer, 2017.

[83] I. W. Hunter, L. Jones, M. Sagar, S. Lafontaine, and P. Hunter. Ophthalmic microsurgical robot and associated virtual environment. *Computers in biology and*

medicine, 25(2):173–182, 1995.

[84] K. Ikuta, K. Yamamoto, and K. Sasaki. Development of remote microsurgery robot and new surgical procedure for deep and narrow space. In *Robotics and Automation, 2003. Proceedings. ICRA'03. IEEE International Conference on*, volume 1, pages 1103–1108. IEEE, 2003.

[85] Intuitive Surgical. The da Vinci Surgical System. `https://www.intuitivesurgical.com/products/davinci_surgical_system/`, 2017. [Online; accessed 26/01/2017].

[86] S. C. Jacobsen, H. Ko, E. K. Iversen, and C. C. Davis. Antagonistic control of a tendon driven manipulator. In *Robotics and Automation, 1989. Proceedings., 1989 IEEE International Conference on*, pages 1334–1339. IEEE, 1989.

[87] S. C. Jacobsen, H. Ko, E. K. Iversen, and C. C. Davis. Control strategies for tendon-driven manipulators. *IEEE Control Systems Magazine*, 10(2):23–28, 1990.

[88] H. Kang and J. T. Wen. Robotic assistants aid surgeons during minimally invasive procedures. *IEEE Engineering in Medicine and Biology Magazine*, 20(1):94–104, 2001.

[89] D. Kim, E. Kobayashi, T. Dohi, and I. Sakuma. A new, compact mr-compatible surgical manipulator for minimally invasive liver surgery. In *International Conference on Medical Image Computing and Computer-Assisted Intervention*, pages 99–106. Springer, 2002.

[90] K.-Y. Kim, H.-S. Song, S.-H. Park, J.-J. Lee, and Y.-S. Yoon. Design and evaluation of a teleoperated surgical manipulator with an additional degree of freedom for laparoscopic surgery. *Advanced Robotics*, 24(12):1695–1718, 2010.

[91] K.-Y. Kim, H.-S. Song, J.-W. Suh, and J.-J. Lee. A novel surgical manipulator with workspace-conversion ability for telesurgery. *IEEE/ASME Transactions on Mechatronics*, 18(1):200–211, 2013.

[92] E. Kobayashi, K. Masamune, I. Sakuma, T. Dohi, and D. Hashimoto. A new safe laparoscopic manipulator system with a five-bar linkage mechanism and an optical zoom. *computer aided surgery*, 4(4):182–192, 1999.

[93] Y. Kobayashi, S. Chiyoda, K. Watabe, M. Okada, and Y. Nakamura. Small occupancy robotic mechanisms for endoscopic surgery. In *International Conference on Medical Image Computing and Computer-Assisted Intervention*, pages 75–82. Springer, 2002.

[94] A. Krupa, G. Morel, and M. De Mathelin. Achieving high-precision laparoscopic manipulation through adaptive force control. *Advanced Robotics*, 18(9):905–926, 2004.

[95] A. Kuntz, L. G. Torres, R. H. Feins, R. J. Webster, and R. Alterovitz. Motion planning for a three-stage multilumen transoral lung access system. In *Intelligent Robots and Systems (IROS), 2015 IEEE/RSJ International Conference on*, pages 3255–3261. IEEE, 2015.

[96] C.-H. Kuo and J. S. Dai. Robotics for minimally invasive surgery: a historical review from the perspective of kinematics. In *International symposium on history of machines and mechanisms*, pages 337–354. Springer, 2009.

[97] C.-H. Kuo, J. S. Dai, and P. Dasgupta. Kinematic design considerations for minimally invasive surgical robots: an overview. *The International Journal of Medical Robotics and Computer Assisted Surgery*, 8(2):127–145, 2012.

[98] C.-H. Kuo and S.-J. Lai. Design of a novel statically balanced mechanism for laparoscope holders with decoupled positioning and orientating manipulation. *Journal of Mechanisms and Robotics*, 8(1):015001, 2016.

[99] S. E. Landsberger and T. Sheridan. A minimal, minimal linkage: The tension compression parallel link manipulator. In *Proceedings of IMACS/SICE international symposium on robotics, mechatronics and manufacturing systems*, pages 81–88, 1993.

[100] A. R. Lanfranco, A. E. Castellanos, J. P. Desai, and W. C. Meyers. Robotic surgery: a current perspective. *Annals of surgery*, 239(1):14–21, 2004.

[101] D. Lau, D. Oetomo, and S. K. Halgamuge. Generalized modeling of multilink cable-driven manipulators with arbitrary routing using the cable-routing matrix. *IEEE Transactions on Robotics*, 29(5):1102–1113, 2013.

[102] D.-Y. Lee, J. Kim, J.-S. Kim, C. Baek, G. Noh, D.-N. Kim, K. Kim, S. Kang, and K.-J. Cho. Anisotropic patterning to reduce instability of concentric-tube robots. *IEEE Transactions on Robotics*, 31(6):1311–1323, 2015.

[103] A. Lehman, M. Tiwari, B. Shah, S. Farritor, C. Nelson, and D. Oleynikov. Recent advances in the cobrasurge robotic manipulator and dexterous miniature in vivo robotics for minimally invasive surgery. *Proceedings of the Institution of Mechanical Engineers, Part C: Journal of Mechanical Engineering Science*, 224(7):1487–1494, 2010.

[104] J. Li, S. Wang, X. Wang, and C. He. Optimization of a novel mechanism for a minimally invasive surgery robot. *The international journal of medical robotics and computer assisted surgery*, 6(1):83–90, 2010.

[105] J. Li, S. Wang, X. Wang, C. He, et al. Development of a novel mechanism for minimally invasive surgery. In *Robotics and Biomimetics (ROBIO), 2010 IEEE International Conference on*, pages 1370–1375. IEEE, 2010.

[106] J. Li, Y. Xing, K. Liang, and S. Wang. Kinematic design of a novel spatial remote center-of-motion mechanism for minimally invasive surgical robot. *Journal of Medical Devices*, 9(1):011003, 2015.

[107] J. Li, G. Zhang, A. Müller, and S. Wang. A family of remote center of motion mechanisms based on intersecting motion planes. *Journal of Mechanical Design*, 135(9):091009, 2013.

[108] J. Li, G. Zhang, Y. Xing, H. Liu, and S. Wang. A class of 2-degree-of-freedom planar

remote center-of-motion mechanisms based on virtual parallelograms. *Journal of Mechanisms and Robotics*, 6(3):031014, 2014.

[109] Z. Li, P. W. Chiu, and R. Du. Design and kinematic modeling of a concentric wire-driven mechanism targeted for minimally invasive surgery. In *Intelligent Robots and Systems (IROS), 2016 IEEE/RSJ International Conference on*, pages 310–316. IEEE, 2016.

[110] Z. Li, L. Wu, H. Ren, and H. Yu. Kinematic comparison of surgical tendon-driven manipulators and concentric tube manipulators. *Mechanism and Machine Theory*, 107:148–165, 2017.

[111] S. Liu, B. Chen, S. Caro, S. Briot, and C. Chen. Dual-triangular remote centre of motion mechanism with cable transmission. In *4th Joint International Conference on Multibody System Dynamics (IMSD2016)*, 2016.

[112] S. Liu, B. Chen, S. Caro, S. Briot, L. Harewood, and C. Chen. A cable linkage with remote centre of motion. *Mechanism and Machine Theory*, 105:583–605, 2016.

[113] S. Liu, C. Chen, B. Chen, and L. Harewood. Novel linkage with remote centre of motion. In *Proceedings of the 14th IFToMM World Congress*, pages 338–343. , 2015.

[114] S. Liu, L. Harewood, B. Chen, and C. Chen. A review on direct kinematics models and iteration shcemes of continuum concentric tube robots. In *Proc. 2015 Australian Biomedical Engineering Conference (ABEC)*, 2015.

[115] S. T. Liu and C. Chen. Framework of modelling concentric tube robot and comparison on computational efficiency. *Meccanica*, pages 1–17.

[116] S. T. Liu, L. Harewood, B. Chen, and C. Chen. A skeletal prototype of surgical arm based on dual-triangular mechanism. *Journal of Mechanisms and Robotics*, 8(4):041015, 2016.

[117] J. Lock and P. E. Dupont. Friction modeling in concentric tube robots. In *Robotics*

and Automation (ICRA), 2011 IEEE International Conference on, pages 1139–1146. IEEE, 2011.

[118] J. Lock, G. Laing, M. Mahvash, and P. E. Dupont. Quasistatic modeling of concentric tube robots with external loads. In Intelligent Robots and Systems (IROS), 2010 IEEE/RSJ International Conference on, pages 2325–2332. IEEE, 2010.

[119] R. C. Locke and R. V. Patel. Optimal remote center-of-motion location for robotics-assisted minimally-invasive surgery. In Robotics and Automation, 2007 IEEE International Conference on, pages 1900–1905. IEEE, 2007.

[120] H. Long, Y. Yang, X. Jingjing, and S. Peng. Type synthesis of 1r1t remote center of motion mechanisms based on pantograph mechanisms. Journal of Mechanical Design, 138(1):014501, 2016.

[121] M. H. Loser and N. Navab. A new robotic system for visually controlled percutaneous interventions under ct fluoroscopy. In International Conference on Medical Image Computing and Computer-Assisted Intervention, pages 887–896. Springer, 2000.

[122] M. J. Lum, D. C. Friedman, G. Sankaranarayanan, H. King, K. Fodero, R. Leuschke, B. Hannaford, J. Rosen, and M. N. Sinanan. The raven: Design and validation of a telesurgery system. The International Journal of Robotics Research, 28(9):1183–1197, 2009.

[123] M. J. Lum, J. Rosen, M. N. Sinanan, and B. Hannaford. Optimization of a spherical mechanism for a minimally invasive surgical robot: theoretical and experimental approaches. IEEE Transactions on Biomedical Engineering, 53(7):1440–1445, 2006.

[124] L. A. Lyons, R. J. Webster, and R. Alterovitz. Motion planning for active cannulas. In Intelligent Robots and Systems, 2009. IROS 2009. IEEE/RSJ International Conference on, pages 801–806. IEEE, 2009.

[125] L. A. Lyons, R. J. Webster, and R. Alterovitz. Planning active cannula configura-

tions through tubular anatomy. In *Robotics and Automation (ICRA), 2010 IEEE International Conference on*, pages 2082–2087. IEEE, 2010.

[126] A. J. Madhani, G. Niemeyer, and J. K. Salisbury. The black falcon: a teleoperated surgical instrument for minimally invasive surgery. In *Intelligent Robots and Systems, 1998. Proceedings., 1998 IEEE/RSJ International Conference on*, volume 2, pages 936–944. IEEE, 1998.

[127] M. Mahvash and P. E. Dupont. Stiffness control of a continuum manipulator in contact with a soft environment. In *Intelligent Robots and Systems (IROS), 2010 IEEE/RSJ International Conference on*, pages 863–870. IEEE, 2010.

[128] M. Mahvash and P. E. Dupont. Stiffness control of surgical continuum manipulators. *IEEE Transactions on Robotics*, 27(2):334–345, 2011.

[129] K. Masamune, E. Kobayashi, Y. Masutani, M. Suzuki, T. Dohi, H. Iseki, and K. Takakura. Development of an mri-compatible needle insertion manipulator for stereotactic neurosurgery. *Journal of Image Guided Surgery*, 1(4):242–248, 1995.

[130] M. Michelin, E. Dombre, P. Poignet, F. Pierrot, and L. Eckert. Path planning under a penetration point constraint for minimally invasive surgery. In *Intelligent Robots and Systems, 2002. IEEE/RSJ International Conference on*, volume 2, pages 1475–1480. IEEE, 2002.

[131] M. Michelin, P. Poignet, and E. Dombre. Dynamic task/posture decoupling for minimally invasive surgery motions: simulation results. In *Intelligent Robots and Systems, 2004.(IROS 2004). Proceedings. 2004 IEEE/RSJ International Conference on*, volume 4, pages 3625–3630. IEEE, 2004.

[132] B. Mitchell, J. Koo, I. Iordachita, P. Kazanzides, A. Kapoor, J. Handa, G. Hager, and R. Taylor. Development and application of a new steady-hand manipulator for retinal surgery. In *Robotics and Automation, 2007 IEEE International Conference on*, pages 623–629. IEEE, 2007.

[133] S. Morikawa, S. Naka, K. Murakami, Y. Kurumi, H. Shiomi, T. Tani, H. A. Haque, J. Tokuda, N. Hata, and T. Inubushi. Preliminary clinical experiences of a motorized manipulator for magnetic resonance image–guided microwave coagulation therapy of liver tumors. *The American Journal of Surgery*, 198(3):340–347, 2009.

[134] T. A. Morley and D. T. Wallace. Roll-pitch-roll surgical tool, June 8 2004. US Patent 6,746,443.

[135] M. Muller. A novel classification of planar four-bar linkages and its application to the mechanical analysis of animal systems. *Philosophical Transactions of the Royal Society of London B: Biological Sciences*, 351(1340):689–720, 1996.

[136] R. M. Murray, Z. Li, S. S. Sastry, and S. S. Sastry. *A mathematical introduction to robotic manipulation*. CRC press, 1994.

[137] S. K. Mustafa and S. K. Agrawal. On the force-closure analysis of n-dof cable-driven open chains based on reciprocal screw theory. *IEEE Transactions on Robotics*, 28(1):22–31, 2012.

[138] R. Nakadate, Y. Tokunaga, J. Solis, A. Takanishi, E. Minagawa, M. Sugawara, K. Niki, and A. Saito. Development of robot assisted measurement system for abdominal ultrasound diagnosis. In *Biomedical Robotics and Biomechatronics (BioRob), 2010 3rd IEEE RAS and EMBS International Conference on*, pages 367–372. IEEE, 2010.

[139] G. Navarra, E. Pozza, S. Occhionorelli, P. Carcoforo, and I. Donini. One-wound laparoscopic cholecystectomy. *British Journal of Surgery*, 84(5), 1997.

[140] M. Neumann and J. Burgner-Kahrs. Considerations for follow-the-leader motion of extensible tendon-driven continuum robots. In *Robotics and Automation (ICRA), 2016 IEEE International Conference on*, pages 917–923. IEEE, 2016.

[141] T.-D. Nguyen and J. Burgner-Kahrs. A tendon-driven continuum robot with extensible sections. In *Intelligent Robots and Systems (IROS), 2015 IEEE/RSJ In-*

ternational Conference on, pages 2130–2135. IEEE, 2015.

[142] T. Ortmaier and G. Hirzinger. Cartesian control issues for minimally invasive robot surgery. In *Intelligent Robots and Systems, 2000.(IROS 2000). Proceedings. 2000 IEEE/RSJ International Conference on*, volume 1, pages 565–571. IEEE, 2000.

[143] Y.-J. Ou and L.-W. Tsai. Isotropic design of tendon-driven manipulators. Technical report, 1995.

[144] D. K. Pai. Strands: Interactive simulation of thin solids using cosserat models. In *Computer Graphics Forum*, volume 21, pages 347–352. Wiley Online Library, 2002.

[145] C. B. Pham, S. H. Yeo, G. Yang, M. S. Kurbanhusen, and I.-M. Chen. Force-closure workspace analysis of cable-driven parallel mechanisms. *Mechanism and Machine Theory*, 41(1):53–69, 2006.

[146] A. Riechel, P. Bosscher, H. Lipkin, and I. Ebert-Uphoff. Concept paper: Cable-driven robots for use in hazardous environments. In *Proceedings of the 10th international topical meeting on robotics and remote systems for hazardous environments*, 2004.

[147] H. Rininsland. Artemis. a telemanipulator for cardiac surgery. *European Journal of Cardio-Thoracic Surgery*, 16(Supplement 2):S106–S111, 1999.

[148] C. N. Riviere, R. S. Rader, and P. K. Khosla. Characteristics of hand motion of eye surgeons. In *Engineering in Medicine and Biology society, 1997. Proceedings of the 19th Annual International Conference of the IEEE*, volume 4, pages 1690–1693. IEEE, 1997.

[149] J. Rosen, J. D. Brown, L. Chang, M. Barreca, M. Sinanan, and B. Hannaford. The bluedragon-a system for measuring the kinematics and dynamics of minimally invasive surgical tools in-vivo. In *Robotics and Automation, 2002. Proceedings. ICRA'02. IEEE International Conference on*, volume 2, pages 1876–1881. IEEE, 2002.

[150] M. B. Rubin. *Cosserat theories: shells, rods and points*, volume 79. Springer Science & Business Media, 2013.

[151] D. C. Rucker, B. A. Jones, and R. J. Webster. A model for concentric tube continuum robots under applied wrenches. In *Robotics and Automation (ICRA), 2010 IEEE International Conference on*, pages 1047–1052. IEEE, 2010.

[152] D. C. Rucker, B. A. Jones, and R. J. Webster III. A geometrically exact model for externally loaded concentric-tube continuum robots. *IEEE Transactions on Robotics*, 26(5):769–780, 2010.

[153] D. C. Rucker and R. J. Webster. Mechanics-based modeling of bending and torsion in active cannulas. In *Biomedical Robotics and Biomechatronics, 2008. BioRob 2008. 2nd IEEE RAS & EMBS International Conference on*, pages 704–709. IEEE, 2008.

[154] D. C. Rucker and R. J. Webster. Computing jacobians and compliance matrices for externally loaded continuum robots. In *Robotics and Automation (ICRA), 2011 IEEE International Conference on*, pages 945–950. IEEE, 2011.

[155] D. C. Rucker and R. J. Webster III. Parsimonious evaluation of concentric-tube continuum robot equilibrium conformation. *IEEE Transactions on Biomedical Engineering*, 56(9):2308–2311, 2009.

[156] D. C. Rucker, R. J. Webster III, G. S. Chirikjian, and N. J. Cowan. Equilibrium conformations of concentric-tube continuum robots. *The International journal of robotics research*, 29(10):1263–1280, 2010.

[157] J. M. Sabater, N. Garcia, C. Perez, L. M. Lopez, F. J. Badesa, and J. Mayol. A new spherical wrist for minimally invasive robotic surgery. In *Robotics (ISR), 2010 41st International Symposium on and 2010 6th German Conference on Robotics (ROBOTIK)*, pages 1–6. VDE, 2010.

[158] T. Salcudean, W. Zhu, P. Abolmaesumi, S. Bachmann, and P. Lawrence. A robot

system for medical ultrasound. In *ROBOTICS RESEARCH-INTERNATIONAL SYMPOSIUM-*, volume 9, pages 195–202. Citeseer, 2000.

[159] D. Sanchez, M. Black, and S. Hammond. Pivot point arm for a robotic system used to perform a surgical procedure, May 1 2001. US Patent App. 09/847,736.

[160] R. Satava, J. Bowersox, M. Mack, and T. Krummel. Robotic surgery: state of the art and future trends. *Contemp Surg*, 57(10):489–99, 2001.

[161] B. M. Schena. Center robotic arm with five-bar spherical linkage for endoscopic camera, May 1 2012. US Patent 8,167,872.

[162] B. M. Schena, R. L. Devengenzo, G. C. Ettinger, E. F. Duval, N. Diolaiti, and D. H. Gomez. Redundant axis and degree of freedom for hardware-constrained remote center robotic manipulator, Mar. 29 2016. US Patent 9,295,524.

[163] M. Schurr, A. Arezzo, B. Neisius, H. Rininsland, H.-U. Hilzinger, J. Dorn, K. Roth, and G. Buess. Trocar and instrument positioning system tiska. *Surgical endoscopy*, 13(5):528–531, 1999.

[164] M. Schurr, G. Buess, B. Neisius, and U. Voges. Robotics and telemanipulation technologies for endoscopic surgery. *Surgical endoscopy*, 14(4):375–381, 2000.

[165] P. Sears and P. Dupont. A steerable needle technology using curved concentric tubes. In *Intelligent Robots and Systems, 2006 IEEE/RSJ International Conference on*, pages 2850–2856. IEEE, 2006.

[166] W.-J. Shiang, D. Cannon, and J. Gorman. Dynamic analysis of the cable array robotic crane. In *Robotics and Automation, 1999. Proceedings. 1999 IEEE International Conference on*, volume 4, pages 2495–2500. IEEE, 1999.

[167] S.-E. Song, J. Tokuda, K. Tuncali, A. Yamada, M. Torabi, and N. Hata. Design evaluation of a double ring rcm mechanism for robotic needle guidance in mri-guided liver interventions. In *Intelligent Robots and Systems (IROS), 2013 IEEE/RSJ International Conference on*, pages 4078–4083. IEEE, 2013.

[168] D. Stoianovici. Uroboticsurology robotics at johns hopkins. *Computer Aided Surgery*, 6(6):360–369, 2001.

[169] D. Stoianovici, K. Cleary, A. Patriciu, D. Mazilu, A. Stanimir, N. Craciunoiu, V. Watson, and L. Kavoussi. Acubot: a robot for radiological interventions. *IEEE Transactions on Robotics and Automation*, 19(5):927–930, 2003.

[170] D. Stoianovici, C. Kim, F. Schäfer, C.-M. Huang, Y. Zuo, D. Petrisor, and M. Han. Endocavity ultrasound probe manipulators. *IEEE/ASME Transactions on Mechatronics*, 18(3):914–921, 2013.

[171] D. Stoianovici, L. L. Whitcomb, J. H. Anderson, R. H. Taylor, and L. R. Kavoussi. A modular surgical robotic system for image guided percutaneous procedures. In *International Conference on Medical Image Computing and Computer-Assisted Intervention*, pages 404–410. Springer, 1998.

[172] D. Stoianovici, L. L. Whitcomb, D. Mazilu, R. H. Taylor, and L. R. Kavoussi. Remote center of motion robotic system and method, Apr. 4 2006. US Patent 7,021,173.

[173] H. Su, D. C. Cardona, W. Shang, A. Camilo, G. A. Cole, D. C. Rucker, R. J. Webster, and G. S. Fischer. A mri-guided concentric tube continuum robot with piezoelectric actuation: a feasibility study. In *Robotics and Automation (ICRA), 2012 IEEE International Conference on*, pages 1939–1945. IEEE, 2012.

[174] P. J. Swaney, J. M. Croom, J. Burgner, H. B. Gilbert, D. C. Rucker, R. J. Webster, K. D. Weaver, and P. T. Russell. Design of a quadramanual robot for single-nostril skull base surgery. In *ASME 2012 5th Annual Dynamic Systems and Control Conference joint with the JSME 2012 11th Motion and Vibration Conference*, pages 387–393. American Society of Mechanical Engineers, 2012.

[175] P. J. Swaney, A. W. Mahoney, A. A. Remirez, E. Lamers, B. I. Hartley, R. H. Feins, R. Alterovitz, and R. J. Webster. Tendons, concentric tubes, and a bevel tip: Three steerable robots in one transoral lung access system. In *Robotics and Automation*

(ICRA), 2015 IEEE International Conference on, pages 5378–5383. IEEE, 2015.

[176] X. Tang. An overview of the development for cable-driven parallel manipulator. *Advances in Mechanical Engineering*, 2014.

[177] R. Taylor, P. Jensen, L. Whitcomb, A. Barnes, R. Kumar, D. Stoianovici, P. Gupta, Z. Wang, E. Dejuan, and L. Kavoussi. A steady-hand robotic system for microsurgical augmentation. *The International Journal of Robotics Research*, 18(12):1201–1210, 1999.

[178] R. H. Taylor, J. Funda, B. Eldridge, S. Gomory, K. Gruben, D. LaRose, M. Talamini, L. Kavoussi, and J. Anderson. A telerobotic assistant for laparoscopic surgery. *IEEE Engineering in Medicine and Biology Magazine*, 14(3):279–288, 1995.

[179] R. H. Taylor, J. Funda, D. D. Grossman, J. P. Karidis, and D. A. LaRose. Remote center-of-motion robot for surgery, Mar. 14 1995. US Patent 5,397,323.

[180] R. H. Taylor, A. Menciassi, G. Fichtinger, and P. Dario. Medical robotics and computer-integrated surgery. In *Springer handbook of robotics*, pages 1199–1222. Springer, 2008.

[181] A. Thakre, Y. Bailly, L. Sun, F. Van Meer, and C. Yeung. Is smaller workspace a limitation for robot performance in laparoscopy? *The Journal of urology*, 179(3):1138–1143, 2008.

[182] L. G. Torres and R. Alterovitz. Motion planning for concentric tube robots using mechanics-based models. In *Intelligent Robots and Systems (IROS), 2011 IEEE/RSJ International Conference on*, pages 5153–5159. IEEE, 2011.

[183] L. G. Torres, R. J. Webster, and R. Alterovitz. Task-oriented design of concentric tube robots using mechanics-based models. In *Intelligent Robots and Systems (IROS), 2012 IEEE/RSJ International Conference on*, pages 4449–4455. IEEE, 2012.

[184] L.-W. Tsai. Design of tendon-driven manipulators. *TRANSACTIONS-*

AMERICAN SOCIETY OF MECHANICAL ENGINEERS JOURNAL OF ME-CHANICAL DESIGN, 117:80–80, 1995.

[185] A. Üneri, M. A. Balicki, J. Handa, P. Gehlbach, R. H. Taylor, and I. Iordachita. New steady-hand eye robot with micro-force sensing for vitreoretinal surgery. In *Biomedical Robotics and Biomechatronics (BioRob), 2010 3rd IEEE RAS and EMBS International Conference on*, pages 814–819. IEEE, 2010.

[186] M. Uyguroğlu and H. Demirel. Kinematic analysis of tendon-driven robotic mechanisms using oriented graphs. *Acta mechanica*, 182(3):265–277, 2006.

[187] N. V. Vasilyev, P. E. Dupont, and P. J. Del Nido. Robotics and imaging in congenital heart surgery. *Future cardiology*, 8(2):285–296, 2012.

[188] N. V. Vasilyev, A. H. Gosline, E. Butler, N. Lang, P. J. Codd, H. Yamauchi, E. N. Feins, C. R. Folk, A. L. Cohen, R. Chen, et al. Percutaneous steerable robotic tool delivery platform and metal microelectromechanical systems device for tissue manipulation and approximation. *Circulation: Cardiovascular Interventions*, 6(4):468–475, 2013.

[189] N. V. Vasilyev, A. H. Gosline, A. Veeramani, M. T. Wu, G. P. Schmitz, R. T. Chen, V. Arabagi, P. J. Del Nido, and P. E. Dupont. Tissue removal inside the beating heart using a robotically delivered metal mems tool. *The International Journal of Robotics Research*, 34(2):236–247, 2015.

[190] A. Vilchis, J. Troccaz, P. Cinquin, K. Masuda, and F. Pellissier. A new robot architecture for tele-echography. *IEEE Transactions on Robotics and Automation*, 19(5):922–926, 2003.

[191] S. Wang, J. Ding, J. Yun, Q. Li, and B. Han. A robotic system with force feedback for micro-surgery. In *Robotics and Automation, 2005. ICRA 2005. Proceedings of the 2005 IEEE International Conference on*, pages 199–204. IEEE, 2005.

[192] S. Wang, Q. Li, J. Ding, and Z. Zhang. Kinematic design for robot-assisted laryn-

geal surgery systems. In *Intelligent Robots and Systems, 2006 IEEE/RSJ International Conference on*, pages 2864–2869. IEEE, 2006.

[193] A. C. Waspe, H. J. Cakiroglu, J. C. Lacefield, and A. Fenster. Design, calibration and evaluation of a robotic needle-positioning system for small animal imaging applications. *Physics in Medicine and Biology*, 52(7):1863, 2007.

[194] R. J. Webster, A. M. Okamura, and N. J. Cowan. Toward active cannulas: Miniature snake-like surgical robots. In *Intelligent Robots and Systems, 2006 IEEE/RSJ International Conference on*, pages 2857–2863. IEEE, 2006.

[195] R. J. Webster, J. M. Romano, and N. J. Cowan. Kinematics and calibration of active cannulas. In *Robotics and Automation, 2008. ICRA 2008. IEEE International Conference on*, pages 3888–3895. IEEE, 2008.

[196] R. J. Webster III and B. A. Jones. Design and kinematic modeling of constant curvature continuum robots: A review. *The International Journal of Robotics Research*, 29(13):1661–1683, 2010.

[197] R. J. Webster III, J. M. Romano, and N. J. Cowan. Mechanics of precurved-tube continuum robots. *IEEE Transactions on Robotics*, 25(1):67–78, 2009.

[198] W. Wei, R. E. Goldman, H. F. Fine, S. Chang, and N. Simaan. Performance evaluation for multi-arm manipulation of hollow suspended organs. *IEEE transactions on robotics*, 25(1):147–157, 2009.

[199] W. Wei and N. Simaan. Modeling, force sensing, and control of flexible cannulas for microstent delivery. *Journal of Dynamic Systems, Measurement, and Control*, 134(4):041004, 2012.

[200] K. Xu and N. Simaan. An investigation of the intrinsic force sensing capabilities of continuum robots. *IEEE Transactions on Robotics*, 24(3):576–587, 2008.

[201] R. Xu, A. Asadian, A. S. Naidu, and R. V. Patel. Position control of concentric-tube continuum robots using a modified jacobian-based approach. In *Robotics and*

Automation (ICRA), 2013 IEEE International Conference on, pages 5813–5818. IEEE, 2013.

[202] R. Xu, S. F. Atashzar, and R. V. Patel. Kinematic instability in concentric-tube robots: Modeling and analysis. In *Biomedical Robotics and Biomechatronics (2014 5th IEEE RAS & EMBS International Conference on*, pages 163–168. IEEE, 2014.

[203] R. Xu and R. Patel. A fast torsionally compliant kinematic model of concentric-tube robots. In *Engineering in Medicine and Biology Society (EMBC), 2012 annual international conference of the IEEE*, pages 904–907. IEEE, 2012.

[204] R. Yao, X. Tang, J. Wang, and P. Huang. Dimensional optimization design of the four-cable-driven parallel manipulator in fast. *IEEE/ASME Transactions On Mechatronics*, 15(6):932–941, 2010.

[205] T. Yasunaga, M. Hashizume, E. Kobayashi, K. Tanoue, T. Akahoshi, K. Konishi, S. Yamaguchi, N. Kinjo, M. Tomikawa, Y. Muragaki, et al. Remote-controlled laparoscope manipulator system, naviot, for endoscopic surgery. In *International Congress Series*, volume 1256, pages 678–683. Elsevier, 2003.

[206] X. You, Z. Xu, W. Chen, S. Yu, and Y. Jin. Dynamic modeling and tension analysis of a 7-dof cable-driven robotic arm. In *Conference Anthology, IEEE*, pages 1–6. IEEE, 2013.

[207] H. Yu, J.-H. Shen, K. M. Joos, and N. Simaan. Design, calibration and preliminary testing of a robotic telemanipulator for oct guided retinal surgery. In *Robotics and Automation (ICRA), 2013 IEEE International Conference on*, pages 225–231. IEEE, 2013.

[208] N. Zemiti, G. Morel, T. Ortmaier, and N. Bonnet. Mechatronic design of a new robot for force control in minimally invasive surgery. *IEEE/ASME Transactions On Mechatronics*, 12(2):143–153, 2007.

[209] N. Zemiti, T. Ortmaier, and G. Morel. A new robot for force control in minimally

invasive surgery. In *Intelligent Robots and Systems, 2004.(IROS 2004). Proceedings. 2004 IEEE/RSJ International Conference on*, volume 4, pages 3643–3648. IEEE, 2004.

[210] F. Zhang, X. Zhang, L. Hang, C. Lu, and T. Furukawa. Type synthesis of n-parallelogram-based surgical arm with remote actuated configuration. In *Mechanism and Machine Science: Proceedings of ASIAN MMS 2016 & CCMMS 2016*, pages 183–194. Springer, 2017.

[211] X. Zhang and C. A. Nelson. Kinematic analysis and optimization of a novel robot for surgical tool manipulation. *Journal of Medical Devices*, 2(2):021003, 2008.

[212] W.-H. Zhu, S. Salcudean, S. Bachmann, and P. Abolmaesumi. Motion/force/image control of a diagnostic ultrasound robot. In *Robotics and Automation, 2000. Proceedings. ICRA'00. IEEE International Conference on*, volume 2, pages 1580–1585. IEEE, 2000.

[213] G. Zong, X. Pei, J. Yu, and S. Bi. Classification and type synthesis of 1-dof remote center of motion mechanisms. *Mechanism and Machine Theory*, 43(12):1585–1595, 2008.